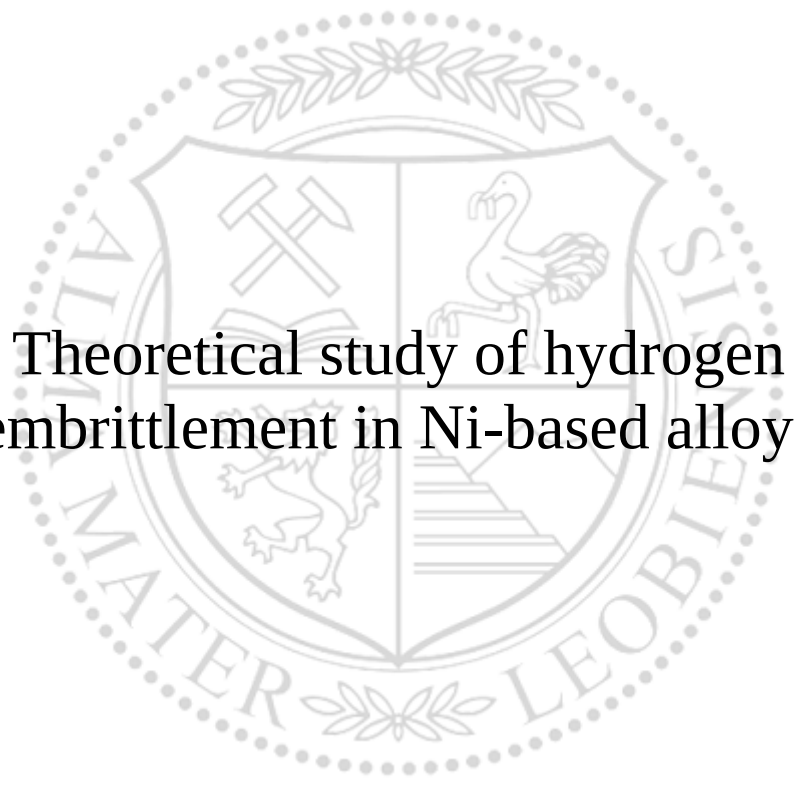




Chair of Materials Physics

Doctoral Thesis



Theoretical study of hydrogen
embrittlement in Ni-based alloys

Teol.lic. Shuang He

December 2019

AFFIDAVIT

I declare on oath that I wrote this thesis independently, did not use other than the specified sources and aids, and did not otherwise use any unauthorized aids.

I declare that I have read, understood, and complied with the guidelines of the senate of the Montanuniversität Leoben for "Good Scientific Practice".

Furthermore, I declare that the electronic and printed version of the submitted thesis are identical, both, formally and with regard to content.

Date 05.12.2019

Signature Author
Shuang, He

The author has carried out the research reported in this thesis at the Computational Materials Design Group of Materials Center Leoben Forschung GmbH, Austria. This work was financially supported under the scope of the COMET program within the K2 Center “Integrated Computational Material, Process and Product Engineering (IC-MPPE)” (Project No. 859480). This program is supported by voestalpine BÖHLER Edelstahl GmbH & Co KG, the Austrian Federal Ministries for Transport, Innovation and Technology (BMVIT) and for Digital and Economic Affairs (BMDW), represented by the Austrian research funding association (FFG), and the federal states of Styria, Upper Austria and Tyrol.

© 2019 by Shuang He. All rights reserved.
Materials Center Leoben Forschung GmbH
Roseggerstraße 12
8700 Leoben, Austria

Acknowledgements

This thesis would not have been possible without the inspiration and support of a number of wonderful individuals – my thanks and appreciation to all of them for being part of this journey and making this thesis possible. I owe my deepest gratitude to Vsevolod Razumovskiy and Werner Ecker, who introduced me to this project within the topic of hydrogen embrittlement and helped me in case I got stuck.

I would like to thank my supervisor Reinhard Pippan, who contributed extensively with discussion and supervision to my understanding of mechanical properties of metals and helped me to gain insight into the fracture mechanisms and see the problems from an experimentalist's point of view. Furthermore, I would also like to thank Reinhold Ebner, my co-supervisor, for his support and proof-reading the thesis. I want to acknowledge our group leader Lorenz Romaner who gave advises on this thesis and other co-authors, Nada Kulo, Maxim Popov, Thomas Antretter, Daniel Scheiber, Tarlan Hajilou, Iman Taji, Frédéric Christien, and Afrooz Barnoush, who were always eager to indulge in fruitful discussions.

I am forever thankful to my colleagues in the Hydrogen Resistant Materials project for their friendship and support, and for creating a cordial working environment. I thankfully acknowledge the contributions of Ernst Plesiutchnig, Christoph Turk, and Marianne Kapp from voestalpine BÖHLER Edelstahl GmbH & Co KG for the project as well as for their insight into addressing industrial concerns.

It is a pleasure to thank all of my colleagues at Computational Materials Design group of Materials Center Leoben Forschung GmbH for the wonderful times and discussion we had. In addition, I would like to thank all my friends in Leoben who gave me the necessary distractions from my research and made my stay in Austria memorable.

Finally, my deep and sincere gratitude to my parents, sister, and brother for their continuous and unparalleled love, help and support. I thank with love to my wife for always being there and supporting me.

Abstract

Ni and its alloys are susceptible to hydrogen embrittlement. In this thesis, the systematic density functional theory investigations have been performed to explore some of the fundamental aspects of how hydrogen interacts with Ni and to aid the development of Ni-based alloys with improved resistance against hydrogen induced damage intended for use in hydrogen-containing environments.

Grain boundary and lattice cohesion plays a critical role in the hydrogen-enhanced decohesion of hydrogen embrittlement mechanism. Firstly, the effects of a comprehensive set of solutes on Ni bulk lattice and GB cohesion have been investigated by means of density functional theory high-throughput calculations to identify the enhancer elements to Ni lattice and GB in our selected solutes. Furthermore, the synergistic effects of H-solute co-segregation, such as, H-Mo, H-C, and H-S, on the GB cohesion have been investigated in detail. In particular, in the case of H-S co-segregation, the simulated detrimental effect of H-S co-segregation on GB decohesion as well as the S GB segregation contents after heat treatment have been compared to the experimental observations.

It has been suggested in a number of recent theoretical investigations at 0 K that hydrogen atoms can accumulate at defects of Ni in a form of clusters. In the second part of this thesis, a combination of density functional theory calculations and embedded atom method simulations has been employed to investigate the configurations of H clusters at defects in Ni at 0 K as well as finite temperatures. Results show that the stability of H clusters in Ni is limited to temperatures below 300 K and that their appearance at the ambient temperature and therefore an impact on possible hydrogen embrittlement mechanisms is unlikely.

In the final part, the thermodynamic and mechanical stability of Ni_3X type compounds has been determined by density functional theory calculations of formation enthalpies and elastic properties of their L1_2 , D0_{22} and D0_{24} phases. In addition, the site occupancy behavior and solubility of some key elements in the L1_2 -structure Ni_3Al , Ni_3Ti , and Ni_3Nb intermetallic compounds have been investigated in detail. The most stable structure for each Ni_3X has been

identified, which can be used for the investigation of hydrogen embrittlement on Ni precipitates as well as Ni/precipitate interfaces.

This thesis revealed the hydrogen-induced embrittling at the atomic scale by taking use of the atomistic simulations, and gained insights into the hydrogen embrittlement mechanisms in Ni-based alloys. The findings provided the theoretical prediction of hydrogen effect on Ni-based alloys and offered a pathway for the design of hydrogen resistant Ni-based alloys.

Kurzfassung

Ni und Ni Legierungen sind anfällig für Wasserstoffversprödung. In dieser Doktorarbeit wurden deshalb Simulationen mithilfe der Dichtefunktionaltheorie durchgeführt um zu untersuchen wie Wasserstoff in Ni wechselwirkt und um die Entwicklung von Ni-basierten Legierungen mit erhöhter Resistenz gegen Wasserstoffversprödung voranzutreiben.

Die Kohäsion von Korngrenzen und Kristallgitter spielt eine entscheidende Rolle bei den Mechanismen verantwortlich für Wasserstoffversprödung. Deswegen wurde der Effekt auf die Korngrenzen- und Kristallgitterkohäsion einer umfassenden Auswahl von Legierungselementen mittels high-throughput DFT-Simulationen untersucht und darauf die Elemente identifiziert, die die Kohäsion erhöhen. Weiters wurden die kombinierten Effekte von H Kosegregation mit Legierungselementen wie Mo, C, und S studiert. Spezielles Augenmerk wurde auf den Fall von H-S Kosegregation und die daraus folgende Versprödung von Korngrenzen gelegt, wobei die Korngrenzengehälter und die Änderungen in der Kohäsion nach einer Temperaturbehandlung mit experimentellen Beobachtungen verglichen wurden.

Es gibt mehrere aktuelle Literaturquellen die durch Simulationen bei 0 K beobachtet haben das Wasserstoff sich an Defekten in Ni anreichert und dabei stabile Cluster bildet. Im zweiten Teil dieser Arbeit wurde eine Kombination von DFT-Simulationen und Simulationen mit der Embedded-Atom-Methode verwendet um verschiedene Konfigurationen von H-Cluster an Ni Defekten bei 0 K und auch bei endlichen Temperaturen zu untersuchen. Die Ergebnisse zeigen das die Stabilität der Cluster nur unter 300 K gegeben ist und daher ein Beitrag zur Wasserstoffversprödung von H-Cluster bei Umgebungstemperatur unwahrscheinlich ist.

Im letzten Teil wurde die thermodynamische und mechanische Stabilität von Ni_3 X-artigen Verbindungen untersucht durch Berechnung der Formierungsenthalpien und der elastischen Eigenschaften von $L1_2$, $D0_{22}$ und $D0_{24}$ Phasen. Zusätzlich wurden die Besetzung und die Löslichkeit von einigen wesentlichen Elementen in der $L1_2$ -Struktur von den intermetallischen Verbindungen Ni_3Al , Ni_3Ti , und Ni_3Nb berechnet, welche zur weiteren Untersuchung von

Wasserstoffversprödung bei Ni-Ausscheidungen sowie Grenzflächen zwischen Ni und den Ausscheidungen verwendet werden können.

Insgesamt wurde in dieser Arbeit mittels Simulationen gezeigt wie Wasserstoff auf atomarer Ebene zu Versprödung in Ni und Ni Legierungen führt. Die Ergebnisse dieser Arbeit geben den Weg vor für die Entwicklung von Ni Legierungen die resistent sind gegen Wasserstoffversprödung.

Table of contents

| | | |
|----------|---|-----------|
| I | Hydrogen embrittlement in Nickel | 1 |
| 1 | Introduction | 2 |
| 1.1 | History and overview | 2 |
| 1.1.1 | Hydrogen embrittlement | 2 |
| 1.1.2 | The properties of hydrogen molecule | 3 |
| 1.1.3 | The source of hydrogen | 3 |
| 2 | Embrittlement and strengthening in Ni-based alloys | 5 |
| 2.1 | Hydrogen embrittlement | 5 |
| 2.1.1 | Hydrogen embrittlement mechanisms | 5 |
| 2.1.2 | Hydrogen embrittlement in Ni and Ni-based alloys | 6 |
| 2.1.3 | Simulation of hydrogen embrittlement mechanisms | 6 |
| 2.2 | The strengthening mechanisms of Ni-base alloys | 7 |
| 2.2.1 | Solid solution strengthening | 7 |
| 2.2.2 | Grain boundary segregation and strengthening | 8 |
| 2.2.3 | Precipitate strengthening | 8 |
| 3 | Theoretical background | 10 |
| 3.1 | First-principles approach | 10 |
| 3.1.1 | The Hamiltonian of the system | 10 |
| 3.1.2 | Density functional theory | 11 |
| 3.1.3 | Local density and generalized gradient approximation | 12 |
| 3.1.4 | Wave function methods and projector augmented wave method | 13 |
| 3.2 | Molecular dynamic and embedded-atom method | 14 |
| 3.2.1 | Molecular dynamic | 14 |
| 3.2.2 | Embedded-atom method | 14 |

| | | |
|-----------|--|-----------|
| 4 | Overview of this thesis | 16 |
| 4.1 | Solute alloying effect on Ni | 16 |
| 4.2 | Co-segregation of H-solute to Ni grain boundary | 16 |
| 4.3 | Hydrogen clustering at defects in Ni | 17 |
| 4.4 | Thermodynamic and mechanical stability of Ni ₃ X-type precipitate | 17 |
| | References | 19 |
| II | Results and discussion | 22 |
| 5 | The effects of solute solid solution and grain boundary segregation on the strengthening in Ni | 23 |
| 5.1 | Introduction | 23 |
| 5.2 | Methodology | 24 |
| 5.2.1 | Density functional theory | 24 |
| 5.2.2 | Calculation of energetic quantities | 25 |
| 5.3 | Results and discussion | 29 |
| 5.3.1 | Solutes in bulk Ni | 29 |
| 5.3.2 | Solute segregation energy in Ni $\Sigma 5(012)$ GB | 30 |
| 5.3.3 | Alloying effect of solute on the GB cohesion of Ni | 32 |
| 5.3.4 | Solute distribution at the GB | 32 |
| 5.4 | Correlation between bulk cohesion and GB strengthening | 33 |
| 5.5 | Conclusion | 33 |
| | References | 37 |
| 6 | Hydrogen-enhanced decohesion mechanism of the special $\Sigma 5(012)$ [100] grain boundary in Ni with Mo and C solutes | 38 |
| 6.1 | Introduction | 38 |
| 6.2 | Computational details | 40 |
| 6.2.1 | Semiempirical calculations | 40 |
| 6.2.2 | DFT calculations | 40 |
| 6.3 | Methodology | 40 |
| 6.3.1 | Solution energy | 40 |
| 6.3.2 | Pair interactions in the bulk | 41 |
| 6.3.3 | Interface formation energy | 41 |
| 6.3.4 | Segregation energy | 42 |
| 6.3.5 | Co-segregation of H-solute to an interface | 43 |

| | | |
|----------|--|-----------|
| 6.3.6 | GB strengthening energy | 43 |
| 6.3.7 | Representative GB and FS construction | 44 |
| 6.4 | Results and discussion | 46 |
| 6.4.1 | Choice of the exchange-correlation functional | 46 |
| 6.4.2 | Solubility of H, C and Mo in bulk Ni | 48 |
| 6.4.3 | Solute segregation to GB and FS | 48 |
| 6.4.4 | Effects of volume and impurity excess changes | 51 |
| 6.4.5 | Interaction of H with Mo and C solutes in Ni | 54 |
| 6.5 | Conclusion | 59 |
| | References | 62 |
| 7 | Hydrogen enhanced intergranular failure of sulfur doped nickel grain boundary: In-situ electrochemical micro cantilever bending vs. DFT | 63 |
| 7.1 | Introduction | 63 |
| 7.2 | Method | 65 |
| 7.2.1 | Materials and characterization | 65 |
| 7.2.2 | Micro cantilever milling and testing | 66 |
| 7.2.3 | Computational details | 68 |
| 7.3 | Results | 70 |
| 7.3.1 | Bending of the bi-crystal micro cantilevers | 70 |
| 7.3.2 | Computational results | 73 |
| 7.4 | Discussion | 81 |
| 7.4.1 | GB effect on the micro mechanical behavior of the pure Ni bi-crystal | 81 |
| 7.4.2 | GB S segregation effect on the micro mechanical behavior of the Ni bi-crystal | 83 |
| 7.4.3 | Decohesion enhancement of the GB hosting S and H | 85 |
| 7.4.4 | H concentration enhancement | 86 |
| 7.5 | Conclusions | 90 |
| | References | 94 |
| 8 | A theoretical insight into hydrogen clustering at defects in Ni | 95 |
| 8.1 | Introduction | 95 |
| 8.2 | Computational details | 95 |
| 8.2.1 | Density functional theory calculations | 95 |
| 8.2.2 | Semiempirical calculations | 96 |
| 8.2.3 | Computational models | 96 |
| 8.3 | Results and discussions | 98 |

| | | |
|-----------|---|------------|
| 8.3.1 | Segregation of H to the defects of Ni | 98 |
| 8.3.2 | H-vacancy cluster in bulk Ni | 99 |
| 8.3.3 | H cluster at Ni grain boundary | 102 |
| 8.4 | Conclusion | 102 |
| | References | 104 |
| 9 | Thermodynamic and mechanical stability of Ni₃X-type compounds | 105 |
| 9.1 | Introduction | 105 |
| 9.2 | Methodology | 107 |
| 9.2.1 | Structure models | 107 |
| 9.2.2 | Computational details | 108 |
| 9.2.3 | Equation of state | 108 |
| 9.2.4 | Formation Enthalpy | 109 |
| 9.2.5 | Elastic properties | 109 |
| 9.2.6 | Solute sublattice preference in L1 ₂ -Ni ₃ X | 111 |
| 9.2.7 | Solution energy in in L1 ₂ -Ni ₃ X | 112 |
| 9.3 | Results and discussion | 112 |
| 9.3.1 | Reference state properties of elements | 112 |
| 9.3.2 | Thermodynamic stability of Ni ₃ X-type intermetallic compounds | 112 |
| 9.3.3 | Mechanical stability of precipitate phase | 114 |
| 9.3.4 | Solute site preference and solubility in L1 ₂ -Ni ₃ X intermetallic compounds | 116 |
| 9.4 | Conclusion | 120 |
| | References | 124 |
| 10 | Conclusions and outlook | 125 |
| 10.1 | Conclusions | 125 |
| 10.2 | Outlook | 126 |
| | Appendix A List of Papers | 128 |
| | Appendix B Contributions to Conferences | 130 |
| | Appendix C Acronyms and Abbreviations | 131 |

Part I

Hydrogen embrittlement in Nickel

Chapter 1

Introduction

1.1 History and overview

1.1.1 Hydrogen embrittlement

Hydrogen embrittlement (HE) phenomenon was found in 1874 in the experiment of the effect of acid on the fracture properties of iron and steel. The macroscale effect of hydrogen on the iron in the original paper was summarized as [1]: "*After a few minutes' immersion (half a minute will sometimes suffice) in strong hydrochloric or dilute sulfuric acid—a piece breaking after being bent once on itself, while before immersion it would bear bending on itself and back again two or three times before breaking*". It was further noted that "*evident to any one by the extraordinary decrease in toughness and breaking-strain of the iron so treated, and is all the more remarkable as it is not permanent, but only temporary in character; for with lapse of time the metal slowly regains its original toughness and strength*". Since then, it has been found that HE can also occur in many other metallic materials and its effect on the materials can be reversible once the hydrogen is released [2–4].

The detrimental effects of hydrogen in metallic materials have been investigated intensively and well known for more than a century. It has been reported that roughly a quarter of failures in the oil and gas industries are related to hydrogen-induced damages [5]. The main five types of hydrogen-induced damage to metallic materials are summarized as following [6]:

- hydrogen embrittlement,
- hydrogen-induced blistering,
- cracking from precipitation by internal hydrogen,
- high temperature hydrogen attack, and
- cracking from hydride.

A phase transformation usually occurs in each of the aforementioned hydrogen-induced damage process except for hydrogen embrittlement. The forms of hydrogen-induced damage which are related to phase transformations are relatively easy to understand in terms of the damage processes. However, knowing the damage processes related to hydrogen embrittlement is not an easy task and avoiding the hydrogen-induced damage processes can be difficult [6]. Furthermore, there are several general mechanisms that can strengthen the metallic materials and prevent the hydrogen embrittlement failures, which will be discussed in detail in the later chapters.

1.1.2 The properties of hydrogen molecule

Hydrogen is the lightest as well as the smallest element with a standard atomic weight of 1.008. The atomic radius of an isolated hydrogen atom is $a_0 = h^2 / (p^2 e^2 \cdot m) = 0.529 \text{ \AA}$ and the covalent atomic radius of a hydrogen atom in the crystal structures is between 0.30 and 0.35 \AA . Fig. 1.1 shows the potential energy for two hydrogen atoms as a function of the distance between them. There is a minimum at the separation of 0.74 \AA , meaning the bond length of H_2 is 0.74 \AA . As shown in Fig. 1.1, the minimal potential energy of H_2 molecule is roughly 4.52 eV (2.26 eV/H or 218.1 kJ·mol⁻¹H), which is the energy needed to break the bond and end up as two separate H atoms in a H_2 molecule [7].

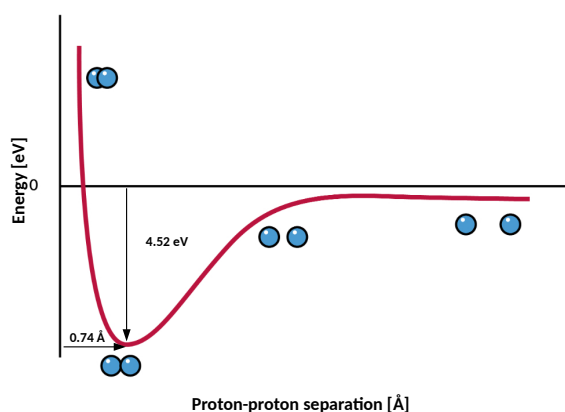


Fig. 1.1 Potential energy of hydrogen as a function of atomic separation.

1.1.3 The source of hydrogen

Generally, there are two types of hydrogen embrittlement occurring in the metallic materials at different stages: (1) internal hydrogen embrittlement, which occurs when the hydrogen

enters molten metallic materials and remains in the material after solidification; (2) external hydrogen embrittlement, which results by trapped hydrogen by solid metals from environment. The external hydrogen embrittlement requires the hydrogen source, which usually takes place during in-service condition, such as, contact with maintenance chemicals, corrosion reactions, cathodic protection, operating in high-pressure hydrogen environment and so on [8].

It is known that hydrogen molecule can be adsorbed by metallic materials and dissociated into atomic hydrogen [1]. As illustrated schematically in Fig. 1.1, the formation of atomic hydrogen on the surface of a metallic material exposed to the gaseous hydrogen or aqueous environment requires the disassociation of hydrogen molecules. Therefore, the presence of atomic hydrogen on the surface of metallic materials contributes to the hydrogen trapping and embrittlement [6].

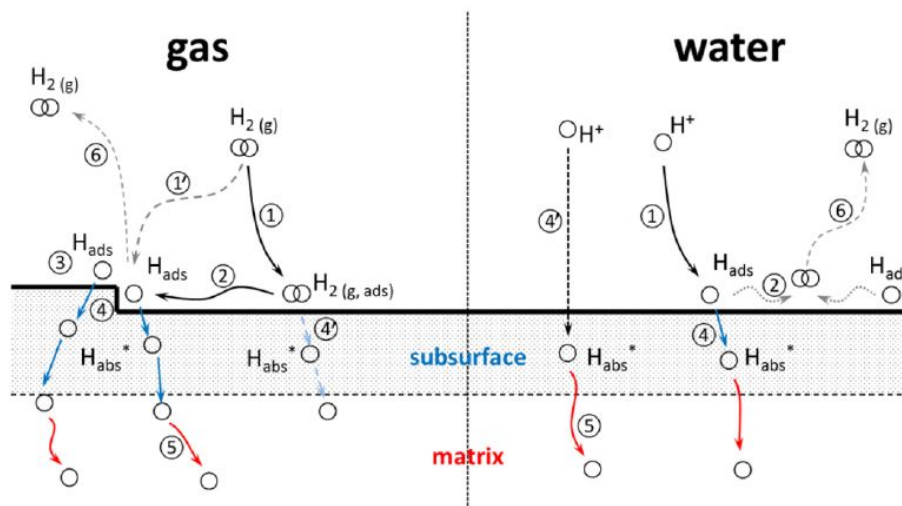


Fig. 1.2 Schematics of the different surface hydrogen reactions and possible ways of integrating atomic hydrogen into the metallic material. The gaseous and aqueous external environments are shown respectively. (1) adsorption of hydrogen from the environment [(1') direct adsorption dissociation], (2) surface migration dissociation, (3) surface dissociation, [(4) subsurface absorption] (4') direct absorption], (5) atomic hydrogen diffusion and trapping, (6) molecular recombination. The picture is taken from Ref. [8].

Fig. 1.2 shows a series of steps that how hydrogen is trapped by crystallographic features. The hydrogen source can be from gaseous and aqueous external environments, thereby molecule H_2 or atomic hydrogen atoms are adsorbed by the metal surface. During the surface reactions, the molecular hydrogen can be dissociated and the atomic hydrogen enters the base metal.

Chapter 2

Embrittlement and strengthening in Ni-based alloys

2.1 Hydrogen embrittlement

Ni and Ni-based alloys (NBA) are susceptible to hydrogen embrittlement, but the description of the underlying fundamental kinetics and mechanisms of HE is complex and multi-faceted. E.g. it requires the knowledge of the source of hydrogen, how hydrogen molecules are adsorbed by the surface of metallic materials, how hydrogen enters the materials, how hydrogen diffuses through the lattice or along interfaces (grain boundaries, phase boundaries), how hydrogen interacts with crystallographic features, modifies the properties of metals, moves with mobile dislocations, and affects the fracture modes. Some typical traps of hydrogen in materials are shown in Fig. 2.1. A number of well-established types of traps are related to a number of HE mechanisms, which can be operative at the same time [3].

2.1.1 Hydrogen embrittlement mechanisms

HE is a result of locally acting damage mechanisms and results from interplay of three factors [9]: (1) local concentration of hydrogen, (2) local mechanical loading resulting from stresses from external loading and from residual stresses, and (3) local material resistivity against HE. The mechanisms of HE on the atomic scale and hence the local material resistance is still a controversial issue. The four most prominent mechanisms explaining hydrogen induced material degradation in alloys are hydrogen enhanced localized plasticity (HELP) [10, 11], hydrogen-enhanced strain-induced vacancy formation mechanism (HESIV) [12, 13], adsorption-induced dislocation emission (AIDE) [14], and hydrogen-enhanced decohesion (HEDE) [3, 15, 16]. While HELP, HESIV and AIDE are models for

damage mechanisms related to localized plastic deformation at the crack tip, the HEDE model assumes that dissolved hydrogen reduces the cohesive strength of the lattice and interfaces. HELP, VM or AIDE mechanism are usually more pronounced at lower hydrogen levels and material strength and in case of higher strength and hydrogen levels the HEDE mechanism tends to be dominant.

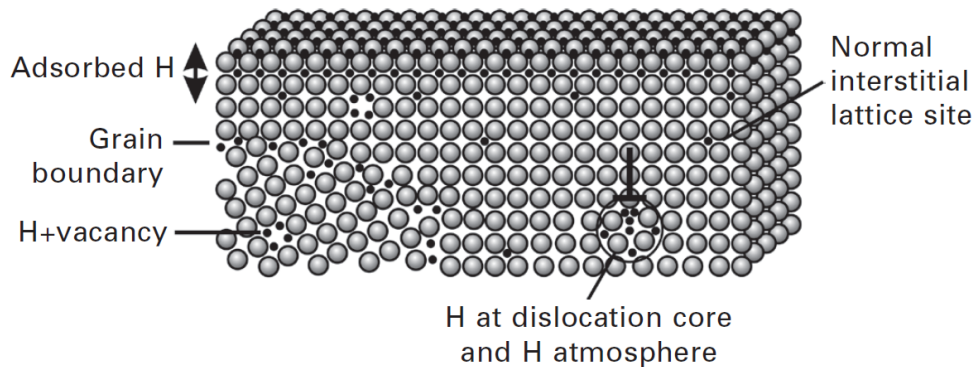


Fig. 2.1 Schematic illustration of 0-2 dimensional defects in a nanoscale film with the accumulation of hydrogen atoms. The figure is taken from Ref. [11]

2.1.2 Hydrogen embrittlement in Ni and Ni-based alloys

Ni and NBA are known to possibly show a transition in the failure mechanism from trans-to intergranular which goes along with a significant decrease in the strain to fracture [3, 16]. Hence, grain boundaries, their segregation states, the presence of precipitates and dislocation pile-ups have to be investigated in order to develop concepts for HE-resistance performance improvement in NBA. The concept of beneficial traps is a direct follow-up from the discussion of irreversible traps. The concept that very deep traps soak up hydrogen and make hydrogen atoms less mobile and hinder the HE-induced damage mechanisms is not applicable under continuous charging conditions at constant temperature, because the traps become redundant once they are filled and hydrogen ingress to potential cracking locations continues unabated [11, 17].

2.1.3 Simulation of hydrogen embrittlement mechanisms

Since the experimental studies are not able to observe the embrittlement process on an atomic scale in metallic materials, it falls to the realm of atomistic simulations to predict the interaction of hydrogen with crystallographic defects and its effect on the strength of NBA. The simulations create an additional view on how hydrogen participates in the fracture process [18–20]. For instance, DFT-based investigations can be used to predict the hydrogen distribution within

a defined matrix and at crystal defects (e.g. point defect, grain boundaries, dislocations), to investigate the effect of hydrogen onto grain boundary and interface cohesion [21–23], which is relevant for HEDE. Further, one can analyze the influence of hydrogen onto hydrogen induced dislocation formation and deformation localization (e.g. structure of dislocations, dislocation formation energies, dislocation-interface interactions, stacking fault energies), which are decisive in plasticity driven damage mechanisms such as HELP, HESIV or AIDE [3].

The early work by Foiles and coworkers [18, 24] using the embedded atom method (EAM), demonstrated that hydrogen could reduce grain boundary cohesion in Ni. However, the calculations documented in literature mainly focus on simplified model systems and neglect the effective local structure and chemical composition (e.g. segregation, precipitates) in NBA [25]. At the meantime, systematic investigation of key alloying elements and effects of co-segregation in NBA are scarce. In this project, a combined approach consisting of thermodynamic and thermokinetic phenomenological modeling (McLean segregation isotherm) and atomistic modeling (DFT and EAM calculations) have been established and applied to investigate the effect of key alloying elements on HEDE of Ni.

2.2 The strengthening mechanisms of Ni-base alloys

The metallic materials used in engineering are usually load-bearing, meaning that such materials should have the required strength not to yield or fracture under the loading condition or in service. Therefore, the mechanical properties of materials can be modified to meet a variety of different engineering applications by different strengthening mechanisms. For example, changing the nature of metallic bonding or the crystal structure to increase strength is not easy and it may lead to brittle solids, therefore strengthening efforts should be directed towards strengthening the lattice against the easy movement of lattice defects [26]. Furthermore, there are also other various strengthening mechanisms that can be effectively used to make metals and alloys meet the service requirements [27]. Some of the mechanisms investigated in this work are briefly introduced in the following sections.

2.2.1 Solid solution strengthening

Solid solution strengthening is one of efficient strengthening mechanisms to improve the strength of metallic materials by addition elements. Solid solutions are usually formed by introducing interstitial or substitutional solutes to the matrix of metallic materials, meaning that there are two types of solid solution strengthening: interstitial solid-solution strengthening and substitutional solid-solution strengthening. Note that interstitial solutions are located in

the voids formed by the host atoms of matrix, for this reason, the interstitial solutes should be small in their dimensions [27].

The usual way to form substitutional solid solutions is replacing the host atoms by solutes which have the similar radii. This enable the possibility to form a desirable alloy by substituting a large percentage of the host atoms. In this case, the Hume-Rothery rules can be used to determine the degree of solute solubility [27] in the matrix when the solute atoms differ in size from the host atoms.

2.2.2 Grain boundary segregation and strengthening

In the poly-crystalline materials, the grain boundary (GB) is the interface between two grains, which differ in mutual orientations. Usually, the GBs are preferential sites for the onset of corrosion and for the precipitation of new phases from the solid [28] and they play an important role on mechanical, functional, and kinetic properties of poly-crystalline materials. However, GBs also disrupt the motion of dislocations through a material and thereby reducing grain size can be a efficient way to improve mechanical strength, as described by the Hall-Petch relationship [29].

GB segregation is a phenomenon of the enrichment of atoms, ions, or molecules at GB region in a poly-crystalline material, the segregated elements thereby can change the energy, mobility, structure as well as cohesion of GBs. In particular, the segregation-induced change on GB cohesion in some respects is regarded as an undesired behavior but is instead used to obtain specific GB structures, compositions and properties that contributes to a better performance of the material [30, 31].

2.2.3 Precipitate strengthening

In addition to atoms in solution, second-phase particles obstruct deformation of the materials. For example, it has been known that the most important second-phase particles in precipitate-hardened Ni-base alloys are γ' and γ'' phases [32, 33]. However, strengthening of Ni-base alloys by precipitates can be related to a series of factors, where the intrinsic strength of matrix phase and ductility of the precipitates are two most important factors. But there are other important factors, such as [34]:

- coherency between the γ' or γ'' precipitates and the γ matrix
- volume fraction of γ' or γ'' in the γ matrix
- anti-phase boundary energy of the ordered γ' or γ'' phase. The dislocations in the precipitate require enough driving force to disorder the precipitate and go through it.

There are also other factors, such as, precipitate size [35] and shape [36], which can affect the strengthening of Ni-base alloys. Moreover, in Ni-base alloys containing sufficient amount of Ti and Nb, γ' and γ'' may transform to Ni_3X -type η phase which typically has mostly Ti on the X-sublattices (Ni_3X) and has an ordered hexagonal D_{024} crystal structure [37, 38].

The fundamental understanding of thermodynamic and mechanical stability of γ' , γ'' , and η is of major importance for the design of new precipitate-hardened Ni-base alloys and for an accurate thermodynamic description of the Ni-base alloys containing these phases.

Chapter 3

Theoretical background

Electrons and nuclei of the matter determine its properties. In solids, the electrons in the outmost shells of an isolated atom interact strongly with neighboring electrons, which are usually so-called valence electrons. The rest of electrons are tightly bound to the nucleus, their orbits do not extend far from the location of the nucleus, which are called core electrons. In most of cases, it is normal and reasonable to neglect the effect of core electrons and just consider the behavior of valence electrons [39].

3.1 First-principles approach

3.1.1 The Hamiltonian of the system

In classical mechanics, the motion behavior or time evolution of a particle with mass can be determined by Newton's laws. In quantum mechanics, the state or motion of the system is determined by the Schrödinger equation [40]:

$$H\Psi(\mathbf{R}_I; \mathbf{r}_i) = E\Psi(\mathbf{R}_I; \mathbf{r}_i). \quad (3.1)$$

Here, \mathbf{R}_I is the position of the ions and \mathbf{r}_i is the variable of the electrons. Hamiltonian H is the operator corresponding to the total energy of the system, which consists of the kinetic energy of the nuclei and electrons, and interactions of electron-electron, nucleus-nucleus, electron-nucleus respectively [41]:

$$H = -\sum_{I=1}^{N_c} \frac{\nabla_I^2}{2M_I} - \sum_{i=1}^{N_e} \frac{\nabla_i^2}{2m_e} + V_{ee}(\mathbf{r}_i) + V_{II}(\mathbf{R}_I) - V_{eI}(\mathbf{r}_i, \mathbf{R}_I). \quad (3.2)$$

Owing to the huge difference of mass between ions and electrons, the motion of atomic nuclei and electrons are processed separately within the framework of the Born-Oppenheimer approximation [42]. Thereby the nuclei behave like classical particles and are fixed during searching the equilibrium state for electronic subsystem, which makes it possible to solve the Schrödinger equation for the wave function of electrons independently. Therefore, the ground state properties of a non-relativistic system can be defined the Schrödinger equation with the time-independent form:

$$H\psi(\mathbf{r}_i) = \left[-\sum_{i=1}^{N_e} \frac{\nabla_i^2}{2m_e} + V_{ee}(\mathbf{r}_i) - V_{eI}(\mathbf{r}_i, \mathbf{R}_I) \right] \psi(\mathbf{r}_i) = E\psi(\mathbf{r}_i). \quad (3.3)$$

Solving the Schrödinger equation with this Hamiltonian is not an easy task for a many-electron system. For instance, if two electrons interchange their positions should also be changed; this is the so-called "exchange" property and it leads to Pauli exclusion principle.

In general, Ψ is a N -electron function, meaning that none of the electrons can be single out and all of them exist in a very complicated correlated state. In the next section, density functional theory will be introduced to provide a way for solving the many-body problem by a single-body problem with an effective potential, therefore this approach makes it possible to have a very efficient method to solve the original many-body problem (Equation 3.3).

3.1.2 Density functional theory

Density functional theory is usually implemented as an effective single particle method [43, 44], which leads to the most efficient way to describe the ground state properties of many-electron system. In particular, the total energy of the system in DFT is a unique function of the one-electron density. One can obtain the electron density by solving the one-electron Kohn-Sham equation [44]:

$$H\phi_\alpha(\mathbf{r}) = \left[-\frac{1}{2}\nabla^2 + V(\mathbf{r}) \right] \phi_\alpha(\mathbf{r}) = E_\alpha\phi_\alpha(\mathbf{r}), \quad (3.4)$$

$$n(\mathbf{r}) = \sum_{\alpha(occup)} |\phi_\alpha(\mathbf{r})|^2, \quad (3.5)$$

where H is the Kohn–Sham effective Hamiltonian, $V(\mathbf{r})$ is the effective one-electron potential and $\phi_\alpha(\mathbf{r})$ is the one-electron wave function for the energy state α .

The total energy can be written using the solution of the one-electron Kohn-Sham equations (3.5) and (3.4)

$$E_s[n] = T_s[n] + \int d\mathbf{r} V_{\text{ext}}(\mathbf{r})n(\mathbf{r}) + \frac{1}{2} \int \int d\mathbf{r} d\mathbf{r}' \frac{n(\mathbf{r})n(\mathbf{r}')}{|\mathbf{r}-\mathbf{r}'|} + \frac{1}{2} \sum_{i \neq j} \frac{Z_i Z_j}{|\mathbf{R}_i - \mathbf{R}_j|} + E_{\text{xc}}[n], \quad (3.6)$$

where $T_s[n]$ is the kinetic energy of the non-interacting electron gas

$$T_s = \sum_{a(\text{occup})} E_\alpha - \int d^3r V(\mathbf{r})n(\mathbf{r}), \quad (3.7)$$

the one-electron potential is given by

$$V(\mathbf{r}) = V_{\text{ext}}(\mathbf{r}) + \int \frac{n(\mathbf{r}')}{|\mathbf{r}-\mathbf{r}'|} d\mathbf{r}' + \frac{\delta E_{\text{xc}}[n(\mathbf{r})]}{\delta n(\mathbf{r})}. \quad (3.8)$$

The effective potential is a function of the electron density $n(\mathbf{r})$, and depends on all the single-particle states. Thus, the Kohn-Sham equations (3.4), (3.5) and (3.8) are solved using iterations until self-consistency of the one-electron potential is obtained.

3.1.3 Local density and generalized gradient approximation

To solve Kohn-Sham equations, the exchange-correlation functional, $E_{\text{xc}}[n(\mathbf{r})]$, should be known. The most common method for the exchange-correlation functional is the local density approximation (LDA)

$$E_{\text{xc}}[n(\mathbf{r})] = \int d\mathbf{r} \varepsilon_{\text{xc}}[n(\mathbf{r})]n(\mathbf{r}), \quad (3.9)$$

where $\varepsilon_{\text{xc}}[n(\mathbf{r})]$ is the exchange-correlation energy of each particle in a homogeneous electron gas of charge density $n(\mathbf{r})$ [45]. Although the electron density in real systems is usually inhomogeneous, but the LDA method reproduces accurate results for a large amount of materials and their properties. One of reasons can be the fact that the electron density in the inter-atomic area is roughly constant and the LDA method satisfies some of important properties and constrains in this case [46–49].

A further improvement for the exchange-correlation energy can be achieved by considering the gradient corrections of the density in the system. The exchange-correlation energy in the

so-called generalized gradient approximation (GGA) has the form [50]

$$E_{xc}[n(\mathbf{r})] = \int d\mathbf{r} \epsilon_{xc}^{\text{GGA}}[n(\mathbf{r}), \nabla n(\mathbf{r})]n(\mathbf{r}). \quad (3.10)$$

The main high light of the GGA is that it reproduces the equilibrium volume of 3d metals better than the LDA[51–53]. However, there are different forms of GGA (PBE [54], PBEsol [55] and PW91 [56]) functional available for some of current computational packages, therefore, it is always necessary to choose the functional by comparison from experiments, as discussed in in Chapter 6.

3.1.4 Wave function methods and projector augmented wave method

Solid state system which has a crystalline structure can be characterized by a spacial periodicity, meaning that the electrons interact with a periodic external potential of the nuclei. One of the solution to solve the Schrödinger equation for this periodic system is Bloch's theorem , which can be written as [57, 41]

$$\psi_n(\mathbf{k}, \mathbf{r}) = \exp(i\mathbf{k} \cdot \mathbf{r})\mu_{\mathbf{k}}(\mathbf{r}), \quad (3.11)$$

here \mathbf{k} is a vector in reciprocal space within the primitive cell of the crystal, while vector \mathbf{r} is called real space. $\exp(i\mathbf{k} \cdot \mathbf{r})$ is the plane wave and $\mu_{\mathbf{k}}(\mathbf{r})$ is periodic in space with the same periodicity as the crystal. This theorem also indicates that it is possible to try and solve the Schrödinger equation for each value of \mathbf{k} independently.

However, valence wave functions exhibit rapid oscillations near the ion cores due to strong Columb interaction, thereby it requires a large number of Fourier components to describe the wave functions accurately. The projector augmented wave (PAW) approach [58, 59] solves this issue by transforming the rapid oscillating wave functions into smooth wave functions, furthermore, it also provides a way to calculate all-electron properties from the smooth wave functions. The PAW method is one of the most efficient and accurate ways for electronic structure calculations, which has been widely used to estimate various properties of materials [41] and implemented in many codes, for example, the Vienna *ab initio* package (VASP) [60–62].

3.2 Molecular dynamic and embedded-atom method

3.2.1 Molecular dynamic

One way of simulating atoms and molecules is called Molecular Dynamics (MD), which focus on numerical simulations instead of theoretical calculations. The MD simulation method was developed in the late 1950's to study the elastic collisions between hard spheres [63, 64]. The realistic potentials were developed later for liquid argon [65] and liquid water [66] during 1960-1970's. Since 1980s, the MD simulation method has been developed rapidly in materials science, nuclear technology, condensed matter physics fields and so on. Moreover, the MD simulation is also a efficient way to simulate materials on a higher scale than first-principles simulation. [67].

3.2.2 Embedded-atom method

The classical equations of motion has been used within the framework of MD, which can be written

$$f_i = m_i \ddot{r}_i, \quad f_i = \frac{\partial U}{\partial r_i}. \quad (3.12)$$

Where f_i is the force on the atoms, and which is usually derived from a potential energy $U(r_N)$, where $r_N = (r_1, r_2, \dots, r_N)$ represents the atomic coordinates in the system [68].

The potential energy $U(r_N)$ of atoms are usually split into the interactions which consist of 1-body, 2-body, 3-body, and higher body terms:

$$U(r_N) = \sum_i \mu(r_i) + \sum_i \sum_{j>i} v(r_i, r_j) + \dots \quad (3.13)$$

Where $u(r)$ is an external potential field or the effects from the container walls. In most of cases, only low order pair potential $v(r_i, r_j)=v(r_{ij})$ are consider and the higher order body (3-body,...) interactions are neglected [67]. In some simulations for complex system, it is sufficient to use a simple model which can represent the behaviours and the properties of the system. One of the efficient methods is the embedded-atom method (EAM), which is written as following:

$$v^{EAM}(r) = \sum_i \left[F_a \left(\sum_{j \neq i} \rho^\beta(r_{ij}) \right) + \frac{1}{2} \sum_{j \neq i} \phi_{\alpha\beta}(r_{ij}) \right]. \quad (3.14)$$

Here F_a is the embedding energy, which is the energy for inserting an atom, i , into the electron density, ρ_β . The second term is the 2-body potential function. In this work, the EAM potential calculations have been done for the Ni and Ni-H systems within the framework of the extensively parallelized Large-scale Atomic/Molecular Massively Parallel Simulator (LAMMPS) environment [69].

Chapter 4

Overview of this thesis

In this thesis, segregation of hydrogen, its co-segregation with other alloying elements to interfaces in Ni-base face-centered-cubic γ phase as well as hydrogen accumulation in the bulk and at the interfaces have been studied theoretically by means of DFT-based calculations. Furthermore, a comprehensive investigation on the thermodynamic and mechanical stability of Ni_3X precipitates has been carried out to identify the most stable phase structure for each Ni_3X composition, which will be used to study the hydrogen effect on the relevant Ni/precipitate interfaces. The results of thesis can be used to evaluate the effect of key alloying elements on HEDE of both interfaces and the bulk of the selected Ni-base alloys under investigation.

4.1 Solute alloying effect on Ni

The solutes (up to 83 elements) segregation in Ni grain boundary (GB) and free surface (FS) as well as their effect on the cohesion of GB have been clarified by literature search. Based on this study, the GB segregation energies of solutes within first three layer of Ni $\Sigma 5$ GB has been calculated for obtaining the knowledge of solute segregation energy distribution in the Ni GB. Furthermore, the solute effects on the Ni bulk lattice strengthening and GB cohesion have been investigated by DFT calculations and it is found that there is a linear correlation between lattice strengthening and GB cohesion enhancement by the solute alloying. The detailed discussions and results are presented in [Chapter 5](#) .

4.2 Co-segregation of H-solute to Ni grain boundary

The synergistic effect of co-segregation of H and other solutes to the Ni GB play an important role in the hydrogen embrittlement of Ni-base alloys. Therefore, the co-segregation of H-Mo,

H-C, and H-S to the Ni $\Sigma 5$ GB and the effects of segregated solute pairs on the GB cohesion have been investigated in detail. In the case of H-Mo and H-C co-segregation, it is found that both Mo and C contribute to the reduction of hydrogen-induced de-cohesion on GB, it is also indicated that H-Mo and H-C interactions in the bulk and at the GB are very similar and can be neglected in most of cases of co-segregation. For the H-S co-segregation to the Ni GB, the intergranular failure of Ni single GB has been investigated employing DFT calculations and micro cantilever bending test by our experimental partner. The kinetics of H and S segregation to the Ni GB have been modelled with segregation energy input from DFT calculations. The overall work reveals that the amount of segregated solute to the GB plays a critical role in the severity of the crack propagation. The detailed discussions and results are presented in **Chapter 6** and **Chapter 7**.

4.3 Hydrogen clustering at defects in Ni

Stability of hydrogen clusters at crystallographic defects in Ni has been recently reported in a number of theoretical density functional theory investigations at 0 K. It has been suggested that hydrogen atoms can accumulate at such defects as vacancies and grain boundaries in a form of clusters containing up to six hydrogen atoms and that the formation of the hydrogen agglomerations can have a significant impact on the hydrogen embrittlement (HE) processes in Ni-base alloys. In this work, we employ a combination of density functional theory calculations and embedded atom method simulations to investigate the stability of H clusters at 0 K as well as finite temperatures. We show that stability of H clusters at structural defects of Ni is limited to temperatures below 300 K and that their appearance at the ambient temperature and therefore an impact on possible HE mechanisms is unlikely. The detailed discussions and results are presented in **Chapter 8**.

4.4 Thermodynamic and mechanical stability of Ni₃X-type precipitate

Ni₃X-type intermetallic compounds, often referred to as γ'' , γ' , and η precipitates in Ni-base alloys, are main second phase in precipitate-hardened Ni-base alloys. However, Ni-base alloys are usually composed of multiple alloying elements, which makes the investigation of the phase stability in compositionally complex alloys even more complicated as the phase formation is governed by the phase competition between multiple phases and solutes. In the last part of this thesis, thermodynamic and mechanical stability of Ni₃X (X=Al, Ti, Nb, Mo, Fe, and

Cr) compounds has been determined by density functional theory calculations of formation enthalpies and elastic properties of their L1₂, D0₂₂ and D0₂₄ phases. In addition, we have investigated the site preference behavior of Al, Ti, Nb, Mo, Fe, and Cr solutes in the L1₂-structure Ni₃Al, Ni₃Ti, and Ni₃Nb intermetallic compounds and used this information to investigate the solubility of the aforementioned alloying elements. The results of this part will be used to study the hydrogen effect on the relevant Ni/precipitate interfaces in the future work. The detailed discussions and results are presented in **Chapter 9**.

References

- [1] W. H. Johnson, *Proc. R. Soc.* 23 (1875) 168–179.
- [2] K. Takai, H. Shoda, H. Suzuki, M. Nagumo, *Acta Mater.* 56 (2008) 5158 – 5167.
- [3] I. M. Robertson, P. Sofronis, A. Nagao, M. L. Martin, S. Wang, D. W. Gross, K. E. Nygren, *Metall. Mater. Trans. A* 46 (2015) 2323–2341.
- [4] M. Nagumo, *Fundamentals of hydrogen embrittlement*, Springer, 2016.
- [5] R. A. Carneiro, R. C. Ratnapuli, V. de Freitas Cunha Lins, *Mater. Sci. Eng. A* 357 (2003) 104 – 110.
- [6] M. R. Louthan, *J. Fail. Anal. Prev.* 8 (2008) 289–307.
- [7] P. A. Tipler, R. Llewellyn, *Modern Physics*, W. H. Freeman and Company, New York, 2008.
- [8] F. Martin, X. Feaugas, A. Oudriss, D. Tanguy, L. Briottet, J. Kittel, in: C. Blanc, I. Aubert (Eds.), *Mechanics - Microstructure - Corrosion Coupling*, Elsevier, 2019, pp. 171 – 197.
- [9] S. Lynch, *Corrosion Reviews* 37 (2019) 377–395.
- [10] C. D. Beachem, *Metall. Mater. Trans. B* 3 (1972) 441–455.
- [11] A. Pundt, R. Kirchheim, *Ann. Rev. Mater. Res.* 36 (2006) 555–608.
- [12] M. Nagumo, *ISIJ International* 41 (2001) 590–598.
- [13] M. Nagumo, *Mater. Sci. Tech.* 20 (2004) 940–950.
- [14] S. Lynch, *Acta Metall.* 36 (1988) 2639 – 2661.
- [15] L. B. Pfeil, H. C. H. Carpenter, *Proc. Royal Soc. Lond* 112 (1926) 182–195.
- [16] M. Dadfarnia, A. Nagao, S. Wang, M. L. Martin, B. P. Somerday, P. Sofronis, *Int. J. Fract.* 196 (2015) 223–243.
- [17] A. Turnbull, *Int. J. Hydrog. Energy* 40 (2015) 16961 – 16970, special issue on 1st International Conference on Hydrogen Storage, Embrittlement and Applications (Hy-SEA 2014), 26-30 October 2014, Rio de Janeiro, Brazil.
- [18] J. E. Angelo, N. R. Moody, M. I. Baskes, *Model. Simul. Mater. Sc.* 3 (1995) 289.
- [19] V. Razumovskiy, A. Lozovoi, I. Razumovskii, *Acta Mater.* 82 (2015) 369 – 377.

- [20] D. Scheiber, R. Pippan, P. Puschnig, L. Romaner, *Model. Simul. Mater. Sci. Eng.* 24 (2016) 035013.
- [21] M. Yamaguchi, M. Shiga, H. Kaburaki, *J. Phys.: Condens. Matter* 16 (2004) 3933.
- [22] M. Yamaguchi, M. Shiga, H. Kaburaki, *J. Phys. Soc. Jpn.* 73 (2004) 441–449.
- [23] D. D. Stefano, M. Mrovec, C. Elsässer, *Acta Mater.* 98 (2015) 306 – 312.
- [24] M. S. Daw, M. I. Baskes, *Phys. Rev. Lett.* 50 (1983) 1285–1288.
- [25] A. Alvaro, I. T. Jensen, N. Kheradmand, O. Løvvik, V. Olden, *Int. J. Hydrog. Energy* 40 (2015) 16892 – 16900.
- [26] T. B. Bhat, V. Arunachalam, *Proceedings of the Indian Academy of Sciences Section C: Engineering Sciences* 3 (1980) 275–296.
- [27] J. Pelleg, *Mechanical properties of materials*, volume 190, Springer Science & Business Media, 2012.
- [28] P. Lejcek, *Grain boundary segregation in metals*, volume 136, Springer Science & Business Media, 2010.
- [29] W. D. Callister Jr, D. G. Rethwisch, *Fundamentals of materials science and engineering: an integrated approach*, John Wiley & Sons, 2012.
- [30] J. R. Rice, J.-S. Wang, *Mater. Sci. Eng. A* 107 (1989) 23 – 40.
- [31] D. Raabe, M. Herbig, S. Sandlöbes, Y. Li, D. Tytko, M. Kuzmina, D. Ponge, P.-P. Choi, *Current Opinion in Solid State and Materials Science* 18 (2014) 253 – 261.
- [32] M. C. Chaturvedi, Y. fang Han, *Metal Sci.* 17 (1983) 145–149.
- [33] M. Chaturvedi, Y. Han, *Mater. Sci. Eng.* 89 (1987) L7 – L10.
- [34] M. J. Donachie, S. J. Donachie, *Superalloys: A technical guide*, ASM international, 2002.
- [35] R. Stevens, P. Flewitt, *Mater. Sci. Eng.* 37 (1979) 237 – 247.
- [36] J. V. Sluytman, T. Pollock, *Acta Mater.* 60 (2012) 1771 – 1783.
- [37] C. T. Sims, N. S. Stoloff, W. C. Hagel, *superalloys II*, Wiley New York, 1987.
- [38] K. Ohira, Y. Kaneno, T. Takasugi, *Mater. Sci. Eng. A* 399 (2005) 332 – 343.
- [39] S. He, *Interactions and phase stability in Ni-rich binary alloys*, Licentiate dissertation at KTH Royal Institute of Technology, Sweden, 2016.
- [40] E. Schrödinger, *Phys. Rev.* 28 (1926) 1049–1070.
- [41] R. M. Martin, *Electronic structure: basic theory and practical methods*, Cambridge university press, 2004.
- [42] M. Born, K. Huang, *Dynamical theory of crystal lattices*, Clarendon Press, 1954.
- [43] P. Hohenberg, W. Kohn, *Phys. Rev.* 136 (1964) B864.
- [44] W. Kohn, L. J. Sham, *Phys. Rev.* 140 (1965) A1133.
- [45] D. M. Ceperley, B. Alder, *Phys. Rev. Lett.* 45 (1980) 566.
- [46] O. Gunnarsson, B. Lundqvist, *Phys. Rev. B* 13 (1976) 4274.

- [47] J. Harris, *Phys. Rev. A* 29 (1984) 1648.
- [48] J. P. Perdew, *Phys. Rev. Lett.* 55 (1985) 1665.
- [49] A. V. Ruban, I. Abrikosov, *Rep. Prog. Phys.* 71 (2008) 046501.
- [50] J. P. Perdew, K. Burke, M. Ernzerhof, *Phys. Rev. Lett.* 77 (1996) 3865.
- [51] A. Khein, D. J. Singh, C. J. Umrigar, *Phys. Rev. B* 51 (1995) 4105.
- [52] V. Ozoliņš, M. Körling, *Phys. Rev. B* 48 (1993) 18304.
- [53] L. Vitos, B. Johansson, J. Kollár, H. L. Skriver, *Phys. Rev. B* 62 (2000) 10046.
- [54] J. P. Perdew, K. Burke, M. Ernzerhof, *Phys. Rev. Lett.* 77 (1996) 3865–3868.
- [55] J. P. Perdew, A. Ruzsinszky, G. I. Csonka, O. A. Vydrov, G. E. Scuseria, L. A. Constantin, X. Zhou, K. Burke, *Phys. Rev. Lett.* 100 (2008) 136406.
- [56] J. P. Perdew, J. A. Chevary, S. H. Vosko, K. A. Jackson, M. R. Pederson, D. J. Singh, C. Fiolhais, *Phys. Rev. B* 46 (1992) 6671–6687.
- [57] D. Sholl, J. A. Steckel, *Density functional theory: A practical introduction*, John Wiley & Sons, 2009.
- [58] P. E. Blöchl, *Phys. Rev. B* 50 (1994) 17953–17979.
- [59] J. Hafner, *J. Comput. Chem.* 29 (2008) 2044–2078.
- [60] G. Kresse, J. Hafner, *Phys. Rev. B* 48 (1993) 13115–13118.
- [61] G. Kresse, J. Furthmüller, *Comput. Mater. Sci.* 6 (1996) 15–50.
- [62] G. Kresse, J. Furthmüller, *Phys. Rev. B* 54 (1996) 11169.
- [63] B. J. Alder, T. E. Wainwright, *J. Chem. Phys.* 27 (1957) 1208–1209.
- [64] B. J. Alder, T. E. Wainwright, *J. Chem. Phys.* 31 (1959) 459–466.
- [65] A. Rahman, *Phys. Rev.* 136 (1964) A405–A411.
- [66] F. H. Stillinger, A. Rahman, *The Journal of Chemical Physics* 60 (1974) 1545–1557.
- [67] H. J. C. Berendsen, in: P. Deuffhard, J. Hermans, B. Leimkuhler, A. E. Mark, S. Reich, R. D. Skeel (Eds.), *Computational Molecular Dynamics: Challenges, Methods, Ideas*, Springer Berlin Heidelberg, Berlin, Heidelberg, 1999, pp. 3–36.
- [68] M. P. Allen, in: H. G. K. K. Norbert Attig, Kurt Binder (Ed.), *Computational soft matter: from synthetic polymers to proteins*, volume 23, NIC Series, 2004, pp. 1–28.
- [69] S. Plimpton, *J. Comput. Phys.* 117 (1995) 1 – 19.

Part II

Results and discussion

Chapter 5

The effects of solute solid solution and grain boundary segregation on the strengthening in Ni

5.1 Introduction

Nickel-base alloys (NBAs) exhibit excellent mechanical strength, resistance to thermal creep deformation, as well as resistance to corrosion or oxidation due to introducing of alloying elements [1, 2] and designing of micro-structures [3, 4]. The development of new NBAs is a time consuming and expensive process, the ability to select promising alloy compositions for further testing while minimizing the amount of experimental testing that occurs would lead to financial and time savings [5]. First-principles calculations can give fundamental understanding of the solute solubility in bulk and GB segregation, in order to predict the mechanical response of materials due to alloying additions. Therefore, the comprehensive study of solute alloying effects on the NBAs by simulations is necessary to select solute elements and design chemical compositions for NBAs.

The solubility of various elements in Ni has been evaluated by a size factor function which is defined as the atomic radius difference between the solute atom and the solvent atom Ni [6]. Roth *et al.* found that the yield stress of the Ni solid solution alloys could be modeled successfully using the Feltham equation [5]. Mishima *et al.* [7] used compression testing of Ni containing small ternary additions of other elements to determine experimentally the increase in the strength of *fcc* Ni by solid solution strengthening. The temperature-dependent stacking fault energy [8], elastic constants [9], and substitution enthalpies [10] of transition metals have been studied by using DFT to evaluate the mechanical and thermodynamic stability of Ni matrix

phase. Chemomechanical effects including plastic deformation by dislocation or vacancy generation are discussed qualitatively by Kirchheim *et al* [11]. Goodfellow [12] reviewed the different strengthening mechanisms occurring in polycrystalline Ni-based superalloys and how these may be modelled, with the aim of revealing the gaps in the literature.

The intergranular fracture along the Ni GB is the preferential mode of failure, while the segregation of elements to GB play an important role to enhance or suppress intergranular brittleness [13–15]. Yamaguchi *et al* [16] and Razumovskiy *et al* [17, 18] studied the segregation for a large number of elements in symmetric grain boundaries $\Sigma 5$ Ni GB and their strengthening effect on the GB cohesion by means of first-principles calculations. Some embrittler species, like: H [19], S [20, 21], P [22], and enhancer elements, like: C [23], have already been studied in detail. Gibson *et al.* published an overview [14] and model development [13] on solute-induced changes in grain boundary cohesion. Geng *et al.* have predicted the embrittlement potency of a large number of transition metals are presented for the Ni $\Sigma 5(210)$ GB [24]. Matsui *et al.* have studied the GB segregation energies, interaction energy between S and solute, and embrittling potency energy by first-principles calculations for 57 Ni-based solid solutions [25]. Lejček *et al.* have investigated segregation in Fe and Ni and by DFT simulation [26–28] and they show that the entropy of grain boundary segregation is a very important quantity which cannot be neglected in thermodynamic considerations as it plays a crucial role [29, 30]. The GB solute segregation energies for a comprehensive set of solutes have also been studied for other metals, such as, W [31, 32], Mo [32].

Nowadays, high-throughput calculations shed light on materials design, such as, for vacancy diffusion database in fcc and hcp metals [33, 34], defect in fcc Cobalt [35], high entropy alloys [36], intermetallic compounds [37], new ternary superalloys [38]. With the state-of-art techniques, we present a high-throughput investigation of the solute alloying effect on the strengthening in Ni. The aim of this work is to provide applicable information of solutes alloying effect on the Ni lattice and GB cohesion. The solute solid solution effect for a comprehensive set of species in Ni bulk and solutes segregation effect on Ni $\Sigma 5(012)$ GB have been investigated using first-principles calculations.

5.2 Methodology

5.2.1 Density functional theory

Spin polarized density functional theory (DFT) calculations have been performed using the projector-augmented-wave (PAW) [39, 40] method as implemented in the Vienna *Ab initio* simulation package (VASP) [41, 42]. We have used the Perdew-Burke-Ernzerhof (PBE) form of

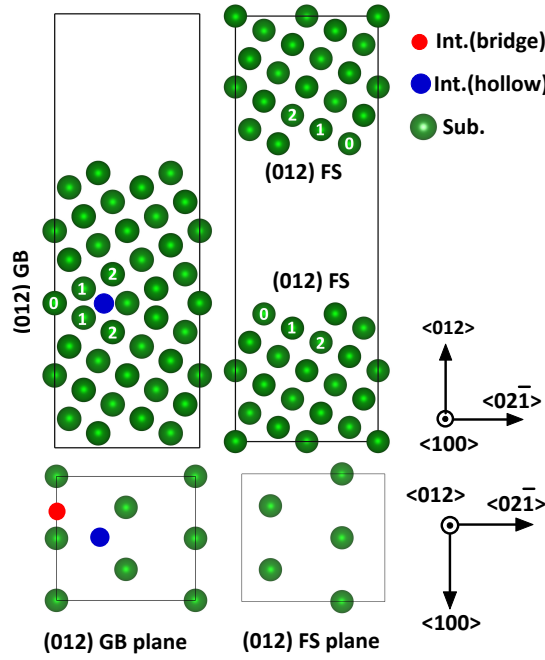


Fig. 5.1 Geometry of $\Sigma 5(012)[100]$ symmetric tilt GB and (012) FS.

generalized gradient approximation (GGA) to the exchange-correlation potential[43] The plane-wave basis set cutoff energy has been set to 400 eV. The convergence criteria of self-consistent calculations have been set to 10^{-5} eV/cell for the total energy and to 9×10^{-3} eV/Å for the atomic forces. The integration over the Brillouin zone has been done using the $4 \times 4 \times 1$ Monkhorst-Pack k -mesh[44] for all slab geometries and using the $4 \times 4 \times 4$ k -mesh in the $3 \times 3 \times 3 \times$ [conventional fcc cell] supercell (SC) calculations. The lattice parameter has been fixed to the equilibrium value of 3.515 Å in all slab and SC calculations while only the ions have been allowed to relax.

5.2.2 Calculation of energetic quantities

5.2.2.1 Solute solution energy in bulk Ni

In the fcc Ni, there are three potential locations for solutes: (i) the two interstitial sites, *i.e.*, the octahedral site (OS) and the tetrahedral site (TS) and (ii) the substitutional site. The solution energy for one solute at an interstitial site (OS or TS) is calculated by using[45, 46]:

$$E_s^{\text{int}} = E_{\text{bulk}}^{\text{X}}[M; 1] - E_{\text{bulk}}^{\text{Ni}}[M; 0] - E_{\text{ref}}^{\text{X}} \quad (5.1)$$

and for one solute at the substitutional sites:

$$E_s^{\text{sub}} = E_{\text{bulk}}^{\text{X}}[M-1;1] - E_{\text{bulk}}^{\text{Ni}}[M;0] + E_{\text{ref}}^{\text{Ni}} - E_{\text{ref}}^{\text{X}}, \quad (5.2)$$

where $E_{\text{bulk}}^{\text{X}}[M;1]$ and $E_{\text{bulk}}^{\text{X}}[M-1;1]$ are the total energies of the supercell with one solute at the interstitial site and one at the substitutional site, respectively. $E_{\text{bulk}}^{\text{Ni}}[M;0]$ is associated with the total energy of the pure supercell with M Ni atoms. $E_{\text{ref}}^{\text{Ni}}$ and $E_{\text{ref}}^{\text{X}}$ are total energies of Ni and solute X at their ground states.

5.2.2.2 Solute segregation energy at GB

We define the GB and FS impurity segregation energies for two representative cases when:

- (i) a solute occupies an interstitial site in the bulk and at the interface:

$$\begin{aligned} E_{\text{seg}}^{\text{gb}} &= E_{\text{slab}}^{\text{gb}}[N;1] - E_{\text{slab}}^{\text{gb}}[N;0] + \Delta_{\text{bulk}}^{\text{X}}, \\ E_{\text{seg}}^{\text{fs}} &= (E_{\text{slab}}^{\text{fs}}[N;2] - E_{\text{slab}}^{\text{fs}}[N;0])/2 + \Delta_{\text{bulk}}^{\text{X}}; \end{aligned} \quad (5.3)$$

- (ii) a solute occupies a substitutional site in the bulk and at the interface:

$$\begin{aligned} E_{\text{seg}}^{\text{gb}} &= E_{\text{slab}}^{\text{gb}}[N-1;1] - E_{\text{slab}}^{\text{gb}}[N;0] + \Delta_{\text{bulk}}^{\text{Ni} \rightarrow \text{X}}, \\ E_{\text{seg}}^{\text{fs}} &= (E_{\text{slab}}^{\text{fs}}[N-2;2] - E_{\text{slab}}^{\text{fs}}[N;0])/2 + \Delta_{\text{bulk}}^{\text{Ni} \rightarrow \text{X}}; \end{aligned} \quad (5.4)$$

- (iii) a solute occupies a substitutional site in the bulk and an interstitial site at the GB:

$$\begin{aligned} E_{\text{seg}}^{\text{gb}} &= (E_{\text{slab}}^{\text{gb}}[N;1] - E_{\text{slab}}^{\text{gb}}[N;0]) + \Delta_{\text{bulk}}^{\text{Ni} \rightarrow \text{X}} - \epsilon_0, \\ E_{\text{seg}}^{\text{fs}} &= ((E_{\text{slab}}^{\text{fs}}[N;2] - E_{\text{slab}}^{\text{fs}}[N;0]))/2 + \Delta_{\text{bulk}}^{\text{Ni} \rightarrow \text{X}} - \epsilon_0. \end{aligned} \quad (5.5)$$

Here $E_{\text{slab}}^{\text{gb}}[N-1;1]$ and $E_{\text{slab}}^{\text{gb}}[N;1]$ are the total energies of the GB slab with one solute at the substitutional site and at the interstitial site respectively; $E_{\text{slab}}^{\text{fs}}[N-2;2]$ and $E_{\text{slab}}^{\text{fs}}[N;2]$ are the total energies of the FS slab containing 2 solutes (symmetrically distributed on both FS of the slab, see Fig. 5.1) at the substitutional sites and at the interstitial sites respectively; $\Delta_{\text{bulk}}^{\text{Ni} \rightarrow \text{X}} = E_{\text{bulk}}^{\text{Ni}}[M;0] - E_{\text{bulk}}^{\text{X}}[M-1;1]$ is the energy difference (per X atom) between bulk supercells before and after one of the host atoms is replaced by an impurity atom and $\Delta_{\text{bulk}}^{\text{X}} = E_{\text{bulk}}^{\text{Ni}}[M;0] - E_{\text{bulk}}^{\text{X}}[M;1]$ is the same energy difference (per X atom) but for the interstitial case with no host atom being replaced by a solute atom. $\epsilon_0 = E_{\text{bulk}}^{\text{Ni}}[M;0]/M$ is the energy of fcc Ni

per atom. In this paper, we adopt the following sign convention: segregation energy $E_{\text{seg}}^{\text{gb}}$ ($E_{\text{seg}}^{\text{fs}}$) is negative if a solute tends to segregate to an interface.

5.2.2.3 Partial cohesive energy

The cohesive energy of a crystal is defined as the energy required to separate its components into neutral free atoms at infinite separation with the same electronic configuration. It can be obtained as a difference of the total energies of the free atoms, E_{at}^i , and a crystal, E_{cryst} [47]:

$$E_{\text{coh}} = \sum c_i E_{\text{at}}^i - E_{\text{cryst}}, \quad (5.6)$$

where c_i is the impurity concentration.

The partial cohesive energy was introduced in the Ref. [48] as a parameter suitable for characterizing the contribution of an impurity to the bond strengthening in the bulk of an alloy where alloying elements were distributed randomly in the phase, neglecting thereby short-range order effects. It was found a good correlation between partial cohesive energies and alloy resistance to creep rupture on an example single crystal Ni-based alloy [48]. The partial cohesive energy, χ_i , of the i th impurity is defined as the partial derivative of the cohesive energy of the alloy, E_{coh} , with respect to impurity concentration, c_i , evaluated in the limit of pure host crystal:

$$\chi_i = \left. \frac{\partial E_{\text{coh}}}{\partial c_i} \right|_{c \rightarrow 0} \quad (5.7)$$

where $c = \{c_i, i = 0, 1, 2 \dots n\}$ is the vector of the impurity concentrations. We then define the partial cohesive energies, according to Equation 5.6 and 5.7, for two representative cases when

i) a solute occupies an interstitial site in the bulk:

$$\chi_i^{\text{int}} = E_{\text{bulk}}^{\text{Ni}}[M; 0] - E_{\text{bulk}}^{\text{X}}[M; 1] + E_{\text{at}}^i - E_{\text{at}}^{\text{Ni}} + E_{\text{cryst}}^{\text{Ni}}; \quad (5.8)$$

ii) a solute occupies a substitutional site in the bulk:

$$\chi_i^{\text{sub}} = E_{\text{bulk}}^{\text{Ni}}[M; 0] - E_{\text{bulk}}^{\text{X}}[M - 1; 1] + E_{\text{at}}^i - E_{\text{at}}^{\text{Ni}}, \quad (5.9)$$

where $E_{\text{at}}^{\text{Ni}}$ is the total energy (per atom) of Ni at its gaseous state, while $E_{\text{cryst}}^{\text{Ni}}$ is the total energy (per atom) of fcc Ni.

5.2.2.4 GB strengthening energy

The ideal work of separation is a fundamental thermodynamic quantity that controls the mechanical strength of an interface and is defined as the reversible work of decohesion, where any diffusion exchange between the interface and the underlying bulk is suppressed during the decohesion (the fast separation limit) [49, 50]. In this case, the “local” equilibrium is maintained between impurity atoms and the surface layer of the host. This equilibrium corresponds to the impurity chemical potential μ' different from the one in the bulk μ , and the expression for work of separation W_{sep} can be written as[51]

$$W_{\text{sep}} = 2\gamma_0^{\text{fs}} - \gamma_0^{\text{gb}} + (\mu' - \mu)\Gamma_{\text{gb}}, \quad (5.10)$$

where the first two terms on the right side $2\gamma_0^{\text{fs}} - \gamma_0^{\text{gb}}$ correspond to the work of separation of the pure GB, *i.e.*, $W_{\text{sep}}^0 = 2\gamma_0^{\text{fs}} - \gamma_0^{\text{gb}}$, while Γ_{gb} is the number of solute atoms per unit interface area and it is assumed that the impurity distributes evenly between the two newly created surfaces. If we neglect all temperature effects and calculate the change of the Gibbs free energy at 0 K, Equation (6.13) becomes:

$$W_{\text{sep}} = W_{\text{sep}}^0 + (E_{\text{seg}}^{\text{fs}} - E_{\text{seg}}^{\text{gb}})\Gamma_{\text{gb}}. \quad (5.11)$$

In what follows, we evaluate the change of the work of separation η in terms of the GB strengthening energy as introduced in Ref.[17]:

$$\eta = (W_{\text{sep}}^0 - W_{\text{sep}})/\Gamma_{\text{gb}}. \quad (5.12)$$

The parameter η characterizes the cohesive strength of the GB with a segregated solute *sa* compared to the GB without the solute. According to Eq. (6.14), Eq. (6.15) can be rewritten as:

$$\eta = E_{\text{seg}}^{\text{gb}} - E_{\text{seg}}^{\text{fs}}. \quad (5.13)$$

In this paper, we adopt the following sign convention: the strengthening energy parameter η is negative if the solute enhances the GB cohesion.

5.3 Results and discussion

5.3.1 Solutes in bulk Ni

Location of solutes in the fcc lattice of Ni has been determined by means of calculating the solution energy at interstitial site as well as at a substitutional site as described in Section 6.3.1. In Fig. 5.2, we show our DFT calculated solution energy of the interstitial octahedral site and the substitutional solutes in Ni with comparison from literature[1]. Firstly, by comparing our calculated solution energies for a solute locating at octahedral site and at substitutional site, we find that H, B, C, N, and O have lower solution energy at octahedral site, which means a site preference to the interstitial site. One also notes that the solution energies of H, B, C, N, and O at the interstitial site are positive, the same as to the most of substitutional solute in Ni.

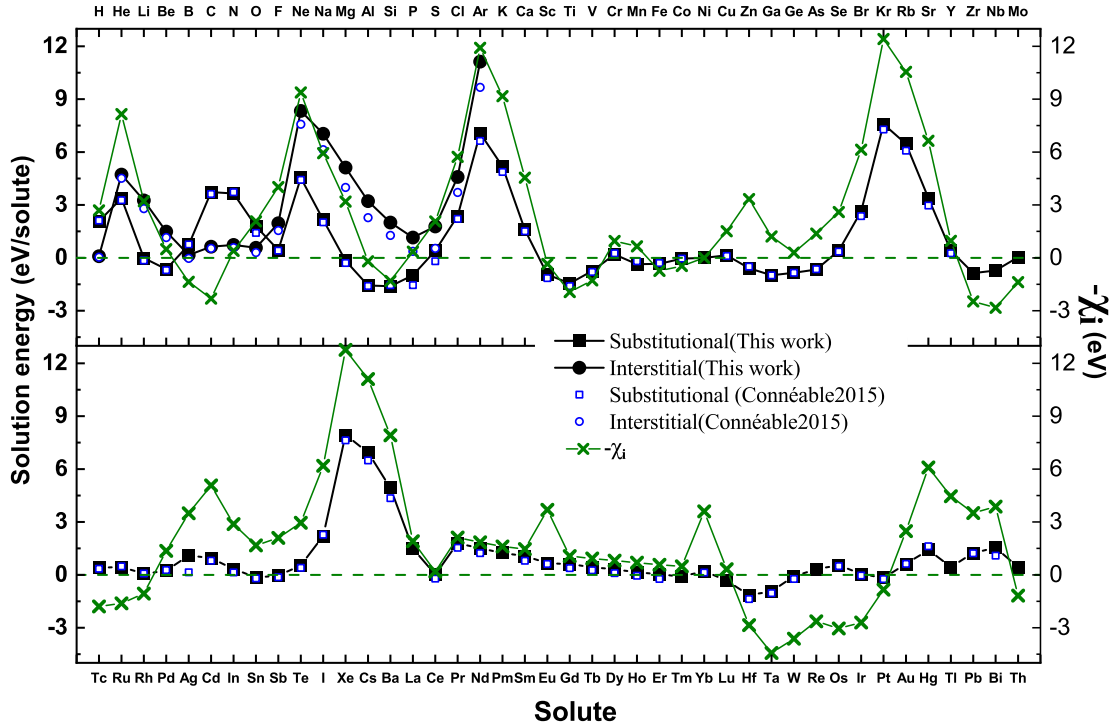


Fig. 5.2 Solution energy and partial cohesive energy of impurities in Ni. The solution energy from literature[1] are also shown for comparison. The upper panel shows the elements form H to Mo , while the lower panel shows the elements from Tc to Bi and Th.

The site preference of H, B, C, N, and O can be understood from simple geometric considerations. The space associated with the interstitial sites in Ni in our calculations can be described by an inscribed sphere of a radius r_{site} of 0.56 \AA for the interstitial octahedral site and of 0.30 \AA for the interstitial tetrahedral site. H has the Slater radii r_{imp} of 0.25 \AA [52], which

accounts for a low solution energy of 0.09 eV at OS of Ni. However, the Slater radius of B, C, N, O are 0.85Å, 0.70Å, 0.65Å, 0.60Å, respectively, which are larger than the OS interstitial volume in Ni. From this perspective, only H can fit both octahedral site and tetrahedral site of bulk Ni.

For other species we have considered in this study, one can see a substitutional site preference. As it has been described by the Hume–Rothery’s rules [53, 54] that the conditions under which an element could dissolve in a metal to form a solid solution are related to two sets of rules: one refers to substitutional solid solutions, and the other refers to interstitial solid solutions. In the case of substitutional solid solutions, the atomic radius of the solute and solvent atoms must differ by no more than 15% and the crystal structures of solute and solvent must be similar, and a metal with lower valency is more likely to dissolve in a metal of higher valency, the solute and solvent should have similar electronegativity. For the interstitial solid solutions, solute atoms should have a radius not larger than 59% of the radius of solvent atoms, and the solute and solvent should have similar electronegativity and valance.

From Fig. 5.2, the calculated solution energy of our selected solute in bulk Ni exactly follows the Hume–Rothery’s rules. We see a negative solution energy for some elements which are located at sublattice of Ni, the trend can be summarized as following: (1) Some of light impurities which have similar atomic radius to Ni, such as, Li, Be, Mg, Al, P, prefer to occupy sublattice of Ni with negative solution energy; (2) In regards to atomic size of transition metals, there is little variation, it turns out that most of transition metals, such as, Sc, Ti, V, Mn, Co, Zn, Ga, Ge, As, Zr, Nb, Sn, Sb, Tm, Lu, Hf, Ta, W, Pt, also have negative solution energy in the Ni.

In Figure 5.2, the calculated values of parameter χ are also shown with solution energies of solutes. It is clear that the most efficient alloying additions to the Ni bulk matrix cohesion are those elements which have negative solution energies in Ni, meaning that the solubles element in bulk Ni strengthen the lattice cohesion of Ni. Among them, we see that *5d* element Hf, Ta, W, Re, Os, and Ir have most strongest effect on the improving on lattice cohesion of Ni. It is also interesting to see that the noble gas element have most detrimental effect on the lattice cohesion of Ni, however, those elements also have quite low solubility in Ni according to the solution energies.

5.3.2 Solute segregation energy in Ni $\Sigma 5(012)$ GB

The information of solute solution obtained from 5.3.1 has been used to calculate solute segregation energies of these solutes to the GB and FS planes (planes corresponding to “L0” sites and the top panel in Fig. 5.1). All sites for solute segregation to “L0” considered in this work are shown in Fig. 5.1 with numbers for substitutional (Sub.) sites and for two types of the interstitial sites in the GB and FS planes: (i) the bridge (Int. bridge) site, which is located at the

middle position of any two nearest Ni atoms in the 100 direction of GB plane; (ii) the hollow (Int. hollow), which is located at the GB core, see Fig. 5.1 or Ref. [55] for details.

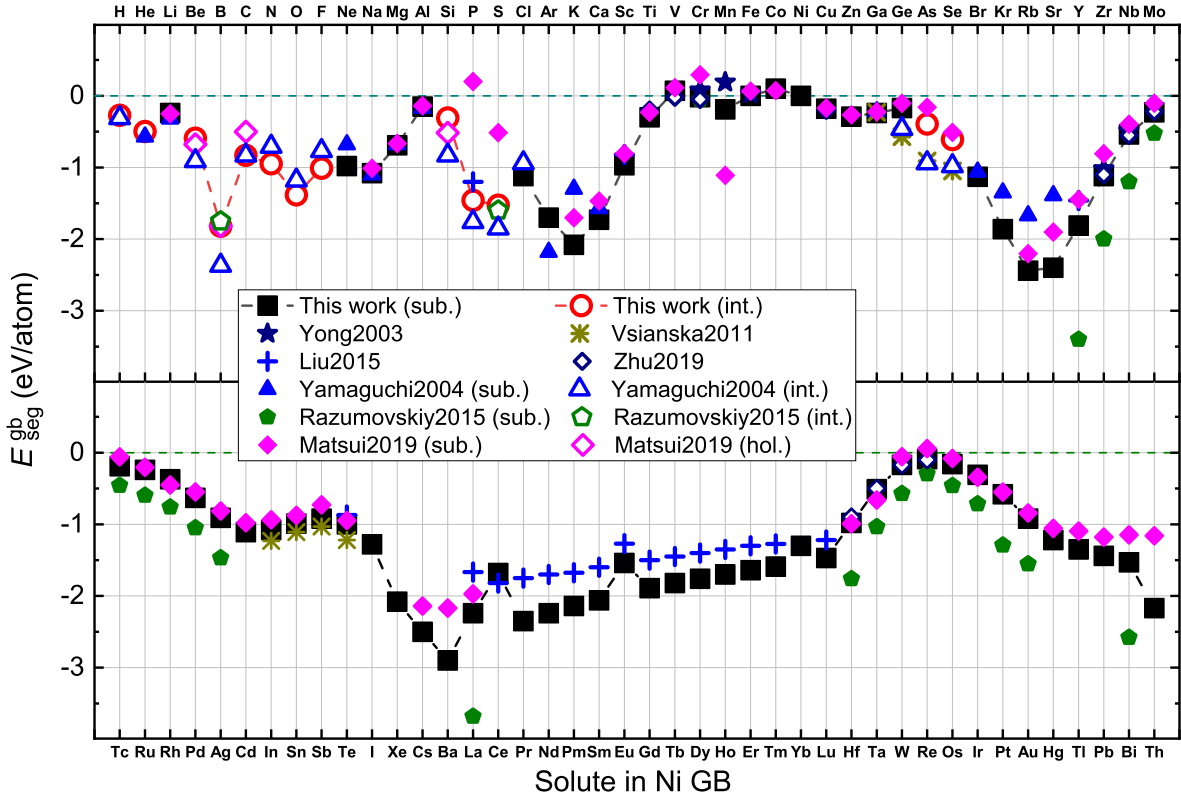


Fig. 5.3 GB segregation energy of solutes located at GB layer (layer "0" in Figure 5.1) of Ni $\Sigma 5(012)$ GB. The literature data are also shown for comparison [16–18, 56, 22, 57–60]. The upper panel shows the elements form H to Mo , while the lower panel shows the elements from Tc to Bi and Th.

Our calculated GB segregation energies for solute segregation to the first layer of GB are shown in Fig. 5.3. As one can see, all of the solutes show a segregation tendency to the Ni $\Sigma 5(012)$ GB, and the similar behavior has been confirmed by some of previous DFT calculations [16–18, 56–60]. However, one still can see some discrepancies for few elements, which is due to the different choices of PAW potentials [16–18], but this would not affect the strengthening energy (see Eq. 5.13) results, as shown in Fig. 5.4. Moreover, our high-throughput calculations for solute segregation also show that the elements located at the middle of the transition metals have lowest segregation energies in each period, and the segregation exhibits a decreasing along the both side of the period.

The site occupancy behavior of solutes in bulk Ni has been shown in Fig. 5.2, it is known that only H, B, C, N, and O occupy the interstitial octahedral site in bulk Ni. The maximal radius inscribed sphere in the ideal Ni $\Sigma 5$ GB is 0.56 \AA , which is same as the sphere size in OS

of Ni, however, due to the expansion of the GB after optimization, this value can be increased by 0.1 Å. As shown in Fig: 5.3, in addition to aforementioned five solutes, He, Be, F, Si, P, S, As, and Se also preference to segregate to the interstitial site of "0" GB layer. However, as shown in Fig. 5.1, there exists two types of interstitial locations at "0" GB layer of $\Sigma 5$ (012) GB [16, 19, 55], *i.e.*, a bridge site which is located at the middle position of two neighboring Ni atoms in the $\langle 100 \rangle$ direction and a hollow site which is located at the GB core. In the case of interstitial solute segregation to the "0" layer of $\Sigma 5$ GB, it is found that H, C, N, and O are stable at the bridge site, while He, Be, F, Si, P, S, As, and Se prefer to segregate to the hollow site.

5.3.3 Alloying effect of solute on the GB cohesion of Ni

In this section, we initially investigate the solutes segregation to GB layer "0" and correspondingly to the FS layer "0" as illustrated in Fig. 5.1 within the framework of Rice-Wang fast-limit separation [49, 50]. The preferential site of each element shown in Fig. 5.3 has been chosen for calculating the strengthening energy parameter η , the results of Fig. 5.4 show that the strength enhancer elements for Ni GB are mostly from transition metals as following: Be, B, C, Al, Ti, V, Cr, Mn, Fe, Co, Zr, Nb, Mo, Tc, Ru, Rh, Hf, Ta, W, Re, Os, Ir, Pt. Moreover, it is found that the elements located at first and last two groups are most detrimental elements for Ni GB in terms of the calculated high strengthening energies. We have also investigated the lanthanide elements in this work, our calculated results indicate that all of them have similar and an embrittling effect on the Ni GB cohesion. We also compare our calculated strengthening energy to the existing literature data [16–18, 25, 56–58, 60] in Fig. 5.4, our results agree well with the values from the aforementioned literature.

5.3.4 Solute distribution at the GB

In the most of current literature, only the first GB layer ("0" in the GB slab of Fig: 5.1) has been considered as the segregation site, therefore, the strengthening effect is only evaluated by one segregation location in GB. In Fig. 5.5, we show the distribution of segregation energies of solutes at first 3 layers of Ni $\Sigma 5$ GB. Both the interstitial and substitutional sites have been taken into account for the segregation locations for all of solutes in this study. In Fig. 5.5), one can see that for most of our selected solutes prefer to segregate to the first layer of GB, which reveals a strong trapping of Ni GB to those elements.

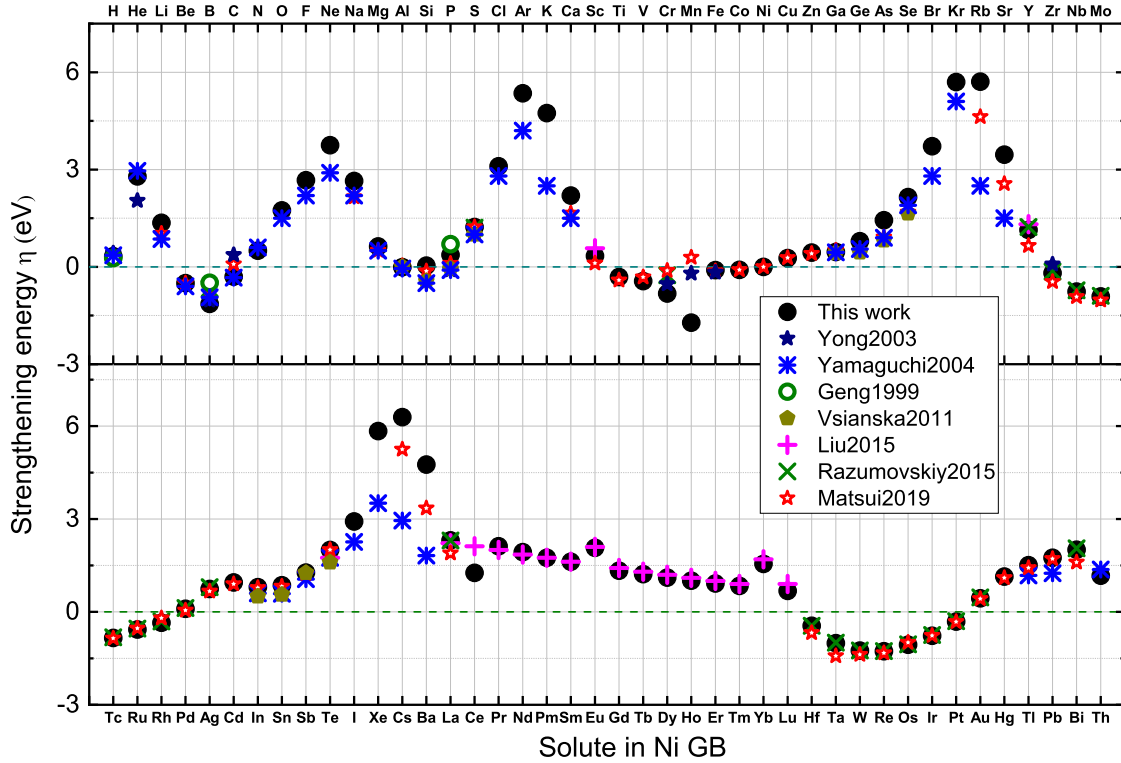


Fig. 5.4 Strengthening energy of solute locating at the first layer of GB. Literature results are also shown for comparison [16–18, 25, 56–58, 60].

5.4 Correlation between bulk cohesion and GB strengthening

The correlation between the partial cohesion energy parameter ($-\chi$) and GB strengthening energy parameter (η) has been plotted in 5.6. One notes that there is a linear correlation of between $-\chi$ and η , indicating that the elements which can enhance the Ni bulk cohesion also contribute to the GB strengthening. As defined in Sections 5.2.2.3 and 5.2.2.4, a positive χ means cohesion enhancement on Ni lattice by adding solute to the fcc Ni matrix, while a negative η indicates a GB strengthening reduction due to solute segregation. As shown in the Fig. 5.6, the elements which can enhance both Ni bulk and GB cohesion are following: C, Al, Si, Ti, V, Fe, Co, Zr, Nb, Mo, Tc, Ru, Rh, Hf, Ta, W, Re, Os, Ir, Pt.

5.5 Conclusion

The site occupancies of solutes as well effects of solute on in bulk and Ni GB have been investigated by means of first-principles calculations. By investigating the solution energies of

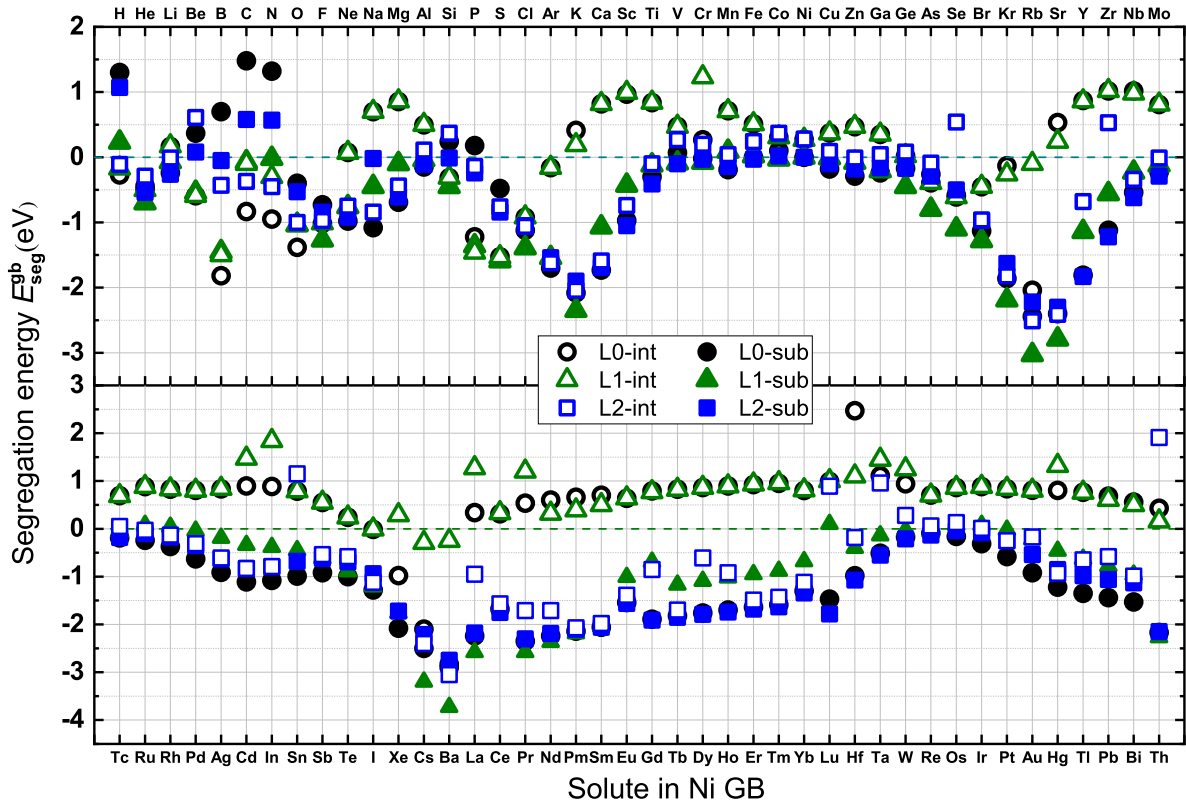


Fig. 5.5 Segregation energy distribution of solutes located at first three GB layers.

solutes in bulk Ni, we have shown that only H, B, C, N, O occupy the octahedral interstitial site in Ni, other elements of our selected list take the sublattice of Ni. Furthermore, our calculated partial cohesive energies for selected solutes show there is a linear correlation between the solute solution energy and partial cohesive energy in Ni.

The segregation and strengthening energy potency of solutes in Ni GB have also been calculated. We show our results for solute GB segregation energies and strengthening energies with literature comparison, moreover, we also consider the solute distribution within the first 3 layers of the GB region, which indicates a different segregation tendency of solutes in the GB.

References

- [1] D. Connétable, É. Andrieu, D. Monceau, *Comput. Mater. Sci.* 101 (2015) 77–87.
- [2] M. Detrois, K. A. Rozman, P. D. Jablonski, J. A. Hawk, in: *Proceedings of the 9th International Symposium on Superalloy 718 & Derivatives: Energy, Aerospace, and Industrial Applications*, Springer, pp. 421–437.
- [3] G. P. Sabol, R. Stickler, *Phys. Stat. Sol. (b)* 35 (1969) 11–52.

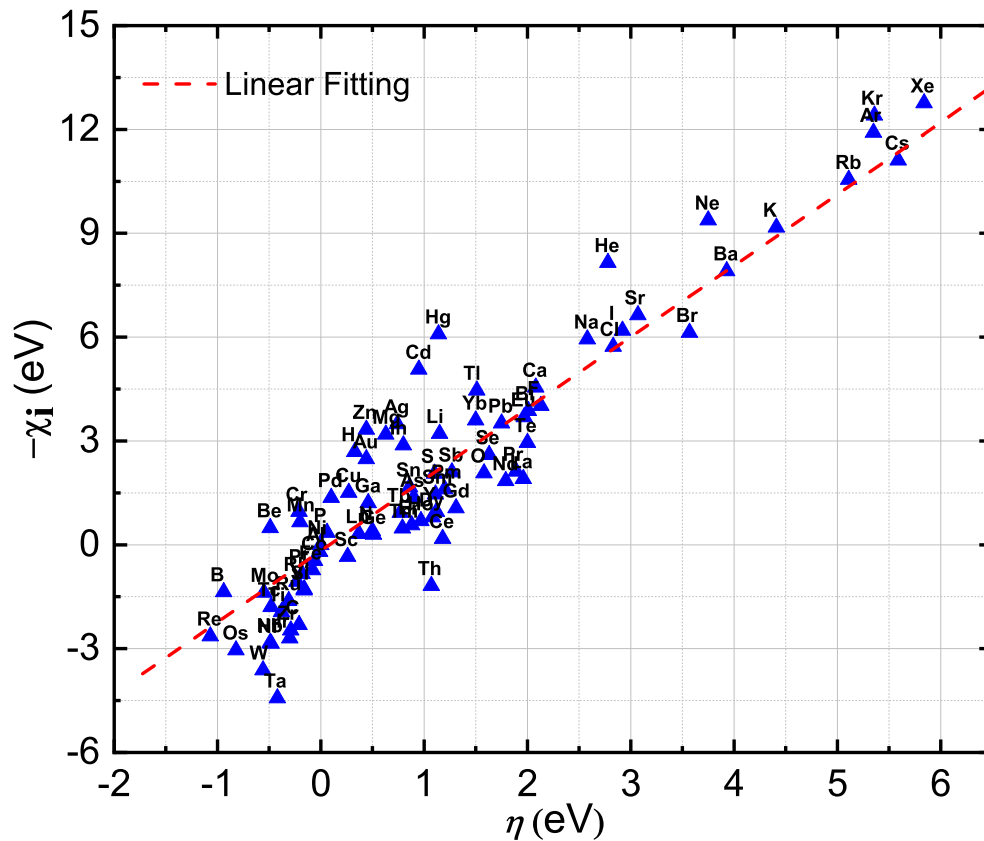


Fig. 5.6 The correlation between strengthening energy and partial cohesive energy.

- [4] A. Drexler, B. Oberwinkler, S. Primig, C. Turk, E. Povoden-Karadeniz, A. Heinemann, W. Ecker, M. Stockinger, *Mater. Sci. Eng. A* 723 (2018) 314 – 323.
- [5] H. A. Roth, C. L. Davis, R. C. Thomson, *Metallurgical and Materials Transactions A* 28 (1997) 1329–1335.
- [6] A. K. Jena, M. C. Chaturvedi, *J. Mater. Sci.* 19 (1984) 3121–3139.
- [7] Y. Mishima, S. Ochiai, N. Hamao, M. Yodogawa, T. Suzuki, *Trans. Japan Inst. Metals* 27 (1986) 656–664.
- [8] S. L. Shang, W. Y. Wang, Y. Wang, Y. Du, J. X. Zhang, A. D. Patel, Z. K. Liu, *Journal of Physics: Condensed Matter* 24 (2012) 155402.
- [9] B. Lu, C. Wang, *Chin. Phys. B* 27 (2018) 077104.
- [10] W. Chen, W. Xing, H. Ma, X. Ding, X.-Q. Chen, D. Li, Y. Li, *Calphad* 61 (2018) 41–49.
- [11] R. Kirchheim, B. Somerday, P. Sofronis, *Acta Mater.* 99 (2015) 87 – 98.
- [12] A. J. Goodfellow, *Materials Science and Technology* 34 (2018) 1793–1808.
- [13] M. A. Gibson, C. A. Schuh, *Acta Mater.* 95 (2015) 145 – 155.

- [14] M. A. Gibson, C. A. Schuh, *Scr. Mater.* 113 (2016) 55 – 58.
- [15] M. A. Gibson, C. A. Schuh, *Data in Brief* 6 (2016) 143 – 148.
- [16] M. Yamaguchi, M. Shiga, H. Kaburaki, *J. Phys.: Condens. Matter* 16 (2004) 3933.
- [17] V. Razumovskiy, A. Lozovoi, I. Razumovskii, *Acta Mater.* 82 (2015) 369 – 377.
- [18] V. Razumovskiy, A. Lozovoi, I. Razumovskii, *Acta Materialia* 106 (2016) 401 – 402.
- [19] M. Yamaguchi, M. Shiga, H. Kaburaki, *J. Phys. Soc. Jpn.* 73 (2004) 441–449.
- [20] M. Yamaguchi, M. Shiga, H. Kaburaki, *Science* 307 (2005) 393–397.
- [21] M. Yamaguchi, M. Shiga, H. Kaburaki, *Mater. Trans.* 47 (2006) 2682–2689.
- [22] W. Liu, C. Ren, H. Han, J. Tan, Y. Zou, X. Zhou, P. Huai, H. Xu, *Journal of Applied Physics* 115 (2014) 043706.
- [23] D. J. Siegel, J. Hamilton, *Acta Mater.* 53 (2005) 87 – 96.
- [24] W. T. Geng, A. J. Freeman, G. B. Olson, *Phys. Rev. B* 63 (2001) 165415.
- [25] I. Matsui, Y. Hisai, T. Uesugi, N. Omura, Y. Takigawa, K. Higashi, *Materialia* 6 (2019) 100312.
- [26] P. Lejček, M. Šob, *J. Mater. Sci.* 49 (2014) 2477–2482.
- [27] P. Lejček, S. Hofmann, *Journal of Physics: Condensed Matter* 28 (2016) 064001.
- [28] P. Lejček, S. Hofmann, V. Paidar, *Materials* 12 (2019) 492.
- [29] P. Lejčobek, M. Šobob, V. Paidar, *Progress in Materials Science* 87 (2017) 83 – 139.
- [30] P. Lejček, M. Všíanská, M. Šob, *Journal of Materials Research* 33 (2018) 2647–2660.
- [31] X. Wu, Y.-W. You, X.-S. Kong, J.-L. Chen, G.-N. Luo, G.-H. Lu, C. Liu, Z. Wang, *Acta Materialia* 120 (2016) 315 – 326.
- [32] D. Scheiber, R. Pippan, P. Puschnig, A. Ruban, L. Romaner, *International Journal of Refractory Metals and Hard Materials* 60 (2016) 75 – 81.
- [33] T. Angsten, T. Mayeshiba, H. Wu, D. Morgan, *New J. Phys.* 16 (2014) 015018.
- [34] C. Wolverton, V. Ozoliņš, *Phys. Rev. B* 73 (2006) 144104.
- [35] S. S. Naghavi, V. I. Hegde, A. Saboo, C. Wolverton, *Acta Mater.* 124 (2017) 1 – 8.
- [36] Y. Lederer, C. Toher, K. S. Vecchio, S. Curtarolo, *Acta Mater.* 159 (2018) 364 – 383.
- [37] A. O. Oliynyk, A. Mar, *Accounts of Chemical Research* 51 (2018) 59–68, PMID: 29244479.
- [38] C. Nyshadham, C. Oses, J. E. Hansen, I. Takeuchi, S. Curtarolo, G. L. Hart, *Acta Mater.* 122 (2017) 438 – 447.
- [39] P. E. Blöchl, *Phys. Rev. B* 50 (1994) 17953.
- [40] G. Kresse, D. Joubert, *Phys. Rev. B* 59 (1999) 1758.
- [41] G. Kresse, J. Hafner, *Phys. Rev. B* 48 (1993) 13115–13118.
- [42] G. Kresse, J. Furthmüller, *Comput. Mater. Sci.* 6 (1996) 15 – 50.
- [43] J. P. Perdew, K. Burke, M. Ernzerhof, *Phys. Rev. Lett.* 77 (1996) 3865–3868.

- [44] H. J. Monkhorst, J. D. Pack, *Phys. Rev. B* 13 (1976) 5188–5192.
- [45] B. Drittler, M. Weinert, R. Zeller, P. H. Dederichs, *Phys. Rev. B* 39 (1989) 930–939.
- [46] A. V. Ponomareva, Y. N. Gornostyrev, I. A. Abrikosov, *Phys. Rev. B* 90 (2014) 014439.
- [47] C. Kittel, *Introduction to Solid State Physics*, 8th ed., John Wiley & Sons, Inc, 2004.
- [48] I. Razumovskii, A. Ruban, V. Razumovskiy, A. Logunov, V. Larionov, O. Ospennikova, V. Poklad, B. Johansson, *Mater. Sci. Eng. A* 497 (2008) 18 – 24.
- [49] J. R. Rice, R. Thomson, *Philos. Mag. A* 29 (1974) 73–97.
- [50] J. R. Rice, J.-S. Wang, *Mater. Sci. Eng. A* 107 (1989) 23 – 40.
- [51] A. Y. Lozovoi, A. T. Paxton, M. W. Finnis, *Phys. Rev. B* 74 (2006) 155416.
- [52] J. C. Slater, *J Chem. Phys.* 41 (1964) 3199–3204.
- [53] W. Hume-Rothery, H. M. Powell, *Z. Krist.-Cryst. Materi.* 91 (1935) 23–47.
- [54] W. Hume-Rothery, *The structures of alloys of iron: an elementary introduction*, Pergamon Press, 1966.
- [55] S. He, W. Ecker, R. Pippan, V. I. Razumovskiy, *Comput. Mater. Sci.* 167 (2019) 100 – 110.
- [56] G. Young, R. Najafabadi, W. Strohmayer, D. Baldey, B. Hamm, J. Harris, J. Sticht, E. Wimmer, *Tech. Report LM-03K047*, NASA. (June 16, 2003).
- [57] W. Liu, H. Han, C. Ren, H. Yin, Y. Zou, P. Huai, H. Xu, *Comput. Mater. Sci.* 96 (2015) 374 – 378.
- [58] M. Váňanský, M. Á ob, *Progress in Materials Science* 56 (2011) 817 – 840, *festchrift Vaclav Vitek*.
- [59] I. Matsui, Y. Hisai, T. Uesugi, N. Omura, Y. Takigawa, K. Higashi, *Materialia* 6 (2019) 100312.
- [60] L. Zhu, J. Zhou, H. Yang, Z. Sun, *J. Alloys Compd.* 795 (2019) 343 – 350.

Chapter 6

Hydrogen-enhanced decohesion mechanism of the special $\Sigma 5(012)$ [100] grain boundary in Ni with Mo and C solutes

6.1 Introduction

Hydrogen embrittlement (HE) was found in 1875 by Johnson in the experiment of the effect of acid on the fracture properties of iron and steel[1]. Since then, it has been found that hydrogen can also embrittle many other materials including Ni and its alloys [2–4]. Nickel-based alloys (NBA) are often made for highly corrosive environment applications and HE can have a dramatic effect on their performance in many cases. In the presence of hydrogen, the failure mode in NBAs can be characterized by failure along grain boundaries (GBs) and at dislocation slip band intersections[5]. H can effectively reduce the activation enthalpy of dislocation slip in Ni [6] and reduce its elastic modulus by 20% [7]. The latter has been partly attributed to hydrogen trapped at defects and the effect of dissolved interstitial hydrogen in the lattice[7].

The origin of HE is partly associated with the aforementioned phenomena, and it has been studied intensively in literature but its underlying microscopic mechanisms are still debated and not fully understood until now [5, 8–10]. The most studied mechanisms of HE include hydrogen-enhanced decohesion (HEDE)[10, 11], hydrogen-enhanced local plasticity (HELP)[12], adsorption-induced dislocation emission(AIDE)[13], or hydrogen-enhanced strain-induced vacancy formation mechanism (HESIV)[14]. While HELP, HESIV and AIDE are damage mechanisms related to localized plastic deformation at the crack tip; the HEDE

model assumes that dissolved hydrogen reduces the cohesive strength of the lattice and interfaces. All these mechanisms are of different nature but they are not mutually exclusive and may occur simultaneously. The dominant damage mechanism depends on material chemistry, its microstructure and external conditions (H concentration, type of loading, strain rate, temperature, etc.) [5, 9].

Since recently, many studies have focused on the HEDE mechanism of HE and computer simulations have shown to be an effective tool to explore the hydrogen-induced cohesion reduction in the bulk[15, 16] and hydrogen segregation-induced decohesion at GBs[17–24]. Nevertheless, there is still a number of open questions requiring further investigation. An example is the combined effect of some of the key alloying elements used in commercial NBA, such as Mo, with H on HEDE in Ni and its alloys representing an important practical issue[25].

Another issue is related to the role of C in HE of Ni. In Refs. [26, 27], it has been shown that the diffusion of C interstitials along GBs in Ni is four orders of magnitude faster than its bulk diffusion and large amount of C can accumulate at GBs, presumably due to significant segregation from the interior of the grains[27]. Latest DFT-based theoretical studies show that C segregates to Ni GB and enhances the GB cohesion[28, 18]. However, the results on segregation of single impurity elements studied in most of the research works so far are insufficient to describe synergistic effects of co-segregation at the interface and this question requires further investigation. For example, it has been experimentally shown that the interaction between co-segregation atoms in Fe-Mn-C[29] and in Ni-base alloys[30, 31] can have a pronounced effect on properties of the material and on its susceptibility to HE.

Such synergistic effects between H and other alloying elements have been studied theoretically by using first-principles calculations in some systems but not in Ni, to the best of our knowledge. So far, the first principles studies on solute co-segregation with H have been focused on Fe[32, 33] where it has been shown that alloying elements, like Cr, can have a detrimental effect on the segregation of H itself and on its effect on the GB cohesion. In this work, we focus on first principles investigation of the fundamentals of segregation and co-segregation of H with C and Mo impurities in Ni and on its effect on the GB cohesive strength in relation to the HEDE mechanism of HE using the Rice-Thomson-Wang theory of interface embrittlement[34, 35]. Furthermore, we focus on methodological aspects of the DFT calculations and investigate the effects of H-Mo and H-C interactions both in the bulk and at the GB in detail.

6.2 Computational details

6.2.1 Semiempirical calculations

The semiempirical simulations have been based on the embedded atom method (EAM) potential calculations within the framework of the extensively parallelized Large-scale Atomic Molecular Massively Parallel Simulator (LAMMPS) environment [36]. To obtain the GB energies with different orientations, we have used LAMMPS [36] to calculate the effects of GB misorientation on the energy of its interface. The EAM potential for Ni has been taken from Ref. [37]. The computational cells have been set up using the EAM equilibrium lattice constant of 3.520 Å, which is in good agreement with DFT (see Section 7.2.3) and the low temperature experimental data [38]. The optimal GB configurations which present the minimum energy state are determined after minimizing and relaxing the GB system at 0 K. The energy minimization of the structure has been carried out using the conjugate gradient algorithm with the convergence criteria 10^{-15} eV and 10^{-15} eV/Å in the total energy and the inter-atomic forces calculations for GBs.

6.2.2 DFT calculations

Spin polarized density functional theory (DFT) calculations have been performed using the projector-augmented-wave (PAW) [39, 40] method as implemented in the Vienna *Ab initio* simulation package (VASP) [41, 42]. We have used the Perdew-Burke-Ernzerhof (PBE) form of generalized gradient approximation (GGA) to the exchange-correlation potential [43]. The plane-wave basis set cutoff energy has been set to 400 eV. The convergence criteria of self-consistent calculations have been set to 10^{-5} eV/cell for the total energy and to 9×10^{-3} eV/Å for the atomic forces. The integration over the Brillouin zone has been done using the $4 \times 4 \times 1$ Monkhorst-Pack k -mesh [44] for all slab geometries and using the $4 \times 4 \times 4$ k -mesh in the $3 \times 3 \times 3 \times$ [conventional *fcc* cell] supercell (SC) calculations. The lattice parameter has been fixed to the equilibrium value in all slab and SC calculations while only the ions have been allowed to relax.

6.3 Methodology

6.3.1 Solution energy

There are three possible positions for solute atoms in the fcc lattice: (i) the two interstitial sites, *i.e.*, an octahedral site (OS) and a tetrahedral site (TS), and (ii) a substitutional site. The solution

energy of an impurity atom in a SC containing M atoms can be calculated using the following expressions[45, 46]:

$$E_{\text{sol}}^i = E_{\text{bulk}}^X[M; 1] - E_{\text{bulk}}^{\text{Ni}}[M; 0] - E_{\text{ref}}^X \quad (6.1)$$

for the interstitial and

$$E_{\text{sol}}^s = E_{\text{bulk}}^X[M - 1; 1] - E_{\text{bulk}}^{\text{Ni}}[M; 0] + E_{\text{ref}}^{\text{Ni}} - E_{\text{ref}}^X \quad (6.2)$$

for the substitutional impurities, where $E_{\text{bulk}}^X[M; 1]$ and $E_{\text{bulk}}^X[M - 1; 1]$ are the total energies of supercells containing one solute atom at one of the interstitial sites and at the substitutional site respectively.

$E_{\text{bulk}}^{\text{Ni}}[M; 0]$ is the total energy of a SC without impurity. $E_{\text{ref}}^{\text{Ni}}$ and E_{ref}^X are the reference state total energies of a Ni atom and of a solute X respectively.

6.3.2 Pair interactions in the bulk

The pair H-solute (X) interaction energies $V_n^{(2)}$ as a function of the coordination shell number n in the bulk of Ni are defined for the case of an interstitial solute as:

$$V_n^{(2)} = E_{\text{bulk}}^{\text{H-X}}[M; 2] + E_{\text{bulk}}^{\text{Ni}}[M; 0] - E_{\text{bulk}}^X[M; 1] - E_{\text{bulk}}^{\text{H}}[M; 1], \quad (6.3)$$

where $E_{\text{bulk}}^{\text{H-X}}[M; 2]$ is the total energy of the bulk Ni SC containing one interstitial H and one interstitial solute atom located as n th nearest neighbors and $E_{\text{bulk}}^{\text{H}}[M; 1]$ is the energy of a supercell containing one interstitial H atom. In the case when X is a substitutional, Equation (6.3) transforms to

$$V_n^{(2)} = E_{\text{bulk}}^{\text{H-X}}[M - 1; 2] + E_{\text{bulk}}^{\text{Ni}}[M; 0] - E_{\text{bulk}}^X[M - 1; 1] - E_{\text{bulk}}^{\text{H}}[M; 1], \quad (6.4)$$

where $E_{\text{bulk}}^{\text{H-X}}[M - 1; 2]$ is the total energy of the bulk Ni SC containing one H atom and one substitutional solute atom located as n th nearest neighbors. The interaction $V_n^{(2)}$ are negative if two solutes tend to attract each other, and positive if two solutes tend to repel each other.

6.3.3 Interface formation energy

We define the free surface (FS) formation energy using the following expression:

$$\gamma_{\text{fs}}^0 = (E_{\text{slab}}^{\text{fs}} - N_{\text{slab}}^{\text{fs}} \epsilon_{\text{slab}}^0) / 2A, \quad (6.5)$$

where $E_{\text{slab}}^{\text{fs}}$ is the total energy of a slab containing two FSs, $N_{\text{slab}}^{\text{fs}}$ is the number of atoms in the FS slab, A is its cross-sectional area and ϵ_{slab}^0 is the energy of the space filling slab representing the bulk of the material calculated in the geometry of the FS slab[47]. The factor 2 in the denominator reflects the fact that there are two FSs per slab by construction (see Fig. 6.2). In the case when the slab geometries are the same for the FS and GB formation energy calculations, the GB formation energy can be defined as[47]:

$$\gamma_{\text{gb}}^0 = (E_{\text{slab}}^{\text{gb}} - N_{\text{slab}}^{\text{gb}} \epsilon_{\text{slab}}^0) / A - 2\gamma_{\text{fs}}^0, \quad (6.6)$$

where $E_{\text{slab}}^{\text{gb}}$ is the total energy of the slab containing one GB and two FSs (see Fig. 6.2) and $N_{\text{slab}}^{\text{gb}}$ is the number of atoms in the GB slab.

6.3.4 Segregation energy

GB or FS impurity segregation energies defined as the change in the total energy corresponding to impurity being taken out from the bulk region of the system and distributed over the FS or GB layers, there are four representative cases when n (number of solute in a GB layer) solute atoms segregate from bulk to an interface:

i) solutes occupy the interstitial sites in the bulk and at the interface:

$$\begin{aligned} E_{\text{seg}}^{\text{gb}} &= E_{\text{slab}}^{\text{gb}}[N; n] - E_{\text{slab}}^{\text{gb}}[N; 0] + n\Delta_{\text{bulk}}^{\text{X}}, \\ E_{\text{seg}}^{\text{fs}} &= (E_{\text{slab}}^{\text{fs}}[N; 2n] - E_{\text{slab}}^{\text{fs}}[N; 0]) / 2 + n\Delta_{\text{bulk}}^{\text{X}}; \end{aligned} \quad (6.7)$$

ii) solutes occupy the substitutional sites in the bulk and at the interface:

$$\begin{aligned} E_{\text{seg}}^{\text{gb}} &= E_{\text{slab}}^{\text{gb}}[N - n; n] - E_{\text{slab}}^{\text{gb}}[N; 0] + n\Delta_{\text{bulk}}^{\text{Ni} \rightarrow \text{X}}, \\ E_{\text{seg}}^{\text{fs}} &= (E_{\text{slab}}^{\text{fs}}[N - 2n; 2n] - E_{\text{slab}}^{\text{fs}}[N; 0]) / 2 + n\Delta_{\text{bulk}}^{\text{Ni} \rightarrow \text{X}}; \end{aligned} \quad (6.8)$$

iii) a solute occupies an interstitial site in the bulk and a substitutional at the interface:

$$\begin{aligned} E_{\text{seg}}^{\text{gb}} &= E_{\text{slab}}^{\text{gb}}[N - n; n] - E_{\text{slab}}^{\text{gb}}[N; 0] + n(\Delta_{\text{bulk}}^{\text{X}} + \epsilon_0), \\ E_{\text{seg}}^{\text{fs}} &= (E_{\text{slab}}^{\text{fs}}[N - 2n; 2n] - E_{\text{slab}}^{\text{fs}}[N; 0]) / 2 + n(\Delta_{\text{bulk}}^{\text{X}} + \epsilon_0); \end{aligned} \quad (6.9)$$

iv) a solute occupies a substitutional site in the bulk and an interstitial at the interface:

$$\begin{aligned} E_{\text{seg}}^{\text{gb}} &= E_{\text{slab}}^{\text{gb}}[N; n] - E_{\text{slab}}^{\text{gb}}[N; 0] + n(\Delta_{\text{bulk}}^{\text{Ni} \rightarrow \text{X}} - \epsilon_0), \\ E_{\text{seg}}^{\text{fs}} &= (E_{\text{slab}}^{\text{fs}}[N; 2n] - E_{\text{slab}}^{\text{fs}}[N; 0]) / 2 + n(\Delta_{\text{bulk}}^{\text{Ni} \rightarrow \text{X}} - \epsilon_0). \end{aligned} \quad (6.10)$$

Here $E_{\text{slab}}^{\text{gb}}[N-n;n]$ and $E_{\text{slab}}^{\text{gb}}[N;n]$ are the total energies of the GB slab with n solutes at the substitutional sites and at the interstitial sites respectively; $E_{\text{slab}}^{\text{fs}}[N-2n;2n]$ and $E_{\text{slab}}^{\text{fs}}[N;2n]$ are the total energies of the FS slab containing N host atoms and $2n$ solutes (symmetrically distributed on both FSs of the slab, see Fig. 6.2) at the substitutional sites and at the interstitial sites respectively; $\Delta_{\text{bulk}}^{\text{Ni}\rightarrow\text{X}} = E_{\text{bulk}}^{\text{Ni}}[M;0] - E_{\text{bulk}}^{\text{X}}[M-1;1]$ is the energy difference (per X atom) between bulk supercells before and after one of the host atoms is replaced by an impurity atom and $\Delta_{\text{bulk}}^{\text{X}} = E_{\text{bulk}}^{\text{Ni}}[M;0] - E_{\text{bulk}}^{\text{X}}[M;1]$ is the same energy difference (per X atom) but for the interstitial case with no host atom being replaced by a solute atom; $\epsilon_0 = E_{\text{bulk}}^{\text{Ni}}[M;0]/M$ is the energy of the fcc Ni per atom. In this paper, we adopt the following sign convention: segregation energy $E_{\text{seg}}^{\text{gb}}$ ($E_{\text{seg}}^{\text{fs}}$) is negative if a solute tends to segregate to an interface.

6.3.5 Co-segregation of H-solute to an interface

The equilibrium co-segregation energy of a solute X (X=Mo or C in this work) with H (interstitial) to an interface at its equilibrium segregated state can be defined as

i) In the case when X occupies a substitutional site at the interface:

$$\begin{aligned} E_{\text{coseg}}^{\text{gb}} &= E_{\text{slab}}^{\text{gb}}[N-1;2] - E_{\text{slab}}^{\text{gb}}[N;0] + \Delta_{\text{bulk}}^{\text{H}} + \Delta_{\text{bulk}}^{\text{Ni}\rightarrow\text{X}} \\ E_{\text{coseg}}^{\text{fs}} &= (E_{\text{slab}}^{\text{fs}}[N-2;4] - E_{\text{slab}}^{\text{fs}}[N;0])/2 + \Delta_{\text{bulk}}^{\text{H}} + \Delta_{\text{bulk}}^{\text{Ni}\rightarrow\text{X}}; \end{aligned} \quad (6.11)$$

ii) In the case when X occupies an interstitial site at the interface:

$$\begin{aligned} E_{\text{coseg}}^{\text{gb}} &= E_{\text{slab}}^{\text{gb}}[N;2] - E_{\text{slab}}^{\text{gb}}[N;0] + \Delta_{\text{bulk}}^{\text{H}} + \Delta_{\text{bulk}}^{\text{X}} \\ E_{\text{coseg}}^{\text{fs}} &= (E_{\text{slab}}^{\text{fs}}[N;4] - E_{\text{slab}}^{\text{fs}}[N;0])/2 + \Delta_{\text{bulk}}^{\text{H}} + \Delta_{\text{bulk}}^{\text{X}}; \end{aligned} \quad (6.12)$$

here $E_{\text{slab}}^{\text{gb}}[N-1;2]$ (X substitutional) and $E_{\text{slab}}^{\text{gb}}[N;2]$ (X interstitial) are the total energies of the GB slab with two solutes at the GB; $E_{\text{slab}}^{\text{fs}}[N-2;4]$ (X substitutional) and $E_{\text{slab}}^{\text{fs}}[N;4]$ (X interstitial) are the total energies of the FS slabs with two solutes on each FS. In the case of FS calculations, H and X solutes are always symmetrically distributed on both surfaces of the FS slab (see Fig. 6.2).

6.3.6 GB strengthening energy

The ideal work of separation is a fundamental thermodynamic quantity that controls the mechanical strength of an interface. It is defined as the reversible work of decohesion, except that any diffusion exchange between the interface and the underlying bulk is suppressed during the decohesion (the fast separation limit)[34, 35]. In this case, the ‘‘local’’ equilibrium is maintained

between impurity atoms and the surface layer of the host. This equilibrium corresponds to the impurity chemical potential μ' different from the one in the bulk μ , and the expression for work of separation W_{sep} can be written as[48]

$$W_{sep} = 2\gamma_0^{fs} - \gamma_0^{gb} + (\mu' - \mu)\Gamma_{gb}, \quad (6.13)$$

where the first two terms on the right side of equation $2\gamma_0^{fs} - \gamma_0^{gb}$ correspond to the work of separation of the pure GB, *i.e.*, $W_{sep}^0 = 2\gamma_0^{fs} - \gamma_0^{gb}$, while Γ_{gb} is the number of solute atoms per unit interface area and it is assumed that the impurity distributes evenly between two newly created surfaces. If we neglect all temperature effects and calculate the change of the Gibbs free energy at 0K, Equation 6.13 becomes:

$$W_{sep} = W_{sep}^0 + (E_{seg}^{fs} - E_{seg}^{gb})\Gamma_{gb}. \quad (6.14)$$

In what follows, we evaluate the change of the work of separation in terms of the GB strengthening energy η as introduced in Ref. [47]:

$$\eta = (W_{sep}^0 - W_{sep})/\Gamma_{gb}. \quad (6.15)$$

The parameter η characterizes the cohesive strength of the GB with a segregated solute as compared to the GB without the solute. According to Equation 6.14, Equation 6.15 can be rewritten as:

$$\eta = E_{seg}^{gb} - E_{seg}^{fs}. \quad (6.16)$$

In this paper, we adopt the following sign convention: the strengthening energy parameter η is negative if the solute enhances the GB cohesion.

6.3.7 Representative GB and FS construction

The coincidence site lattice (CSL) GB model[49] has been used to model the GB structure at the atomic level. Selection of a representative CSL GB in Ni has been done using EAM calculations. The EAM calculations of CSL GB energies in metals provide very reasonable agreement with the DFT results for pure metals[50, 51] and can be very effectively used to scan the energy landscape of various GB configurations with no system size limitations characteristic to standard DFT calculations. The results of our EAM calculations are shown in Fig. 6.1 where the GB energy is calculated as a function of the misorientation angle in the

$\langle 100 \rangle$ direction. The plot is mirrored by a line of symmetry corresponding to the boundary plane on the *fcc* lattice, which is 90° in $\langle 100 \rangle$ tilt GB. The rotation angles of 0° , 90° and 180° (equivalent by symmetry) in the figure correspond to the perfect lattice configuration with no GB and the zero formation energy. The $\Sigma 5(012)$ GB represents a reasonable choice for a representative interface for DFT calculations as it falls in the midrange of special GBs formation energies in Ni, it can be constructed using relatively small size (see below) and is well-studied in literature[17, 52, 19, 18, 47, 53, 54].

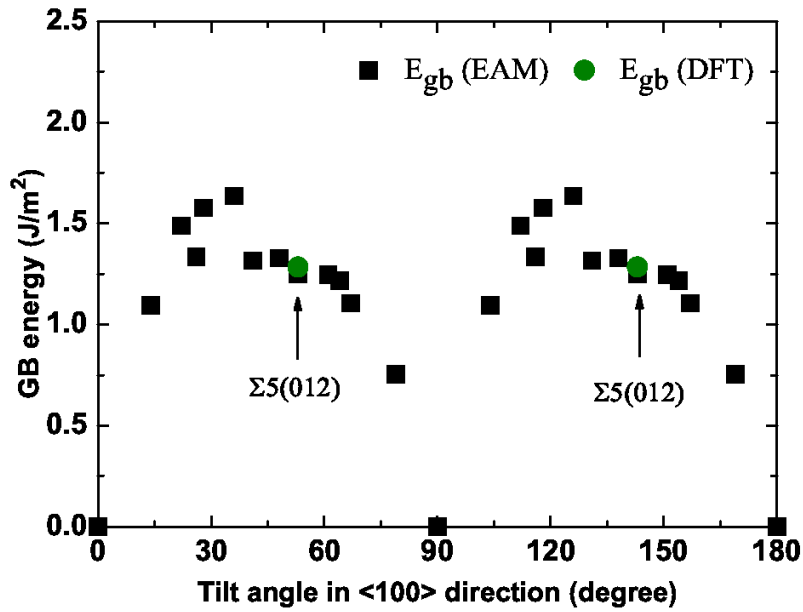


Fig. 6.1 The GB energy of various tilt CSL GBs with [100] rotation axis shown as a function of the tilt misorientation angle in Ni.

The structure of the selected representative $\Sigma 5(012)$ GB used in our DFT calculations is shown in Fig. 6.2. It has been constructed by rotating two *fcc* grains around the [100] axis by 53.1° , and it is represented by a supercell containing 76 nonequivalent atoms (19 atomic layers and 4 Ni atoms per layer) with two equivalent, reversely oriented grains. The slabs separated with more than 7.0 \AA of vacuum have been shown to be sufficient to suppress interactions between periodic images[55, 47].

The corresponding (012) FS has been modeled using the same slab geometry as for the $\Sigma 5(012)$ GB with the same number of atoms (76) and the size of the vacuum layer of 9.5 \AA . The FS structure is shown in Fig. 6.2. The size of the slab as well as of the vacuum layer have been converged with respect to the γ_{gb}^0 , γ_{fs}^0 of Ni and E_{seg}^{gb} and E_{seg}^{fs} for a representative impurity [55, 47].

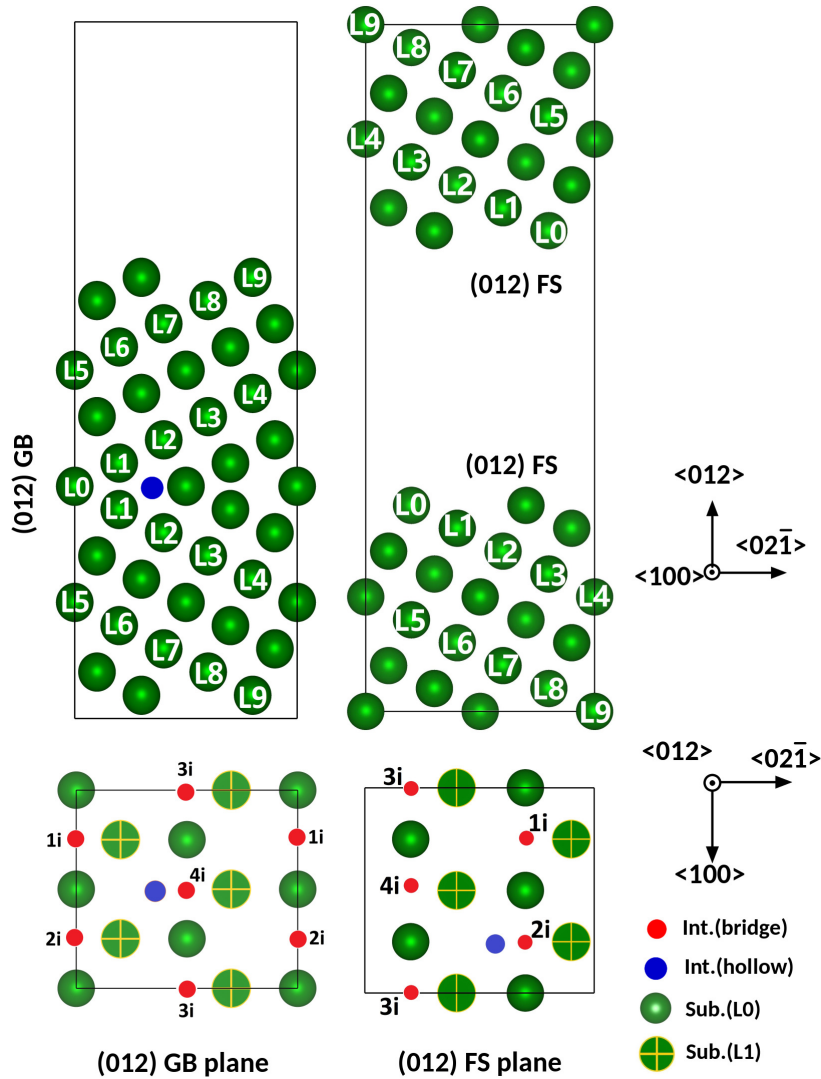


Fig. 6.2 Geometry of $\Sigma 5(012)[100]$ symmetric tilt GB and (012) FS (front and top views). "L" with a number numerate the GB and FS layers respectively. Interstitial "bridge" and "hollow" sites are shown with red and blue circles respectively.

6.4 Results and discussion

6.4.1 Choice of the exchange-correlation functional

In Table 6.1, we present the 0 K equilibrium lattice parameter, the bulk modulus, the bulk magnetic moment, the $\Sigma 5(012)$ GB and (012) FS formation energies of pure nickel calculated using different exchange correlation (XC) functionals. The LDA and three types of GGA (PBE [43], PBEsol [56] and PW91 [57]) functional available in VASP are chosen for comparison.

Table 6.1 Calculated values of the equilibrium lattice constant , the bulk modulus, the spin magnetic moment, the $\Sigma 5(012)[100]$ GB and the (012) FS formation energies in Ni. The calculated data are compared to experimental and DFT results from literature.

| | This work | | | | Literature results | | | | |
|-----------------|-----------|-------|--------|-------|---------------------------------------|--------------------|--------------------|--------------------|---------------------------------------|
| | LDA | GGA | | | DFT | | | | Expt. |
| | | PBE | PBEsol | PW91 | | | | | |
| a_{eq} | 3.456 | 3.515 | 3.460 | 3.518 | 3.423 ^a | 3.515 ^b | 3.518 ^c | 3.463 ^d | 3.515 ^e |
| B | 252 | 195 | 225 | 195 | 192 ^f | | | | 188 ^g |
| M | 0.61 | 0.64 | 0.61 | 0.61 | 0.63 ^h , 0.62 ⁱ | | | | 0.64 ^j |
| γ_{gb}^0 | 1.487 | 1.286 | 1.394 | 1.173 | 1.42 ⁱ | 1.30 ^k | 1.21 ^l | 1.23 ^m | 0.93 ^o |
| γ_{fs}^0 | 2.994 | 2.397 | 2.712 | 2.236 | 2.67 ⁱ | 2.45 ^k | 2.39 ^l | 2.53 ^m | 2.37 ⁿ , 2.49 ^o |

^a Reference[58], PAW-LDA .

^b Reference[59], PAW-GGAPBE.

^c Reference[58], PAW-GGAPBE.

^d Reference[58], PAW-GGAPBEsol.

^e Reference[38], x-ray diffraction, 87 K.

^f Reference[60], PAW-GGA.

^g Reference[61], Experiment.

^h Reference[62], Linear muffin-tin orbital method(LMTO).

ⁱ Reference[19], Augmented plane wave(APW)-GGA, $\Sigma 5(012)$ GB.

^j Reference[63], x-ray diffraction.

^k Reference[55], PAW-GGA, $\Sigma 5(012)$ GB.

^l Reference[64], PAW-GGA, $\Sigma 5(012)$ GB.

^m Reference[65], Norm-conserving pseudopotentials (NCP), $\Sigma 5(012)$ GB.

ⁿ Reference[66], Expt. (Liquid-vapour surface tension data for 0 K, general GBs).

^o Reference[67], Expt. (Zero creep technique at 1370°C, general GB).

The results presented in Table 6.1 demonstrate good agreement with previously published theoretical and experimental data on Ni [19, 38, 55, 58–65, 67, 66]. LDA FS and GB formation energies and the bulk modulus calculations generally overestimate the experimental values [66, 67] and provide higher values than GGA functionals used in this work and published in literature [19, 55, 65]. The LDA lattice parameter calculations provide underestimated values of the lattice parameter with respect to both GGA calculations and experiments. All XC functionals provide very similar values of the magnetic moment on Ni close to the experimental values [63] and the results of previous theoretical investigations [19, 62]. In general, the results obtained using the PBE XC functional agree best with the experimental data and therefore we choose this functional and the equilibrium lattice constant obtained using this functional for the remaining DFT calculations, unless specified otherwise.

6.4.2 Solubility of H, C and Mo in bulk Ni

Location of H, C and Mo impurities in the fcc lattice of Ni has been determined by means of calculating the solution energy at OS and TS interstitial sites as well as at a substitutional site as described in Section 6.3.1. The results shown in Table 9.3 suggest that H and C prefer interstitial OS sites whereas Mo occupies the substitutional fcc lattice site. The impurity solution energies along with the vacancy formation energy in pure Ni have been compared to earlier DFT-based calculations [16, 20–24, 68–71] and experiments [72].

The calculated solution energy of H at the OS site is 0.09 eV, which is close to the values obtained in other computational studies [16, 20–24]. The solution energy of H at the TS site is 0.36 eV. This value also agrees well with the results of previous computational studies [16, 20–24, 68] and experimental measurements [72]. The solution energy of C at both TS (2.47 eV) and OS (0.76 eV) sites agrees well with previous studies [69, 70]. Both values are much lower than that of the substitutional site equal to 3.73 eV. In the case of Mo, the solution energy at the substitutional site (0.04 eV) is much smaller than those at TS (6.34 eV) and OS (5.23 eV) sites which agrees well with other theoretical investigations [16, 71].

The site preference of H, C and Mo can be understood from simple geometric considerations. The space associated with the interstitial sites in Ni in our calculations can be described by an inscribed sphere of a radius r_{site} of 0.56 Å for the OS and of 0.30 Å for the TS. H, C and Mo have Slater radii r_{imp} of 0.25, 0.70 and 1.45 Å correspondingly [73]. From this perspective, only H can fit both TS and OS sites, C is slightly larger than the OS and Mo is too large for both of OS and TS. These arguments are also reflected in energy differences between TS, OS and the substitutional sites for all these elements, where the solution energies exceed 0.50 eV for all cases when $r_{\text{site}} < r_{\text{imp}}$ and are smaller if $r_{\text{site}} > r_{\text{imp}}$ (see Table 9.3).

6.4.3 Solute segregation to GB and FS

The information on the type of bulk configuration for each of the solute atom obtained in Section 6.4.2 has been used to calculate solute segregation energies of these solutes to the GB and FS planes (planes corresponding to "L0" sites and the top panel in Fig. 6.2) as described in Section 6.3.4. All sites for solute segregation considered in this work are shown in Fig. 6.2 with numbers for substitutional (Sub.) sites and with red and blue circles for two types of the interstitial sites in the GB and FS planes: i) the bridge (Int. bridge) site, which is located at the middle position of any two Ni atoms in the $\langle 100 \rangle$ direction of GB plane; ii) the hollow (Int. hollow), which is located at the GB core, see Fig. 6.2 or Ref. [17, 18] for details.

In Table 6.3, we first present the results corresponding to L0 GB and FS segregation of interstitial (both in the bulk and in the interface planes, Equation 6.7) C and H solutes and

Table 6.2 Solution energies of H, C, Mo solutes as well as of a vacancy in Ni (in eV). OS, TS, Sub. and Vac. abbreviations denote octahedral site, tetrahedral site, substitutional site and a vacancy respectively.

| Defect | OS | TS | Sub. | Method | Reference |
|--------|------|------|-------|------------|-----------|
| H | 0.09 | 0.36 | 2.08 | PAW-GGA | This work |
| | 0.11 | – | – | PWSCF-PBE | [24] |
| | 0.09 | 0.31 | 2.06 | PAW-GGA | [23] |
| | 0.08 | 0.33 | – | VASP | [20] |
| | 0.06 | 0.29 | 2.11 | PAW-GGA | [16] |
| | 0.05 | 0.29 | – | PAW-GGA | [21] |
| | 0.08 | – | – | PAW-GGA | [22] |
| | 0.06 | – | – | PAW-GGA | [68] |
| | 0.13 | – | – | experiment | [72] |
| C | 0.76 | 2.47 | 3.73 | PAW-GGA | This work |
| | 0.64 | 2.25 | – | PAW-GGA | [69] |
| | 0.70 | – | – | PAW-GGA | [70] |
| Mo | 5.23 | 6.34 | 0.04 | PAW-GGA | This work |
| | 4.10 | 5.00 | –0.03 | PAW-GGA | [16] |
| | – | – | 0.14 | PAW-GGA | [71] |
| Vac. | – | – | 1.42 | PAW-PBE | This work |
| | – | – | 1.48 | PWSCF-PBE | [24] |
| | – | – | 1.38 | PAW-GGA | [23] |
| | – | – | 1.38 | PAW-GGA | [21] |

of a substitutional (both in the bulk and in the interface planes, Equation 6.8) Mo solute as it has been considered in the most of the theoretical works cited in the table [17–19, 28, 47, 52–54, 74–77] and such positions correspond to the lowest energy configurations according to Equations 6.7–6.10. Our results suggest that both H and C can segregate to GB as well as to FS. H has a stronger tendency to segregate to FS while C has a stronger tendency to segregate to the GB. In the case of Mo, it prefers to segregate to GB and has no segregation tendency toward FS. These differences in GB and FS segregations are also related to their embrittling potency or the strengthening energy (see Section 6.3.6). In this way, H has an embrittling while C and Mo have a strengthening effect on the GB cohesive strength within the Rice-Thomson-Wang theory of GB embrittlement.

Other theoretical investigations on segregation and embrittling effect of H, C and Mo impurities segregation to the GB plane support our findings [17–19, 47, 52–54, 74–77]. However, the information on GB and FS segregation in most of these investigations is limited to GB and FS layers or only assumes always the same type of either interstitial or substitutional site occupied by an impurity atom in both bulk and GB which must not necessarily be the case.

Table 6.3 GB, FS, and strengthening energies of H, C and Mo in Ni (in eV/atom). The GB orientation, computational methods, used lattice parameters, and references are shown in separate columns. All results correspond to 0.25 ML solute interface excess.

| Solutes | GB/FS | $E_{\text{seg}}^{\text{gb}}$ | $E_{\text{seg}}^{\text{fs}}$ | η | Method | a_0 | Reference |
|---------|-----------------------|------------------------------|------------------------------|--------|----------------|-------|-----------|
| H | $\Sigma 5(012)$ | -0.27 | -0.60 | 0.33 | VASP-PAW-GGA | 3.515 | This work |
| | $\Sigma 5(012)$ | -0.31 | -0.71 | 0.40 | WIEN2k-PAW-GGA | 3.503 | [19, 18] |
| | $\Sigma 5(012)$ | — | — | 0.27 | FLAPW-GGA | 3.514 | [17] |
| | $\Sigma 5(012)$ | -0.23 | — | — | VASP-PAW-GGA | 3.514 | [53] |
| | $\Sigma 5(001)$ | -0.16 | -0.58 | 0.42 | VASP | — | [74] |
| | $\Sigma 3(112)$ | -0.24 | — | — | EAM | 3.520 | [75] |
| | $\Sigma 9(221)$ | -0.28 | — | — | EAM | 3.520 | [75] |
| | $\Sigma 11(113)$ | -0.24 | — | — | EAM | 3.520 | [75] |
| | $\Sigma 5(012)$ | — | — | 0.27 | EAM | 3.520 | [52] |
| | $\Sigma 5(012)$ | -0.25 | -0.55 | 0.30 | EAM | 3.520 | [54] |
| C | $\Sigma 5(012)$ | -0.83 | -0.53 | -0.30 | VASP-PAW-GGA | 3.515 | This work |
| | $\Sigma 5(012)$ | -0.83 | -0.61 | -0.22 | WIEN2K-GGA | 3.503 | [18] |
| | $\Sigma 3(11\bar{2})$ | -0.39 | — | — | VASP-PAW-GGA | 3.525 | [28] |
| Mo | $\Sigma 5(012)$ | -0.29 | 0.68 | -0.97 | VASP-PAW-GGA | 3.515 | This work |
| | $\Sigma 5(012)$ | — | — | -0.70 | FLAPW-GGA | — | [76] |
| | $\Sigma 5(012)$ | -0.57 | 0.34 | -0.91 | VASP-PAW-GGA | 3.447 | [47, 77] |

Therefore, the extended study of the segregation behavior of H, C and Mo solutes is needed. Fig. 6.3 shows complete segregation profiles for H, C and Mo impurities as a function of distance from GB and FS. Here one can see that H and C prefer to occupy interstitial sites at the L0 layer of the GB side, while Mo has a slight preference for segregation towards the third layer from the GB plane (L2 in Fig. 6.2) layer. Our results show that outside of the GB plane, the stable interstitial sites for our considered solutes always correspond to the octahedral interstitial site of the bulk fcc lattice. H and C have been found to occupy the *bridge* interstitial sites and Mo the substitutional site (See Fig. 6.2 and 6.3). The segregation tendencies near the FS are even more diverse: the lowest FS segregation energy for H, C and Mo atoms corresponds to the first, the second and the fourth layer from the FS plane layers (L9, L8 and the L6 in the notations of GB slab in Fig. 6.2), respectively.

In Table 6.3, we show the results obtained using the lowest GB segregation energies and the FS segregation energies that exactly correspond to the initial GB positions of solute atoms before the cleavage. These results are later used for calculation of the change of the work of separation introduced by each of the impurities η . This approach corresponds to the fast separation limit of the Rice-Thomson-Wang theory of interface embrittlement[34, 35]. All sites for impurity segregation considered in this work are shown in the bottom panel of Fig. 6.2 where all considered substitutional sites (Sub.) are numbered and interstitial sites are marked

with smaller blue or red circles. Only the results for the minimum segregation energy are shown in Table 6.3. However, one also can consider other potential segregation sites in GB layer which beyond lowest GB segregation energies. Our calculations show that both H and C occupy the *bridge* site and Mo takes the substitutional site in the GB plane. For H, it stays at the interstitial bridge site at GB/FS after relaxation from either a initial bridge or hollow site. In the case of C, the segregation energy of the *hollow*-site C is -0.36 eV, which is higher than the segregation energy of the *bridge*-site C ($E_{seg}^{gb} = -0.83$ eV). A *hollow*-site C on FS can not be stable and will segregate to the *bridge* site at L1 subsurface layer (see Fig. 6.2 and the segregation profile in Fig. 6.3). For Mo, the GB and FS segregation energies to the hollow site is 0.81 eV and 0.91 eV, respectively, which means Mo does not segregate to interstitial site at both GB and FS. All considered interstitial impurities also prefer *bridge* the interstitial sites and the substitutional impurity prefers the substitutional site if placed outside of the GB plane.

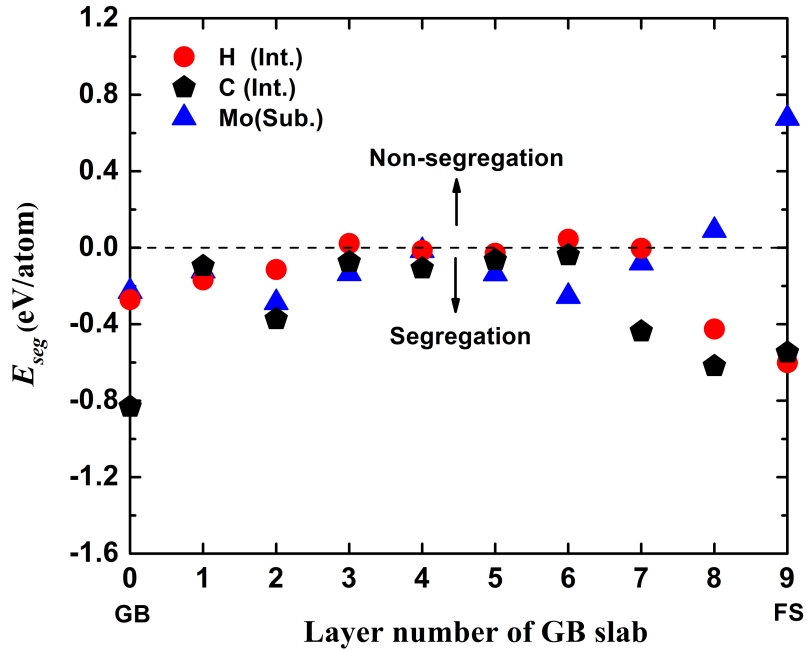


Fig. 6.3 H (interstitial), C (interstitial) and Mo (substitutional) solute atom segregation profiles within the half section of the GB slab containing a $\Sigma 5$ (012)GB and a (012) FS (see Fig. 6.2).

6.4.4 Effects of volume and impurity excess changes

In the previous sections, all reported results correspond to 0 K equilibrium lattice constant calculations and to 0.25 ML of impurity excess at an interface. In this section, we will demonstrate possible effects of volume change and impurity excess variations on the interface formation and on GB/FS solute segregation energies in Ni.

6.4.4.1 Volume change effect on interface formation and cohesion

As it has already been shown in literature, the volume change can have a sizable effect on the formation energy of low index interfaces in metals[78]. In Fig. 6.4, we show the results of the volume change effect on γ_{fs}^0 , γ_{gb}^0 and W_{sep}^0 (compressive for $a < 3.515$ Å and expansion for $a > 3.515$ Å).

The calculated γ_{fs}^0 energies exhibit a pronounced dependency on the volume change if the bulk lattice constant is > 3.54 Å and almost no dependence upon compression up to 3.495 Å. At the same time, the observed energy changes do not exceed 10% (γ_{fs}^0 decreases) within the chosen interval of the corresponding lattice constant of Ni (limited above by 3.620 Å [79]). The overall changes of γ_{gb}^0 and of W_{sep}^0 within the selected interval, in particular, near the 0 K equilibrium value of the lattice constant a_0 , are negligibly small.

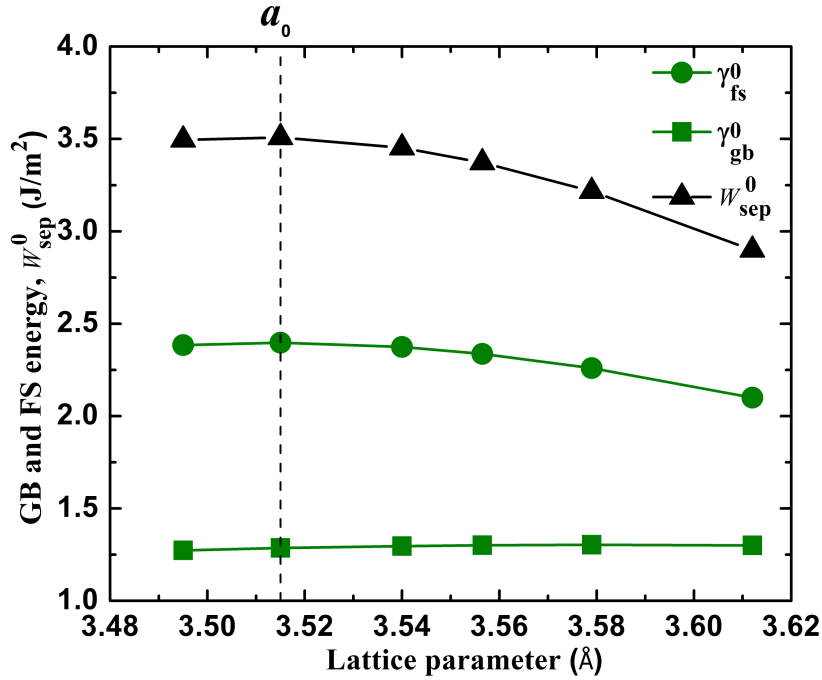


Fig. 6.4 (012) GB and FS energies and the work of separation as a function of the lattice parameter of Ni. The vertical dashed line shows the equilibrium lattice parameter at 0 K.

6.4.4.2 Volume change effect on solute segregation

A similar to the previous section study has been done by us in connection to the solute segregation energies. Unlike γ_{gb}^0 and γ_{fs}^0 , E_{seg}^{gb} and E_{seg}^{fs} exhibit a much more pronounced dependence on volume changes (see Fig. 6.5). The dependence is almost linear and very similar

for both FS and GB for all impurity atoms. The strongest dependence is observed in the case of C solute followed by Mo and H.

For both C and H atoms, $E_{seg}^{gb} < 0$ and $E_{seg}^{fs} < 0$ in the whole interval of considered volumes suggesting a propensity toward GB and FS segregation. In the case of Mo atoms, the situation is slightly different: if the lattice parameters $< 3.58 \text{ \AA}$, Mo atoms tend to segregate to the GB. However, E_{seg}^{gb} changes sign (becomes positive) if the lattice constant increases above 3.58 \AA suggesting the anti-segregation behavior. In order to connect this observation to the solute atom segregation behavior at elevated temperatures corresponding to the respective volume expansion regime, a more detailed investigation is required. This topic goes beyond the scope of the present paper but it would be an interesting subject for future investigations. The E_{seg}^{fs} of Mo is positive in the whole interval of considered volumes suggesting no segregation to (012) FS in Ni.

Using Equation 6.7 and 6.8, we have calculated FS segregation energies for H, C, and Mo at different lattice parameter to obtain strengthening energies by Equation 6.16. In contrast to E_{seg}^{gb} and E_{seg}^{fs} , η for all elements does not exhibit almost any dependence on lattice strains and stays virtually constant to 0.33 eV , -0.30 eV and -0.91 eV for H, C and Mo solutes respectively.

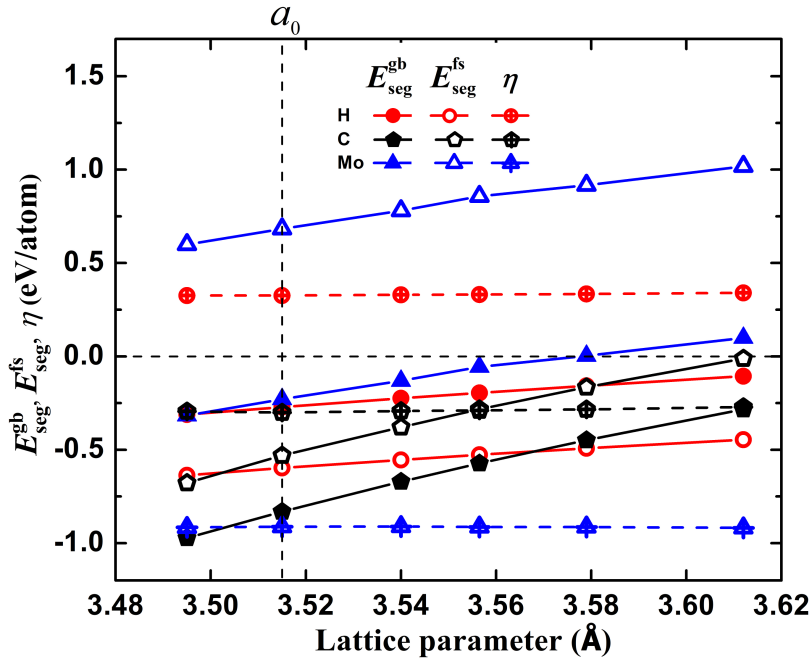


Fig. 6.5 GB, FS segregation energy and strengthening energy of H, C and Mo as a function of lattice parameter. The vertical dash line shows the equilibrium lattice parameter of Ni at 0 K.

6.4.4.3 Effect of solute excess on the segregation

As shown in bottom panel of Fig. 6.2, there are 4 substitutional sites and 8 potential interstitial sites (4 bridge sites and 4 hollow sites) in (012) GB layer. As we have shown in Section 6.4.3, Mo prefers the substitutional site while H and C prefer to occupy the bridge sites in the GB layer. Therefore, we have selected 4 substitutional and 4 corresponding interstitial (bridge) sites for Mo and H or C respectively. In what follows, we define these 4 sites for each type of the impurity atoms within the GB plane as a monolayer (ML) and vary the amount of Mo, C and H atoms from 1 to 4 within the GB plane and refer to these results to as 0.25, 0.5, 0.75, and 1 ML respectively.

In Fig. 6.6, we present our results on the segregation energy and strengthening energy as a function of H, C, and Mo coverage. $E_{\text{seg}}^{\text{gb}}$ and η change with increasing interface impurity content are much less pronounced for H than for C and Mo.

In the case of H and C, we observe a negligible decrease (0.01 eV) of both parameters from 0.25 ML to 0.50 ML solute excess and an increase from 0.50 ML to 1 ML, meaning that a pair of H or C atoms can be favored in the $\Sigma 5$ GB, which was also confirmed in Ref. [80] by calculating the H atom formation energy in Ni $\Sigma 5(012)$ GB. In the case of Mo, we observe a decrease of both segregation energy and strengthening energy. This behavior indicates repulsive solute interactions at the GB for C and H when solute excess is higher than 0.50 ML and attractive solute interaction for Mo, suggesting that Mo atoms can be prone to clustering at the GB in Ni. The changes in η with solute excess for H, C and Mo suggest that increasing H excess at the GB reduces W_{sep} (GB cohesion) linearly and remains the η as almost constant (see Equation 6.13-6.15). On the other side, increasing C content at the GB above 0.5 ML will significantly reduce its positive effect on the GB strength with η approaching zero at 1 ML. Mo, on contrary, enhances its positive influence on GB cohesion with increasing its content almost linearly which makes it the most efficient GB strengthener among the considered elements.

6.4.5 Interaction of H with Mo and C solutes in Ni

In order to understand possible synergetic effects between H and other solutes in Ni, we would like to get the first an idea on H-solute pair interactions in the bulk and at GB. In what follows, we take the first step in this direction and present results.

6.4.5.1 H-solute interactions in the bulk

Due to high solubility of H in Ni[81, 24], H might be present in the material at higher concentrations rather than in the dilute limit and its interaction with other alloying elements can play a role. Using Equations 6.3 and 6.4, we have calculated the pair H-H, H-Mo and H-C interactions

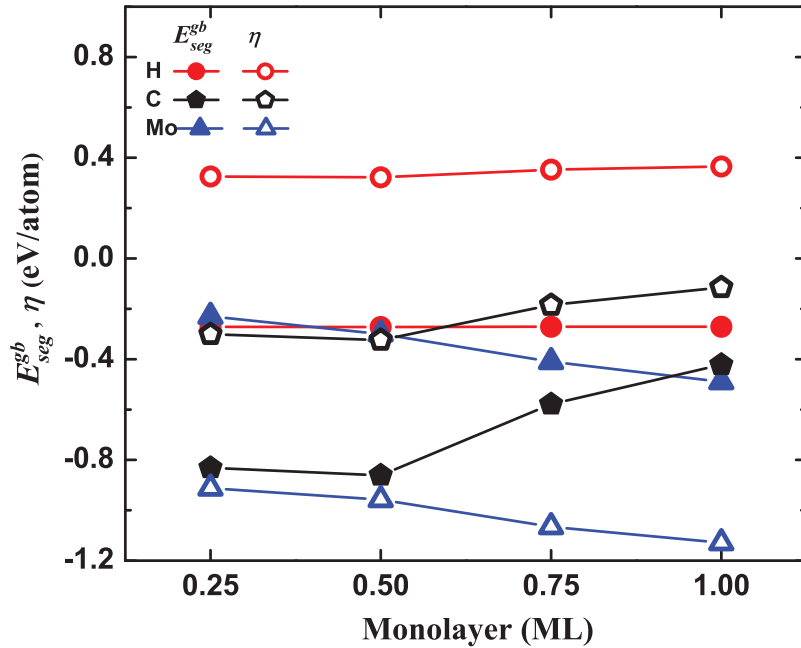


Fig. 6.6 H, C and Mo GB segregation and strengthening energies as a function of their GB excess (in ML).

as a function of interaction distance between these pairs of atoms in the fcc Ni matrix. The positions of the solutes in matrix have been selected according to the results presented in Table 9.3.

The H-H pair interactions have been checked at the 5 first coordination shells and have been found to be negligibly small (the strongest interaction energy at the first coordination shell has been found to be less than 0.02 eV). This result agrees with previous findings of Ref. [82]. The H-C interactions have been found to be negligibly small as well (below 0.02 eV) at the 5 first coordination shells. The strongest interaction has been found in the case of a Mo-H couple of atoms at the first coordination shell. This interaction of 0.121 eV is repulsive suggesting that Mo and H atoms are unlikely to be found as the first neighbors in Ni solid solution. The remaining interactions from the second to fifth coordination shells are below 0.02 eV as in the case of H-Mo.

6.4.5.2 Co-segregation of H-solute to the GB

The co-segregation of H-Mo and H-C solute atoms to the GB has been studied within the first three GB layers (L0, L1 and L2 in Fig. 6.2). The choice of the layers has been based on the results presented in Fig. 6.3 where all H, C and Mo atoms show the lowest segregation energies within the first three layers from the GB plane. There are 4 substitutional and 4 interstitial sites

in each layer (see bottom panel in Fig. 6.2) being occupied by solute atoms according to their site preferences calculated for the case of the single atom segregation in Section 6.4.3.

The co-segregation of Mo and C impurities with H at the $\Sigma 5(012)$ GB has been studied as described in Section 6.3.5 and Equation 6.16. The co-segregation of H–Mo and H–C results are presented in Fig. 6.7 and Fig. 6.8, respectively. Each figure shows the results for co-segregation energies (top panel), the corresponding effect of co-segregating atoms on the GB cohesion η (middle panel). The interatomic distance between co-segregating atoms after relaxation is shown in the bottom panel. The results correspond to configurations with the solute atoms located at substitutional (Mo) and interstitial (H, C) positions at the first three layers starting from the GB plane (see Fig. 6.2).

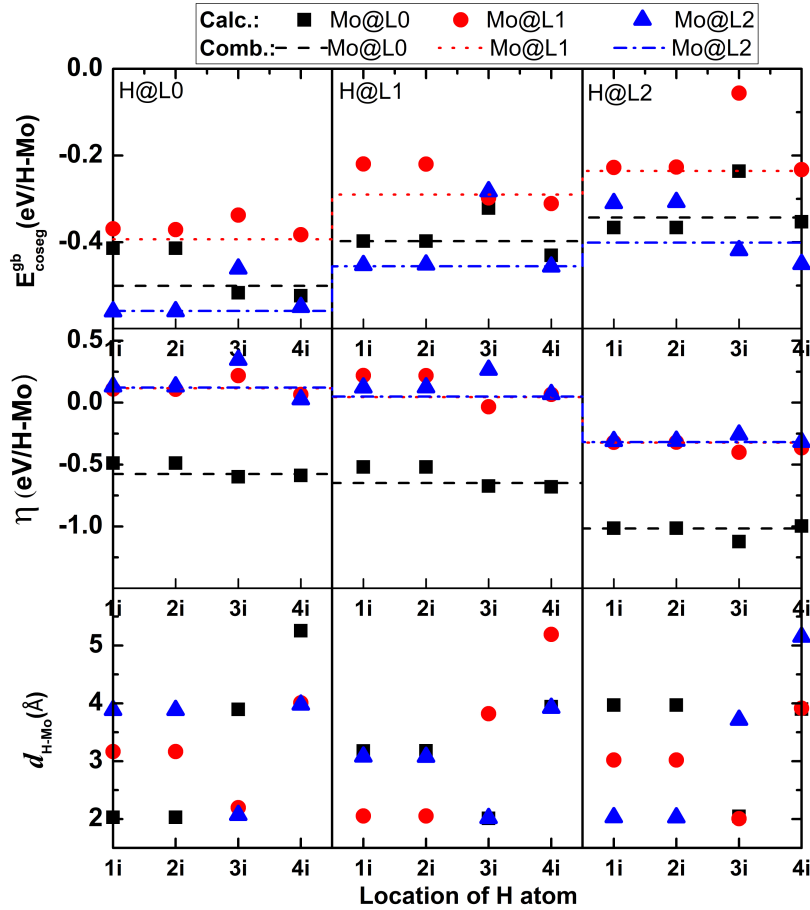


Fig. 6.7 The calculated H–Mo co-segregation energy, strengthening energy, and the interatomic distance between H and Mo atoms at the $\Sigma 5(012)$ GB are shown by individual symbols. The combined values for segregation and strengthening energies of each element to corresponding layer are shown by horizontal lines. H locations correspond to the interstitial *bridge* sites as enumerated in Fig. 6.2.

The co-segregation energies and strengthening energies of H-Mo along with the interatomic distances between H and Mo are shown in Fig. 6.7. Differently colored symbols (Calc.) correspond to Mo atoms located at different GB layers (L0, L1, L2, see Fig. 6.2), the figure blocks separated by vertical lines correspond to H atoms located at different GB layers. As it has been shown in Fig. 6.3, Mo has the lowest GB segregation energy at the substitutional site in L2 (-0.29 eV) and H in L0 (-0.27 eV). Co-segregation of H and Mo, does not change the site preference for H atoms though it makes 4 interstitial positions in the GB plane none-equivalent (compared to a single impurity segregation case) and combinations of H-Mo atoms located at the longest distance of about 3.8 Å from each other in L0 and L2 layers respectively have the lowest segregation energies.

Here we would like to note that all considered combinations of H-Mo solute atoms have a negative segregation energy indicating a pronounced propensity toward segregation of a combination of these two solutes. However, the effect of co-segregating atoms on the GB decohesion (parameter η) is not the same for all considered configurations of segregating atoms. For instance, all configurations with Mo solute atoms segregating to the GB layer L0 and H to any layer have a pronounced GB strengthening effect (negative η) but most of configurations with Mo segregating to L1 and L2 layers and H to L0-L2 layers have a slight GB embrittling effect (positive η). Though an overall effect of H-Mo co-segregation for most of the considered seems to be positive, a more detailed investigation of the GB segregation the framework of segregation isotherms[83] is required to provide a quantitative answer on the resulting effect of H-Mo co-segregation on the GB cohesion. Such investigation goes beyond the framework of the current paper and it is a subject of ongoing work and future publications.

In Fig. 6.8, we show a similar to Fig. 6.7 plot for the H-C co-segregation. In comparison to the single solute atom segregation profiles in Fig. 6.1 where both C and H solute atoms have the lowest segregation energy in the GB layer L0, the co-segregation of H and C solute atoms does not change the site preference for this couple of solute atoms: both prefer the GB layer L0 and have a pronounced segregation tendency toward the first three GB layers considered in this study (L0, L1 and L2). The configurations of H-C solute atoms separated by the largest possible distance within the slab are favored. The overall effect of H-C co-segregation on the GB cohesion is primarily negative with just a few combinations of H-C solute atoms providing the GB strengthening when C is located in the L0 (1i) and H in the L1 or L2 layers.

We have compared the directly calculated co-segregation energies to the results of a linear superposition of the individual H and solute atom segregation energies. In Figs. 6.7 and 6.8, we show these results of this linear superposition with horizontal lines (Comb.) for H-Mo and H-C located in the corresponding GB layers (L0-L2). As one can see, the results of the superposition are very close to those of the direct DFT calculations for almost all combinations

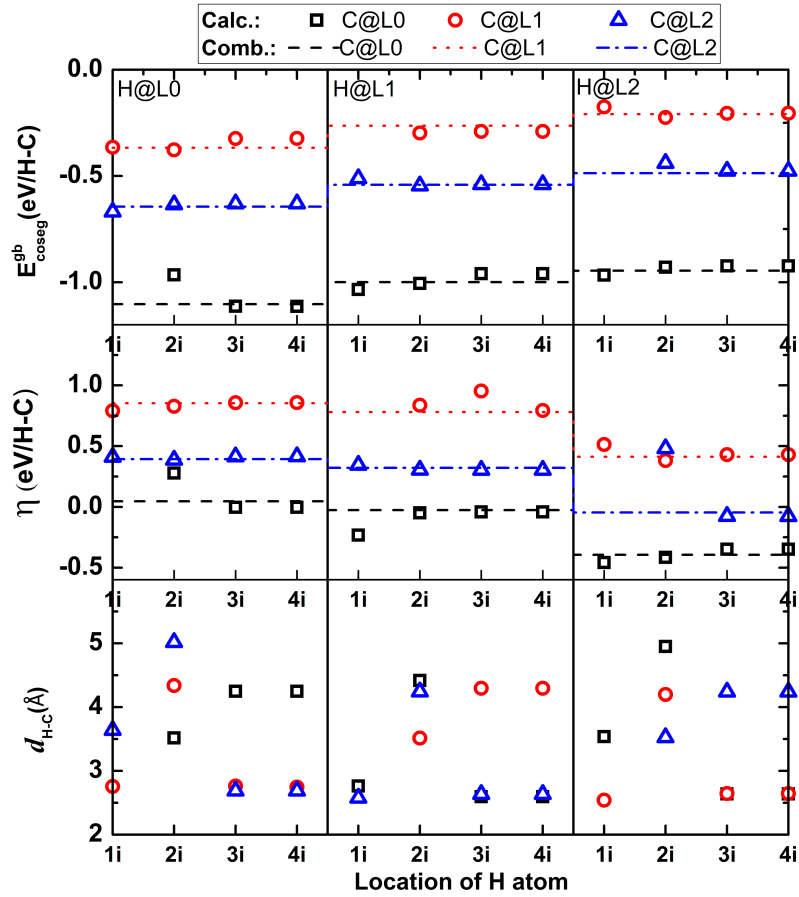


Fig. 6.8 The calculated H–C co-segregation energy, strengthening energy, and the interatomic distance between H and C atoms at the $\Sigma 5(012)$ GB are shown by individual symbols. The combined values for segregation and strengthening energies of each element to corresponding layer are shown by horizontal lines. H locations correspond to the interstitial "bridge" sites as enumerated in Fig. 6.2

of segregation solute atoms. The observed deviations for most of the pairs are found to be within 0.15 eV for H–Mo and within less than 0.02 eV for almost all H–C pairs with an exception of H (L0-2i)-C (L0-1i) combination. These results agree well with the H–solute interactions in the bulk (Section 6.4.5.1) and suggesting that the interactions in the bulk and in the GB are very similar though there are some exceptions indicating that the H–C interactions in the GB plane can be stronger than those in the bulk. However, the lowest $E_{\text{coseg}}^{\text{gb}}$ is virtually identical for both H–Mo and H–C couples calculated by both methods. The same result holds true for the calculations of the GB strengthening energy η , which has been calculated in the direct DFT calculations using the FS H-solute positions corresponding to the initial GB site occupancy by segregating atoms before cleavage. Following these results, we suggest that a

simple superposition of the segregation energies can be very effectively used to predict the segregation of H–Mo and H–C solutes at Σ 5 GB in Ni.

6.5 Conclusion

First-principles calculations based on density functional theory have been performed to investigate H, C and Mo solute segregation to Ni Σ 5(012) GB and Ni (012) FS as well as their effect on the GB cohesion. Results show that H, C, and Mo solutes segregate to the GB whereas only H and C exhibit a tendency toward FS segregation. C and Mo solutes demonstrate the GB strengthening and H the GB embrittling effects in Ni. We have observed a strong dependence of the GB and FS segregation energies of all solutes on system volume changes and almost no volume dependence of the GB strengthening energy. The results indicated that the GB segregation energy of Mo can change the sign at relatively large volumes. There is virtually no dependence of the GB segregation energy on the impurity excess in the case of H segregation, and a sizable increase of GB segregation energy with increasing C solute GB excess and decrease of GB segregation energy with increasing Mo solute GB excess.

The results on co-segregation of H-C and H-Mo solute atoms show a significant distribution of the GB segregation energy and strengthening energy at the GB within the first three GB layers. Both co-segregating couples exhibit a pronounced segregation tendency toward the first three layers from the GB plane and have different (both positive and negative) values of strengthening energy depending on the configurations of the segregation couples. This result indicates a possible mixed character of the effect of co-segregating solutes on the GB cohesion in Ni with a predominantly strengthening effect for the H–Mo solute couple and a possible destrengthening effect of the H–C solute couple for the majority of considered configurations.

The results of the comparison between the results of direct DFT calculations of H–solute co-segregation and of the superposition of individual segregation of solute atoms suggest that a linear superposition of the segregation energies (weak H-solute interaction at GB and in the bulk) can be very effectively used to predict the ground state GB segregation energy and the strengthening energy in Ni-C-H and Ni-Mo-H systems. We suggest that the same result may hold true for other Ni-H-X systems as well.

The aforementioned results on H-solute co-segregation provide a segregation-induced GB strengthening strategy for reducing property toward the intergranular fracture of Ni and its alloys caused by HEDE.

References

- [1] W. H. Johnson, *Proc. R. Soc.* 23 (1875) 168–179.
- [2] P. Cotterill, *Prog. Mater. Sci.* 9 (1961) 205 – 301.
- [3] M. Louthan, G. Caskey, J. Donovan, D. Rawl, *Mater. Sci. Eng.* 10 (1972) 357 – 368.
- [4] D. E. J. Talbot, *Int. Metall. Rev.* 20 (1975) 166–184.
- [5] M. Nagumo, *Fundamentals of hydrogen embrittlement*, Springer, 2016.
- [6] E. Sirois, H. Birnbaum, *Acta Mater.* 40 (1992) 1377 – 1385.
- [7] S. K. Lawrence, B. P. Somerday, R. A. Karnesky, *JOM* 69 (2017) 45–50.
- [8] S. M. Myers, M. I. Baskes, H. K. Birnbaum, J. W. Corbett, G. G. DeLeo, S. K. Estreicher, E. E. Haller, P. Jena, N. M. Johnson, R. Kirchheim, S. J. Pearton, M. J. Stavola, *Rev. Mod. Phys.* 64 (1992) 559–617.
- [9] A. Pundt, R. Kirchheim, *Ann. Rev. Mater. Res.* 36 (2006) 555–608.
- [10] I. M. Robertson, P. Sofronis, A. Nagao, M. L. Martin, S. Wang, D. W. Gross, K. E. Nygren, *Metall. Mater. Trans. A* 46 (2015) 2323–2341.
- [11] M. Dadfarnia, A. Nagao, S. Wang, M. L. Martin, B. P. Somerday, P. Sofronis, *Int. J. Fract.* 196 (2015) 223–243.
- [12] W. W. Gerberich, R. A. Oriani, M.-J. Lji, X. Chen, T. Foecke, *Philos. Mag. A* 63 (1991) 363–376.
- [13] S. Lynch, *Acta Metall.* 36 (1988) 2639 – 2661.
- [14] M. Nagumo, *Mater. Sci. Tech.* 20 (2004) 940–950.
- [15] M. S. Daw, M. I. Baskes, *Phys. Rev. Lett.* 50 (1983) 1285–1288.
- [16] D. Connétable, É. Andrieu, D. Monceau, *Comput. Mater. Sci.* 101 (2015) 77–87.
- [17] W. T. Geng, A. J. Freeman, R. Wu, C. B. Geller, J. E. Raynolds, *Phys. Rev. B* 60 (1999) 7149–7155.
- [18] M. Yamaguchi, M. Shiga, H. Kaburaki, *J. Phys.: Condens. Matter* 16 (2004) 3933.
- [19] M. Yamaguchi, M. Shiga, H. Kaburaki, *J. Phys. Soc. Jpn.* 73 (2004) 441–449.
- [20] E. Wimmer, W. Wolf, J. Sticht, P. Saxe, C. B. Geller, R. Najafabadi, G. A. Young, *Phys. Rev. B* 77 (2008) 134305.
- [21] R. Nazarov, T. Hickel, J. Neugebauer, *Phys. Rev. B* 89 (2014) 144108.
- [22] D. D. Stefano, M. Mrovec, C. Elsässer, *Acta Mater.* 98 (2015) 306 – 312.
- [23] D. Connétable, Y. Wang, D. Tanguy, *J. Alloys Compd.* 614 (2014) 211 – 220.
- [24] A. Metsue, A. Oudriss, X. Feaugas, *J. Alloys Compd.* 656 (2016) 555–567.
- [25] L. E. Shoemaker, *Superalloys 718, 625, 706 and Derivatives 2005* (2005) 409–418.
- [26] T. Parthasarathy, P. Shewmon, *Scr. Metall.* 17 (1983) 943 – 946.
- [27] L. V. Alvensleben, P. Haasen, *MRS Proceedings* 138 (1988) 479.

- [28] D. J. Siegel, J. Hamilton, *Acta Mater.* 53 (2005) 87 – 96.
- [29] A. T. Wicaksono, M. Militzer, *IOP Conf. Ser. Mater. Sci. Eng.* 219 (2017) 012044.
- [30] A. Kimura, H. Birnbaum, *Acta Metall.* 36 (1988) 757 – 766.
- [31] J. Dong, M. Zhang, X. Xie, R. Thompson, *Mater. Sci. Eng. A* 328 (2002) 8 – 13.
- [32] B. He, W. Xiao, W. Hao, Z. Tian, *J. Nucl. Mater.* 441 (2013) 301 – 305.
- [33] M. Yuasa, M. Hakamada, Y. Chino, M. Mabuchi, *ISIJ Int.* 55 (2015) 1131–1134.
- [34] J. R. Rice, R. Thomson, *Philos. Mag. A* 29 (1974) 73–97.
- [35] J. R. Rice, J.-S. Wang, *Mater. Sci. Eng. A* 107 (1989) 23 – 40.
- [36] S. Plimpton, *J. Comput. Phys.* 117 (1995) 1 – 19.
- [37] X. W. Zhou, R. A. Johnson, H. N. G. Wadley, *Phys. Rev. B* 69 (2004) 144113.
- [38] J. Bandyopadhyay, K. Gupta, *Cryogenics* 17 (1977) 345–347.
- [39] P. E. Blöchl, *Phys. Rev. B* 50 (1994) 17953.
- [40] G. Kresse, D. Joubert, *Phys. Rev. B* 59 (1999) 1758.
- [41] G. Kresse, J. Hafner, *Phys. Rev. B* 48 (1993) 13115–13118.
- [42] G. Kresse, J. Furthmüller, *Comput. Mater. Sci.* 6 (1996) 15 – 50.
- [43] J. P. Perdew, K. Burke, M. Ernzerhof, *Phys. Rev. Lett.* 77 (1996) 3865–3868.
- [44] H. J. Monkhorst, J. D. Pack, *Phys. Rev. B* 13 (1976) 5188–5192.
- [45] B. Drittler, M. Weinert, R. Zeller, P. H. Dederichs, *Phys. Rev. B* 39 (1989) 930–939.
- [46] A. V. Ponomareva, Y. N. Gornostyrev, I. A. Abrikosov, *Phys. Rev. B* 90 (2014) 014439.
- [47] V. Razumovskiy, A. Lozovoi, I. Razumovskii, *Acta Mater.* 82 (2015) 369 – 377.
- [48] A. Y. Lozovoi, A. T. Paxton, M. W. Finnis, *Phys. Rev. B* 74 (2006) 155416.
- [49] D. Warrington, P. Bufalini, *Scr. Metall.* 5 (1971) 771 – 776.
- [50] D. Scheiber, R. Pippan, P. Puschnig, L. Romaner, *Model. Simul. Mater. Sci. Eng.* 24 (2016) 035013.
- [51] V. I. Razumovskiy, D. Scheiber, I. M. Razumovskii, V. N. Butrim, A. S. Trushnikova, A. G. Beresnev, *Adv. Cond. Matter Phys.* 2018 (????) 9383981.
- [52] M. Shiga, M. Yamaguchi, H. Kaburaki, *Phys. Rev. B* 68 (2003) 245402.
- [53] D. D. Stefano, M. Mrovec, C. Elsässer, *Acta Mater.* 98 (2015) 306 – 312.
- [54] A. Tehranchi, W. Curtin, *J Mech. Phys. Solids* 101 (2017) 150 – 165.
- [55] S. Sanyal, U. V. Waghmare, P. R. Subramanian, M. F. X. Gigliotti, *Appl. Phys. Lett.* 93 (2008) 223113.
- [56] J. P. Perdew, A. Ruzsinszky, G. I. Csonka, O. A. Vydrov, G. E. Scuseria, L. A. Constantin, X. Zhou, K. Burke, *Phys. Rev. Lett.* 100 (2008) 136406.
- [57] J. P. Perdew, J. A. Chevary, S. H. Vosko, K. A. Jackson, M. R. Pederson, D. J. Singh, C. Fiolhais, *Phys. Rev. B* 46 (1992) 6671–6687.
- [58] P. Haas, F. Tran, P. Blaha, *Phys. Rev. B* 79 (2009) 085104.

- [59] S. He, P. Peng, O. I. Gorbatov, A. V. Ruban, *Phys. Rev. B* 94 (2016) 024111.
- [60] Y. Wang, Z.-K. Liu, L.-Q. Chen, *Acta Mater.* 52 (2004) 2665 – 2671.
- [61] H. M. Ledbetter, R. P. Reed, *J. Phys. Chem. Ref. Data* 2 (1973) 531–618.
- [62] G. H. O. Daalderop, P. J. Kelly, M. F. H. Schuurmans, *Phys. Rev. B* 41 (1990) 11919–11937.
- [63] V. S. Babu, A. S. Pavlovic, M. S. Seehra, *J. Appl. Phys.* 79 (1996) 5230–5232.
- [64] G. Schusteritsch, E. Kaxiras, *Model. Simul. Mater. Sci. Eng.* 20 (2012) 065007.
- [65] E. T. Bentría, I. K. Lefkaier, B. Bentría, *Mater. Sci. Eng. A* 577 (2013) 197 – 201.
- [66] W. Tyson, W. Miller, *Surf. Sci.* 62 (1977) 267 – 276.
- [67] T. Roth, *Mater. Sci. Eng.* 18 (1975) 183 – 192.
- [68] U. Aydin, L. Ismer, T. Hickel, J. Neugebauer, *Phys. Rev. B* 85 (2012) 155144.
- [69] Y.-A. Zhu, Y.-C. Dai, D. Chen, W.-K. Yuan, *Carbon* 45 (2007) 21 – 27.
- [70] D. J. Hepburn, D. Ferguson, S. Gardner, G. J. Ackland, *Phys. Rev. B* 88 (2013) 024115.
- [71] W. Chen, W. Xing, H. Ma, X. Ding, X.-Q. Chen, D. Li, Y. Li, *Calphad* 61 (2018) 41 – 49.
- [72] C. Papastaikoudis, B. Lengeler, W. Jager, *J. Phys. F: Met. Phys.* 13 (1983) 2257.
- [73] J. C. Slater, *J. Chem. Phys.* 41 (1964) 3199–3204.
- [74] G. Young, R. Najafabadi, W. Strohmayer, D. Baldey, B. Hamm, J. Harris, J. Sticht, E. Wimmer, *Tech. Report LM-03K047, NASA.* (June 16, 2003).
- [75] J. E. Angelo, N. R. Moody, M. I. Baskes, *Model. Simul. Mater. Sc.* 3 (1995) 289.
- [76] W. T. Geng, A. J. Freeman, G. B. Olson, *Phys. Rev. B* 63 (2001) 165415.
- [77] V. Razumovskiy, A. Lozovoi, I. Razumovskii, *Acta Mater.* 106 (2016) 401–402.
- [78] L. Vitos, A. Ruban, H. Skriver, J. Kollár, *Surf. Sci.* 411 (1998) 186 – 202.
- [79] R. Kohlhaas, P. Dunner, P. Schmitz, *Z. Angew. Physik* 23 (1967).
- [80] A. Alvaro, I. T. Jensen, N. Kheradmand, O. Løvvik, V. Olden, *Int. J. Hydrog. Energy* 40 (2015) 16892 – 16900.
- [81] M. Louthan, J. Donovan, G. Caskey, *Acta Metall.* 23 (????) 745–749.
- [82] J. von Pezold, L. Lymperakis, J. Neugebauer, *Acta Mater.* 59 (2011) 2969 – 2980.
- [83] D. Scheiber, L. Romaner, F. Fischer, J. Svoboda, *Scr. Mater.* 150 (2018) 110 – 114.

Chapter 7

Hydrogen enhanced intergranular failure of sulfur doped nickel grain boundary: In-situ electrochemical micro cantilever bending vs. DFT

7.1 Introduction

Grain boundary (GB) is known as a very common defect in metallic materials which possesses a higher energy comparing to the bulk crystal. Therefore the GBs are preferential sites for impurities to segregate. This segregation process is thermodynamically favourable, if it reduces the total energy of the system. Depending on the segregation energy difference between the grain boundary and free surface, segregated elements at the grain boundary can have a strengthening or embrittling effect on the GB cohesive energy [1, 2]. Fracture mode transition due to segregated elements to the GB is one of the most dangerous technical failures in metallic structures. Intergranular (IG) fracture proceeds quickly due to the interconnected network of the GBs and usually this type of failure is hard to be detected before the final rupture. Nickel (Ni), as one of the basic engineering materials, has a face centered cubic (FCC) crystal structure and, thanks to the greater number of slip systems available in this structure, it is intrinsically ductile [3]. However, IG fracture of this metal can happen even at room temperature, which is usually associated with GB segregation of impurity atoms [4, 5].

Various elements can be segregated in Ni GB. Comparing the embrittling effect of the different solute elements such as Sn, Sb, P, and S to the Ni GB, S was found to be one of the most detrimental GB segregating elements due to its high segregation potency and its impact on

the mechanical properties of the interfaces[6–8]. Sulfur (S) segregation to GBs in Ni, is reported to convert the fracture mode of the material to IG failure by changing the local cohesive strength of the GB [3]. The atomic hydrogen (H) is another deleterious element which can be introduced to the material throughout the manufacturing process or can be adsorbed under the service condition such as exposing to cathodic protection, corrosion processes or H-gas containing environment. The embrittling effect of H on Ni and Ni alloys, and the correlation between the solute H concentration and the fracture mode transition have been studied extensively [9–11]. Despite of the discrepancies on the involved embrittlement mechanism, there is an agreement in the literature upon fracture mode transition to IG fracture by increasing the H fugacity in the material [9]. Up to now, most IG failure studies to figure out the effect of segregated impurities such as H or S or their co-segregation on the mechanical properties of the alloy, are confined to polycrystalline materials. Due to the diversity in the GB type and heterogeneity of the segregated element concentration in each GB, testing a polycrystalline material, different overall critical S or H concentration amounts to induce IG cracking are reported in the literature. Therefore, using polycrystalline material, it is hard to find out a direct relationship between a selected GB type and segregation parameters and mechanical response of that specific GB. A few studies, albeit can be found which investigate a single GB. Vehoff et al. by growing a bicrystal, examined the effect of S and H on the GB embrittlement [12].

Introducing the focused ion beam - scanning electron microscopy (FIB-SEM) technology, nowadays it is possible to make series of identical micron sized specimens in favorable positions on the material. Micro cantilever bending test which has been drawn a lot of attention since its first use in 2005 [13], is an interesting method to explore the micro mechanical variation of the materials [14]. Putting an specific GB in the micro cantilever makes it more convenient to study the segregation and environmental parameters on the mechanical behaviour of the GB [15, 16]. Combining micro milling with electron back-scatter diffraction (EBSD) method, enables us to select the favorable GB and test a series of identical cantilevers under different circumstances. In addition, by confining the testing size to a micron scale and considering a specific GB, it is possible to compare the results to atomistic calculations, which can give fundamental understanding of the GB segregation and quantify the segregation-induced changes in GB cohesion. One of the prominent examples is the simulation of Hydrogen-enhanced decohesion (HEDE) of GB in Ni [7, 17–20], which has shown that atomic hydrogen tended to segregate to the Ni GB and demonstrated GB embrittling effect. Moreover, the synergistic effect between segregated impurities has drawn attention to the investigation of solutes co-segregation at GB, such as, H-Cr cosegregation in α -Fe GB [21, 22], C-O cosegregation in α -Ti GB [23], C, B, O, Fe, and Hf cosegregation in Mo GB [24], H-C and H-Mo cosegregation in Ni GB[20]. Although, S is known to segregate to Ni GB and embrittle the GB cohesion [25–28, 8], the H-S

interaction and its co-segregation effect as well as the kinetics of H-S segregation in Ni GB has not been studied well at the atomic level.

In this study, micro mechanical testing has been combined with atomistic calculations to study the co-segregation effect of the S and H co-segregation in the selected GBs. The microcantilever bending test has been utilized to look into the mechanical response of the GB segregated with S, H and also the co-segregation effect of them. Testing the selected GB by micro cantilever method provides a valuable results on the interaction of segregated impurities in GBs and their impact on the material property. So in the future, the obtained knowledge about the sensitive GB type can be used to strengthen the materials against environmental conditions by GB engineering[29–32]. From the computational side, it is focused on first principles investigation of the fundamentals of segregation and co-segregation of H with S in Ni and its effect on the GB cohesive strength in relation to the HEDE mechanism of HE using the Rice-Thomson-Wang theory of interface embrittlement [33, 34]. Furthermore, the kinetics of H and S segregation to Ni GB by using our calculated segregation energies from DFT and the Mclean was investigated. isotherm [35, 1, 36, 37].

7.2 Method

7.2.1 Materials and characterization

Two types of pure nickel and grain boundary sulfur doped nickel samples were used in this study. The polycrystalline high purity nickel (99.99 %) produced by zone refining process. Disc shape sample with a diameter of 12 mm and thickness of 4 mm annealed in vacuum at 1250 °C for 72 h followed by furnace cooling as the final heat treatment step. The annealing process let the grains to grow to an average size of ~ 2 mm and obtain grain boundaries perpendicular to the surface of the sample [38]. The sulfur doped sample contains 5.4 wtppm of sulfur in solid solution condition measured by glow discharge mass spectroscopy technique. Following casting, hot rolling and cold rolling processes were carried out to decrease the thickness of the ingot to 3 mm. Afterwards, the material was annealed 72 h at 1300 °C and 24 h at 1000 °C followed by water cooling. The average grain size of ~ 350 μm was obtained at this step. Equilibrating the material for 60 days at 600 °C resulted in grain boundary sulfur segregation. Wavelength dispersive X-ray spectroscopy measurements were conducted for detecting the segregated sulfur amount to the selected grain boundaries as described in [39]. Sulfur was the only segregated element detected at the grain boundary. The sulfur measurement profiles alongside the corresponding SEM images of the GBs are shown in Fig. 7.1. According to the measurements the doped sulfur amount to the GB can vary between 27 to 57 ng cm^{-1} .

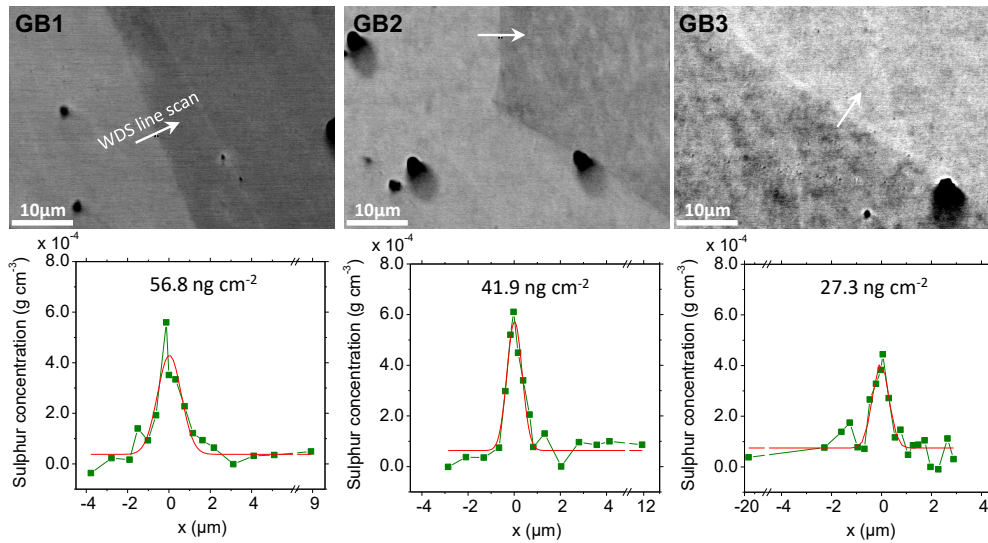


Fig. 7.1 Sulfur concentration profiles of three different grain boundaries across the indicated lines in the scanning electron microscopy images measured by wavelength dispersive spectroscopy on the nickel sample with 5.4 wt.ppm. bulk sulfur, annealed 60 days at 600 °C.

Table 7.1 The sulfur content and structural information of selected GBs

| GB ID | WDS measured GB S conc. (ng cm ⁻¹) | GB angle vs. sample surface (°) | Corrected S conc. (ng cm ⁻¹) | Sigma | Misorientation Angle (°) |
|-------|--|---------------------------------|--|-------|--------------------------|
| GB1 | 56.8 | 82.4 | 56.3 | - | 54.2 |
| GB2 | 41.9 | 28.8 | 20.2 | - | 3.6 |
| GB3 | 27.3 | 92 | 27.3 | 5 | 35.6 |

The sample's surface were prepared by normal grinding and finally electropolished in a solution of 1 Molar methanolic H_2SO_4 to reach a maximum surface roughness of $\sim 1 \text{ nm}/\mu\text{m}^2$ [40]. The electropolishing process was carried out at 30 V for 30 s. The electron backscattered diffraction (EBSD) characterization was used to select the grain boundaries of interest in both pure and sulfur doped nickel samples.

7.2.2 Micro cantilever milling and testing

Bicrystal micro-cantilevers were milled by FEI Helios DualBeamTM FIB system on the grain boundaries listed in Table 7.2 to the dimensions presented in Fig. 7.2(c). The GB angle relative to the sample surface was checked to be in the range of 80 to 90 degree prior to milling of the bi-crystal beams as shown in Fig. 7.2(c₁) and (c₂). The tested GB in the pure Ni sample are named as PNi1, NiS1 as a random GB and NiS2 as $\Sigma 5$ type GB were assigned for testing on the sulfur doped sample. To obtain a clean surface the ion current density of 98 pA at 30 kV was selected during the final cleaning step. To intentionally intensify the stress concentration

to the GB, a notch with the very low current density of 9.8 pA was milled aiming the grain boundary to be positioned right below the notch.

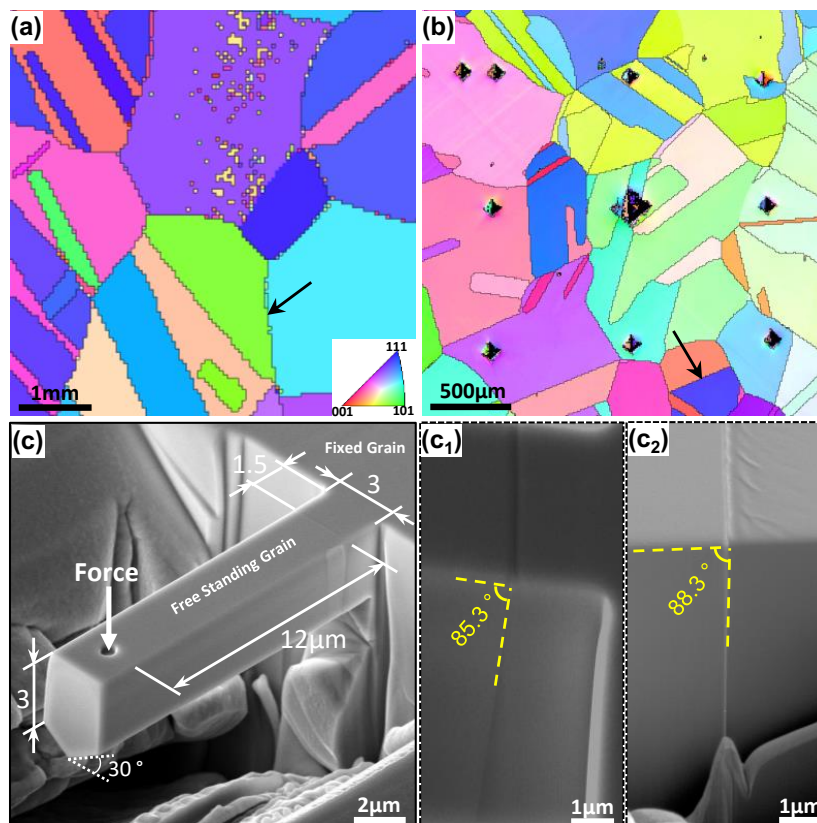


Fig. 7.2 The inverse pole figure map of the studied (a) pure nickel and (b) grain boundary sulfur doped nickel samples. The selected grain boundaries for cantilever milling is marked by black arrows. (c) Representative dimensions of the bi-crystal cantilevers. Selected grain boundary angle to the sample surface in (c₁) pure nickel and (c₂) sulfur doped specimen NiS1.

The micro beam bending tests were performed in two hydrogen free and in situ electrochemical hydrogen charged conditions using Hysitron TI 950 TriboIndenter[®] system. Displacement control mode was used to bend the cantilevers with the displacement rate of 2 nm s^{-1} at room temperature. A long shaft conical tip with a nominal tip radius of 500 nm, was used for bending the cantilevers in liquid. A miniaturized three electrode electrochemical setup consisted of platinum counter-, working- and Hg/HgSO₄-reference electrodes was used in this study. The reference electrode was connected to the cell through a double junction integrated to the TriboIndenter to perform the in situ bending tests [41, 42].

The micro beam were charged with a cathodic current density in the range of -60 to $-100 \mu\text{A cm}^{-1}$ at -1450 to -1600 mV potential versus the Hg/HgSO₄ reference electrode. Glycerol based solution with the composition of 1.3 M borax in glycerol mixed with 20 %

distilled water [43] used as the hydrogen charging electrolyte. Additional bending tests were done on the grain boundary called NiS2 which were hydrogen charged by the glycerol based solution with the addition of 0.002 M $Na_2S_2O_4$ to the solution as the hydrogen recombination poison. High resolution scanning electron microscopy imaging and cross sectional slicing by FIB were used to track the crack propagation path versus the grain boundary position.

Table 7.2 Tested grain boundaries misorientation angle and corresponding information in pure nickel (PNi1) and sulfur doped (NiS1 and NiS2) specimens.

| GB ID | Angle (°) | Axis | | | Sigma | Plane 1 (fixed grain) | | | Plane 2 (free standing grain) | | |
|-------|-----------|------|-----|----|-------|-----------------------|-----|----|-------------------------------|-----|-----|
| | | h | k | l | | u | v | w | u | v | w |
| PNi1 | 47.3 | -2 | 12 | 19 | - | 16 | 19 | 14 | -4 | -29 | -8 |
| NiS1 | 46.6 | 21 | 5 | 16 | - | -9 | -4 | 4 | 2 | -21 | -12 |
| NiS2 | 35.6 | 1 | -29 | 1 | 5 | 18 | -17 | 10 | 18 | -17 | 9 |

7.2.3 Computational details

Spin polarized density functional theory (DFT) calculations have been performed using the projector-augmented-wave (PAW) [44, 45] method as implemented in the Vienna *Ab initio* simulation package (VASP) [46, 47]. The Perdew-Burke-Ernzerhof (PBE) form of generalized gradient approximation (GGA) has been used for the exchange-correlation potential [48]. The plane-wave basis set cutoff energy has been set to 400 eV. The convergence criteria of self-consistent calculations have been set to 10^{-5} eV/cell for the total energy and to 9×10^{-3} eV/Å for the atomic forces. The integration over the Brillouin zone has been done using the $4 \times 4 \times 1$ Monkhorst-Pack k -mesh [49] for all slab geometries calculations and using the $4 \times 4 \times 4$ k -mesh in the $3 \times 3 \times 3$ [conventional f.c.c. cell] bulk supercell calculations. The lattice parameter has been fixed to 3.515 \AA [20] and only the ions have been allowed to relax in all slab and bulk calculations. The Ni $\Sigma 5(012)$ coincidence site lattice (CSL) symmetric tilt GBs has been modeled using a 76-atom GB slab with 19 layers and 4 atom/layer [20]. The Ni $\Sigma 5(012)$ GB structure used in this work and illustration of GB cleavage are shown in Fig. 7.3.

The site preference of H and S impurities in the bulk of fcc Ni has been studied by means of DFT calculations in a number of publications [19, 20, 50–52]. The results have shown that H prefers to occupy the octahedral interstitial site [19, 20, 51, 52] and S substitutes the lattice sites [50, 51] in the bulk. Here, we use these results and define the GB segregation energy as the total energy difference between the bulk of the material with an impurity atom occupying the most stable site (interstitial octahedral for H and substitutional for S) and the system with an the impurity atom situated at the GB (both substitutional and interstitial sites

are considered). The methodology for GB segregation energy (E_{seg}^{gb}) and the work of separation W_{sep} DFT calculations is described in Refs. [8, 20] in detail.

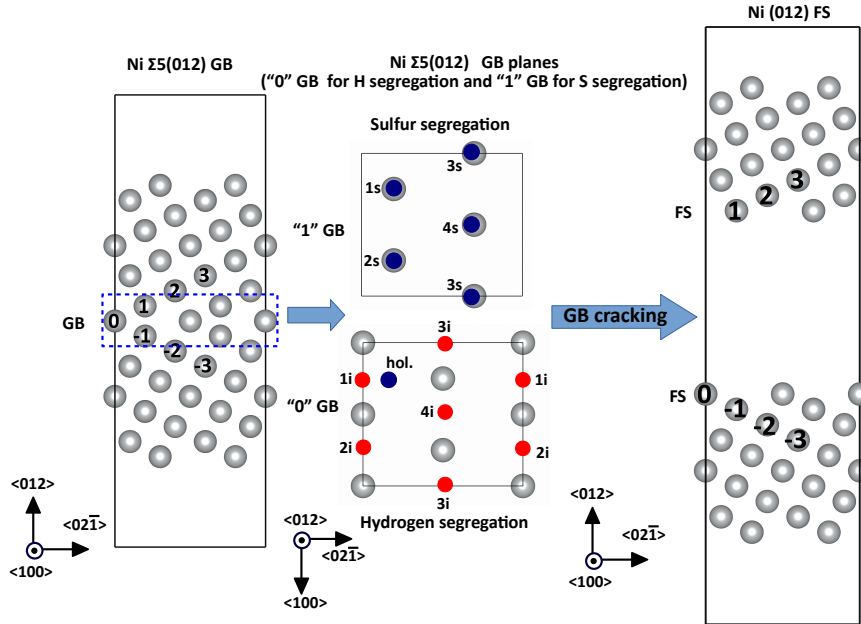


Fig. 7.3 Illustration of cracking at Ni Σ 5 (012) [100] symmetric tilt GB. "0" and "1" GB planes with interstitial H and substitutional S atoms are also shown respectively.

The GB enrichment of H and S at $T > 0$ has been modeled by means of a modified McLean isotherm [35, 1, 36, 37], which takes as input GB segregation energy profiles from DFT calculations. In contrast to the classical equilibrium segregation isotherm, the used model takes into account possible effects of grain size (solute depletion in the bulk) and the kinetics of segregation. The details of the model are given in Refs [36, 37].

The ideal work of separation W_{sep} that is a fundamental thermodynamic quantity that controls the mechanical strength of an interface has been chosen to evaluate resistance of the selected GB to decohesion. Reduction of the W_{sep} indicates reduction of the cohesive strength of an interface. However, it does not automatically mean that the interface will fracture in a brittle manner [34]. Another condition has to be satisfied: $W_{sep} < G_{disl}$, where G_{disl} is the minimal energy per unit area of crack advance required to emit a single dislocation. The latter can be estimated to be in the range between 1-3 J/m² for Ni depending on the applied shear stress level, orientation of the GB, temperature and the stress rate [53]. An alternative way of estimating brittle to ductile fracture mode is the R ratio of the W_{sep} to twice the free surface energy of the metal [54, 55]:

$$R = \frac{W_{\text{sep}}}{2\gamma_{\text{fs}}^{\text{PCP}}}, \quad (7.1)$$

here $\gamma_{\text{fs}}^{\text{PCP}}$ denotes the surface energy of the preferred cleavage plane, which for fcc metals is mainly the (111) plane [56]. Free surface energy of Ni (111) surface is obtained by $\gamma_{\text{fs}}^{\text{PCP}} = (E_{\text{fs}} - N * \epsilon_0) / 2A_{\text{fs}}$, where E_{fs} is the total energy of FS slab, N is the total atom number and A_{fs} the area of FS slab. If R is close to unity, transgranular cleavage is expected, while for lower values the IG fracture is expected.

7.3 Results

7.3.1 Bending of the bi-crystal micro cantilevers

7.3.1.1 Pure Nickel grain boundary

Fig. 7.4(a) shows the representative load-displacement (L-D) curves of the pure nickel bi-crystal micro beams obtained in two different experimental conditions of H-free environment and in situ electrochemical H-charging. Although the elastic stiffness is well matched for the two sets of the curves and all the tested beams have relatively a similar yield point, there are obvious differences in plastic regime. The cantilever bent in H-free condition shows slight hardening up to reaching the maximum load at $\sim 2.5 \mu\text{m}$ displacement follows by gradual reduction in the flow curve to the final $5 \mu\text{m}$ displacement. from the Fig. 7.4(a) it can also be inferred that the work hardening rate of the H-charged beams is higher than of the H-free one. In addition, the maximum load of the H-charged beams reach to higher values in comparison with H-free testing condition. In the case of H-charged beams the reduction in the flow curve, due to crack formation, takes place at the ~ 1 to $1.5 \mu\text{m}$ displacement. The continuous decrease in the loading force of the hydrogen charged beams can be an indication for the H-induced cracking and decrease in the cross sectional length of the beams which is lead to reduction in the required force for continuing the test.

Fig. 7.5(a₁ to a₃) and (b₁ to b₃) shows the post deformation micrographs of the bi-crystal pure nickel beams bent in H-free and H-charged conditions, respectively. As it is evident from Fig. 7.5(a₁ and a₂) for H free condition, the notch is blunted along abundant slip traces visible in the top and the cross sectional surfaces in adjacent crystals of the beam. According to the Schmid's law the observed slip traces in the free standing and the fixed side of the bi-crystal beam are due to the activation of the dislocation on (-1 -1 1) plane in fixed-grain and (1 -1 -1) plane with Schmid value of 0.35 and 0.48, respectively. This phenomena demonstrates that the

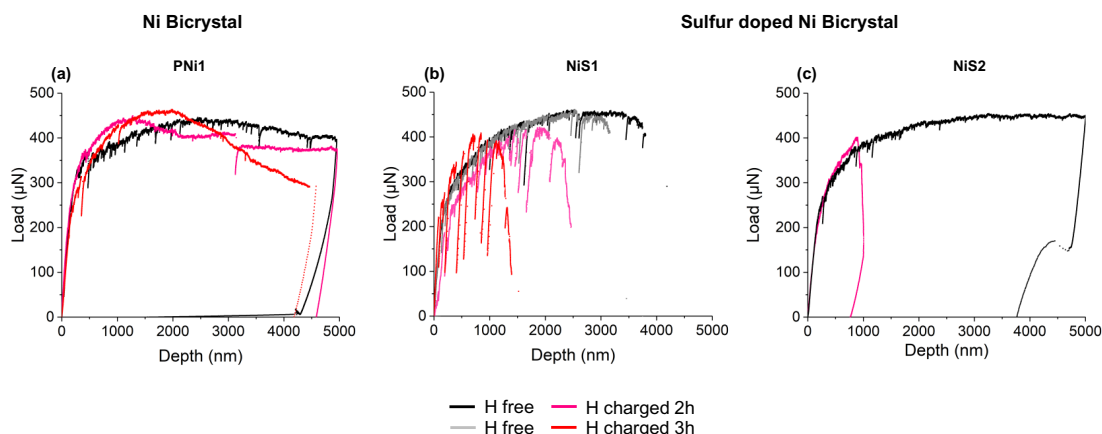


Fig. 7.4 Load-displacement curves of the (a) pure nickel (grain boundary PNi1 in table 7.2) and (b) and (c) sulfur doped (grain boundary NiS1 and NiS2 in table 7.2, respectively) bi-crystal beams tested with hydrogen free and in situ electrochemical hydrogen charging conditions.

plasticity during the deformation is not only presents in the notch area but it also spreads out to the fixed and free standing grains in the bi-crystal beam as shown by yellow dashed lines.

The white arrow in the Fig. 7.5(a₃) exhibits the grain boundary positioned beneath the notch withstanding the plasticity with no evidence of intergranular cracking. the schematic diagram can better show the deviation of the Gb from its original straight form which shows a great amount of plasticity beneath the notch. The observed chain of the micro voids in the notched area is also an strong proof for the domination of plasticity in the H-free testing condition. In contrast to the beams bent in H-free condition, crack propagation from the notch position was observed for the H-charged beams which was the reason for the continues decrease in the corresponding L-D curve in Fig. 7.4(a). A closer cross sectional view of the cracked beam in Fig. 7.5(b₂) illustrates less slip traces compared to H-free tested beams which is an indication for the lower plasticity and its confinement to the notch area in the H-charged beams. from the figure it is also obvious that the crack did not follow the GB path as depicted in schematic diagram. Alternatively, it has initiated from the notch itself and propagates in cranked-like form in the fracture surface. Further slicing through the thickness of the beam by FIB (Fig. 7.5(b₄)) has also demonstrated that the crack is not intergranular and it deviates to the neighboring grain. Noticing the formation of a dimple in the crack path in this figure is an evidence that the failure was not brittle.

7.3.1.2 Sulfur doped nickel grain boundary

The L-D curves of the S-doped bi-crystal beams with the GB NiS1 and NiS2 are shown in Fig. 7.4(b) and (c), respectively. For NiS1 cantilevers, the bent beams show a rapid decrease in

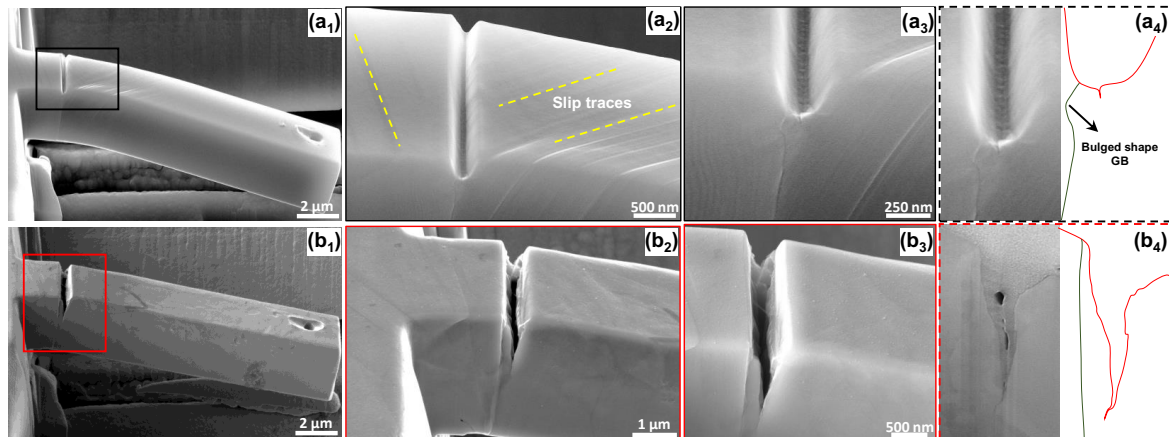


Fig. 7.5 Post deformation secondary electron images from the side view of the pure nickel bi-crystal beams (grain boundary PNi1 in table 7.2) tested with hydrogen free (a₁ to a₃) and in situ hydrogen charging (b₁ to b₃) conditions.

the load after reaching a maximum load of ~ 450 and ~ 400 μN in the H-free and H-charged environmental conditions, respectively. The sharp load reduction with considerably higher slope comparing to the pure nickel results is attributed to the detrimental effect of the sulfur impurity segregation to the grain boundary. Testing the beams in the H-charged condition decreased the displacement to about 2.5 and 1.5 micrometer after 2 and 3 h of charging. However, the GB embrittling degree of the material is strongly dependent on the content of the segregated elements and also the type of the subjected GB. To refer this, another type of GB with different misorientation angle and segregated sulfur comparing to NiS1 was examined. Fig. 7.4(c) shows the L-D curve of the NiS2 GB which is a $\Sigma 5$ type and has around 11° misorientation lower than the NiS1.

In H-free condition, no rapid load drop is observed in NiS2 in contrast to NiS1 beams and the load is leveled off on the maximum load of ~ 450 μN up to the final displacement of 5 μm , similar to the case of PNi1 GB. However, introducing H into the sulfur doped GB system, caused a distinct change in the L-D behaviour compared to H-free condition. A reduction of the final tolerated displacement to the 1 μm can be a strong indication of the mixed collaboration of the H and the S atoms in the weakening of the GB strength. Comparing Fig. 7.4 (a) and (c), one can obtain that, in such a condition the only presence of S or H in the system may not result in a deleterious effect on the GB embrittling. However, combining them together can cause a dramatic failure in the system.

Post deformation micrographs of the beams containing the grain boundaries of NiS1 and NiS2 bent in H-free testing condition are shown in Fig. 7.6(a₁ to a₄) and (b₁ to b₄), respectively. The NiS1 bi-crystal beam shows a straight and sharp grain boundary opening with a complete

brittle type fracture surface which cut the notch area and results in the formation of jagged shaped cleavage pattern in the coincidence place of the GB and the notch as depicted in the Fig. 7.6(a₃,a₄). From the figure it can also be inferred that the stress concentration in NiS1 is mostly localized to the GB and less slip traces can be observed on the neighboring grains of the cantilever. By contrast, the greater plasticity of NiS2 compared to NiS1 can be elucidated from the abundant and spread slip traces in specially free standing side of the beam. Although a crack nucleation can be observed in the GB (as noted in Fig. 7.6(b₃, b₄), the notch blunting and high plasticity prevail the deformation process. So it can be deduced that in both sulfur doped grain boundaries (NiS1 and NiS2) the crack is initiated from grain boundaries rather than the notch area. However, due to dissimilarity of the grain boundaries, the severity of the GB opening was different. In NiS1 the grain boundary opening reaches to the notch area, while in NiS2 it was stopped before reaching to the notch surface. The different behaviour of these two boundaries are more significant considering that the final displacement of the beam containing GB NiS2 was 5 μm while for the NiS1 sample was about 3 μm at the stage of the sharp load drop as shown in Fig. 7.4 (b) and (C).

For both type of GBs, co-existence of the H alongside with the S caused the complete brittle fracture in the GB plane and completely detachment of the free standing part of the beam as shown in Fig. 7.7 (a₁ and a₂). The angled crack path in the remaining fixed side of the beams shown in figure Fig. 7.7(a₁2) is an indication that the crack follows the GB. Although, the presence of H increases the brittleness of the metal, previous works show [57] that the fracture surface is usually formed with the mixed brittle and ductile features. Here, the action of H together with the segregated S leads to produce a completely smooth surface without any ductile features. This shows a fully brittle characteristics of the crack in NiS1 which is formed by decohesion of the grain boundary. Accordingly, the sharp crack propagation in the NiS2 GB after 2 h H charging represented itself with a sudden load drop at $\sim 1 \mu\text{m}$ displacement in the L-D curve as shown in Fig. 7.4(c). It should be noted that the used solution for H charging of the beams with NiS2 GB contained the H recombination poison. The used solution helps to charge the sample to higher H concentration. The observed crack nucleation and propagation at very low displacement in comparison with H-free condition shows the co-segregation effect of the H and the S on the decohesion of the GB.

7.3.2 Computational results

7.3.2.1 H and S segregation to Ni GB

The calculated GB segregation profiles of 0.25 ML of H and S impurities located in the first four GB layers as a function of distance from the GB plane are shown in Figure 7.8. The results

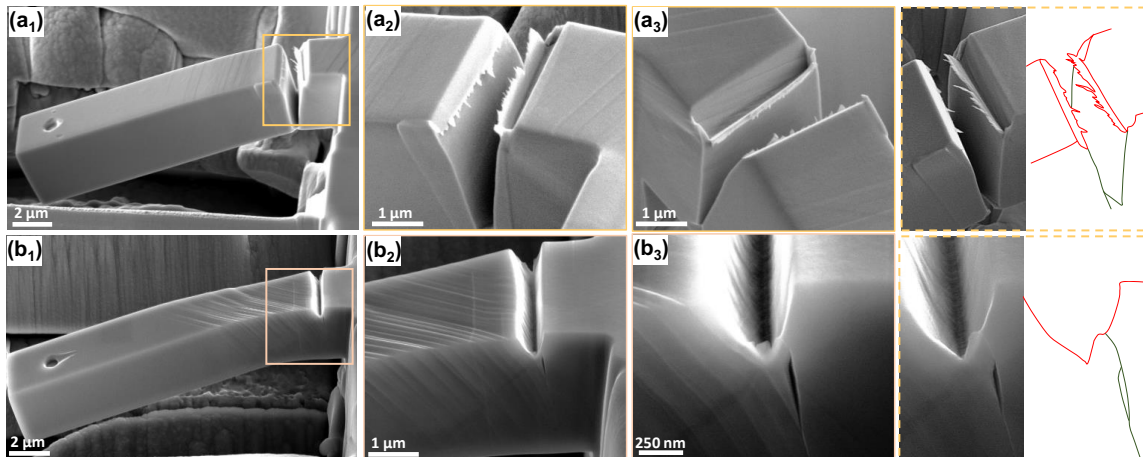


Fig. 7.6 Secondary electron images from the side view of the bi-crystal beams on the grain boundary sulfur doped sample with (a₁ to a₃) grain boundary NiS1 and (b₁ to b₃) grain boundary NiS2 in table 7.2 bent with hydrogen free condition.

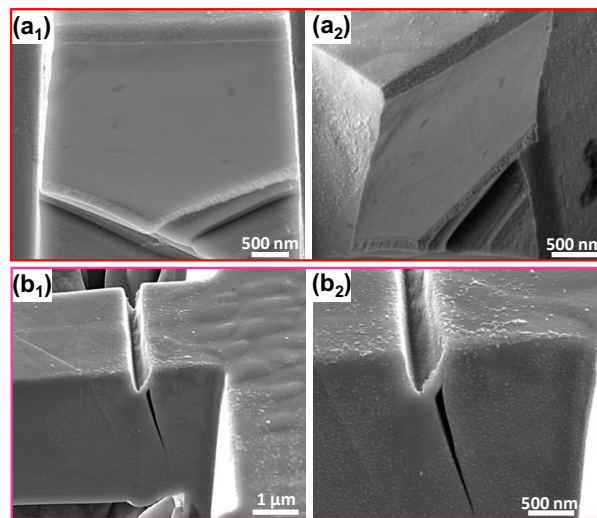


Fig. 7.7 Secondary electron images from the fracture surface of the beam with grain boundary NiS1 (a₁ and a₂) and the crack propagation path in NiS2 (b₁ and b₂) bent with in situ electrochemical H charging condition.

are found to be in good agreement with available literature data [19, 20, 58]. In Fig. 7.8, one can see that H prefers to occupy the interstitial sites within the GB layer (GB layer "0" in the Fig. 7.3). Specifically, H prefers the "bridge" interstitial sites (shown by 1i–4i in Fig. 7.3). S on the other hand has the lowest segregation energy corresponding to its segregation to the substitutional sites (1s–4s) in the next to GB ("1") layer. Our results also show that there is a little energy difference between the substitutional site and the "hollow" interstitial site for S (shown in Fig. 7.3 by *hol.* in "0" GB layer). The calculated segregation energy of -1.59

eV/atom for S is in good agreement with previous DFT investigations [58] and experimentally measured value of -1.48 eV/atom [59]. We have also found an additional not reported earlier segregation site for S atoms located at the interstitial inter-space between layers 0 and 1 with the energy of -0.75 eV/S-atom.

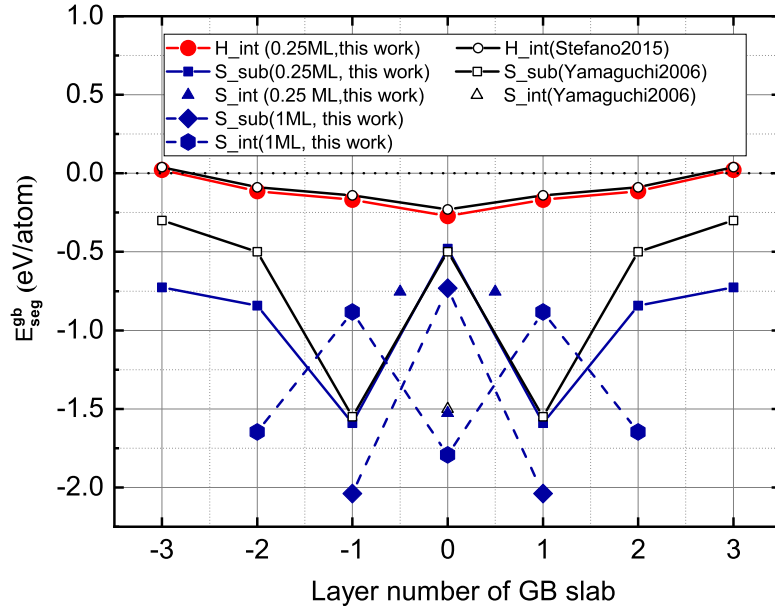


Fig. 7.8 H and S segregation profiles at $\Sigma 5$ (012) GB in Ni compared to the literature data [19, 58]. The S segregation energies are shown for 0.25 ML and 1ML coverage by using scatter-line and scatter-dashline respectively. The layer number corresponding to the segregation energy profile calculations are shown in Fig. 7.3.

In addition to segregation profiles, we have investigated a possible effect of the GB excess on the segregation energy of H and S. In Fig. 7.9, we show the E_{seg}^{gb} dependence on the GB excess of segregating elements ranging from 0.25 to 1 ML impurity excess (only averaged over all possible atomic configurations numbers corresponding to each GB excess are shown). H exhibits virtually no GB excess dependence with a shallow local minimum of average segregation energy of H at a coverage of 0.5 ML, which has been observed in a number of previous DFT investigations [20, 60, 61]. S atoms show an attractive interaction with about 0.20 eV reduction of E_{seg}^{gb} by changing S GB excess from 0.25 to 1 ML. This result is in good agreement with the theoretical results of the Refs. [8, 58] and the results of the experimental investigation in Ref. [62] where the observed S GB content was estimated to be in the range of about 1 ML.

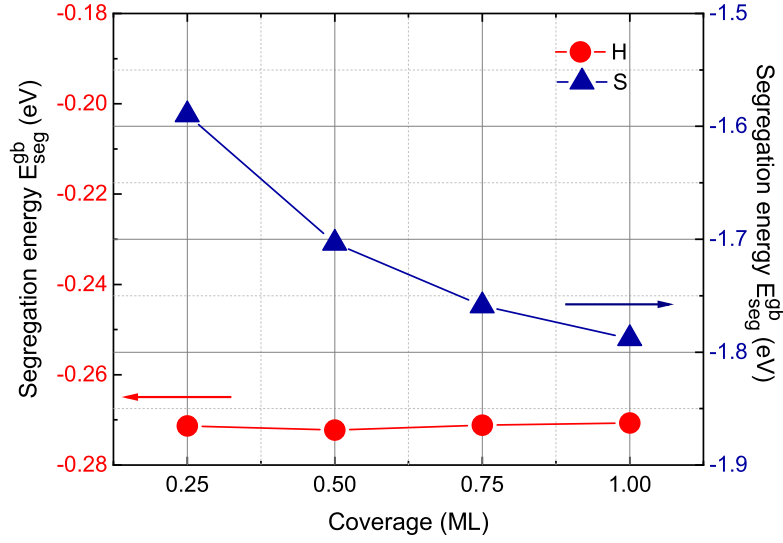


Fig. 7.9 Coverage change effect on the H and S GB segregation energies. The coverage of 0.25–1 ML for interstitial H at "0" GB layer and substitutional S at "1" GB layer are shown separately.

7.3.2.2 Interaction between segregating atoms at Ni GB

The interaction energies between H and S atoms at the GB in Ni have been investigated by DFT calculations as well and the results are shown in Table 7.3. The interactions have been obtained for four different S and H GB excesses (0.25, 0.5, 0.75, and 1ML) and only the averaged over all possible configurations for each GB excess values (if applicable) are shown in the table. The interaction energy between the impurity atoms located at the GB E^{int} has been defined as:

$$E^{\text{int}} = E_{\text{slab}}^{\text{gb}}[N-n; m; n] + (n+m-1)E_{\text{slab}}^{\text{gb}}[N; 0; 0] - mE_{\text{slab}}^{\text{gb}}[N; m; 0] - nE_{\text{slab}}^{\text{gb}}[N-n; 0; n] \quad (7.2)$$

where $E_{\text{slab}}^{\text{gb}}[N; m; n]$ is the total energy of the GB slab with m H atom(s) and n S atom(s) at the GB, $E_{\text{slab}}^{\text{gb}}[N; 0; 0]$ is the energy of a slab with no impurity atoms, $E_{\text{slab}}^{\text{gb}}[N; 0; n]$ energy of a slab with n S atoms and $E_{\text{slab}}^{\text{gb}}[N; m; 0]$ energy of a slab with m H atoms.

The results suggest that there are weak repulsive interactions between H and S atoms resulting in the interaction energies in the range of 0.05-0.08 eV/H-S couple. These interactions are slightly larger than H-H interactions reported in the previous section but they are still significantly lower than S-S interactions that range between -0.23 and -0.264 eV/S-S couple and non-linearly increase with increasing S GB excess. The absolute value and the repulsive character of H-S interactions suggest that the GB segregation of S atoms should not be strongly

affected by H co-segregation and vice versa. The main factor influencing S GB segregation is the concentration of S at the GB while the GB segregation of H seems to be quite inert to any GB compositional changes.

The co-segregation effects have been additionally evaluated by calculating a difference between the interaction energy E^{int} and the sum of individual interaction energies of the atomic couples (S-S, H-H and S-H) forming the segregation layer $\sum E_{i-j}^{\text{int}}$ as:

$$\delta = E^{\text{int}} - \sum E_{i-j}^{\text{int}}. \quad (7.3)$$

Small values of δ shown in Table 7.3 for all investigated combinations of H and S GB excess values suggest very weak synergistic effects between H and S atoms of the order of less than 0.03 eV.

Table 7.3 The calculated interaction energies between the segregating elements at the GB E^{int} (eV), the difference between the interaction energy E^{int} and the sum of individual interaction energies of the atomic couples (S-S, H-H and S-H) forming the segregation layer δ (eV), work of separation (J/m^2), the reduction of the work of separation reduction in %, and the ratio R calculated from Eq. 7.1.

| GB system | GB coverage (ML) | | E^{int} | δ | W_{sep} | $\Delta W_{\text{sep}}(\%)$ | R |
|------------|------------------|------|------------------|----------|------------------|-----------------------------|------|
| | S | H | | | | | |
| Ni | – | – | – | – | 3.508 | – | 0.91 |
| Ni+H | – | 0.25 | – | – | 3.414 | –2.69 | 0.89 |
| | – | 0.50 | 0.000 | – | 3.321 | –5.33 | 0.87 |
| | – | 0.75 | 0.000 | 0.000 | 3.201 | –8.75 | 0.83 |
| | – | 1.00 | 0.002 | 0.002 | 3.084 | –12.09 | 0.80 |
| Ni+S | 0.25 | – | – | – | 3.187 | –9.19 | 0.83 |
| | 0.50 | – | –0.228 | 0 | 2.927 | –16.62 | 0.76 |
| | 0.75 | – | –0.508 | –0.052 | 2.628 | –25.13 | 0.69 |
| | 1.00 | – | –0.793 | –0.057 | 2.286 | –34.88 | 0.60 |
| Ni+(S & H) | 0.25 | 0.25 | 0.061 | – | 3.106 | –11.47 | 0.81 |
| | 0.50 | 0.25 | –0.101 | 0.005 | 2.797 | –20.28 | 0.73 |
| | 0.75 | 0.25 | –0.296 | 0.029 | 2.524 | –28.06 | 0.66 |
| | 1.00 | 0.25 | –0.567 | –0.018 | 2.178 | –37.93 | 0.57 |
| | 0.25 | 0.50 | 0.119 | –0.003 | 2.967 | –15.42 | 0.77 |
| | 0.25 | 0.75 | 0.154 | –0.029 | 2.839 | –19.08 | 0.74 |
| | 0.25 | 1.00 | 0.223 | –0.022 | 2.701 | –22.99 | 0.70 |

7.3.2.3 Kinetics of H and S segregation to Ni GB

The enrichment of GBs with S and H atoms has been calculated using the DFT segregation profiles shown in Fig. 7.8 (corresponding to 0.25 ML GB excess for H and 1 ML for S) and the segregation models described in Refs. [36, 37]. Following the results of the previous sections, the interactions between H and S atoms have been neglected. The results on S segregation have been obtained by concentration averaging over the interstitial and substitutional positions in the first three GB layers, whereas only interstitial positions have been considered in the case of H segregation. The average grain size of 350 μm and the initial bulk amount of S equal to 5.4 wt.ppm (10 at.ppm) have been taken from the results of Section 7.2.1. The information about H content in the Ni samples during charging has been estimated to vary from 50 to 300 at.ppm. The GB width has been taken from the segregation energy profiles shown in Fig. 7.8 equal to 8 \AA . The bulk diffusion parameters for the diffusion coefficients of S and H in Ni in the form $D = D_0 \exp E_a/k_B T$ have been set to $D_0 = 1.4 \times 10^{-4} \text{m}^2/\text{s}$; $E_a = 2.28 \text{ eV}$ [63] and $D_0 = 4.47 \times 10^{-7} \text{m}^2/\text{s}$; $E_a = 0.37 \text{ eV}$ [64] respectively. The grains have been discretized into shells with a thickness of 1 μm . The information about the heat treatment history of the sample has been taken from Section 7.2.1 and divided into 2 intervals of our interest: I) annealing; II) H-charging.

The modeling results are shown in Fig. 7.10, where the left side of the figure refers to the 3-step annealing process (stage I) of 1300°C for 72h \rightarrow air cooling ($t' = 10^\circ\text{C}/\text{sec}$) \rightarrow 1000°C for 24h \rightarrow water cooling ($t' = 100^\circ\text{C}/\text{sec}$) \rightarrow 600°C for 60 days and the right part to H-charging at 300°C for 10h. The top panels show the evolution of temperature as a function of time. The bottom panels show the amount of S and H segregating to the GB in Ni as a function of the heat treatment time.

During the simulated 3-step annealing process, S enrichment at the GB reaches 75 at.% at the end of the I stage of the heat treatment. This number is slightly below the theoretical equilibrium enrichment of S at 600°C of 78 at.% and suggests that S has almost reached its equilibrium GB concentration after the annealing in the experiment. Here, we would like to note that the equilibrium S GB excess at the room temperature is about 100 at. % and the obtained amount of 75 at.% of S at the GB is a result of the instant quenching from 600°C to the room temperature at the end of stage I of the heat treatment. The content of S stays constant during the H-charging (stage II). The amount of H going to the GB after charging (stage II) varies from 10 to 18 at.% , which corresponds to the equilibrium values for the assumed H contents from 50 to 300 at.ppm in the bulk of Ni, respectively. In summary, we estimate about 75 at.% of S and 10-20 at.% of H at the GB after stages I and II of the heat treatment at the selected $\Sigma 5(210)$ GB.

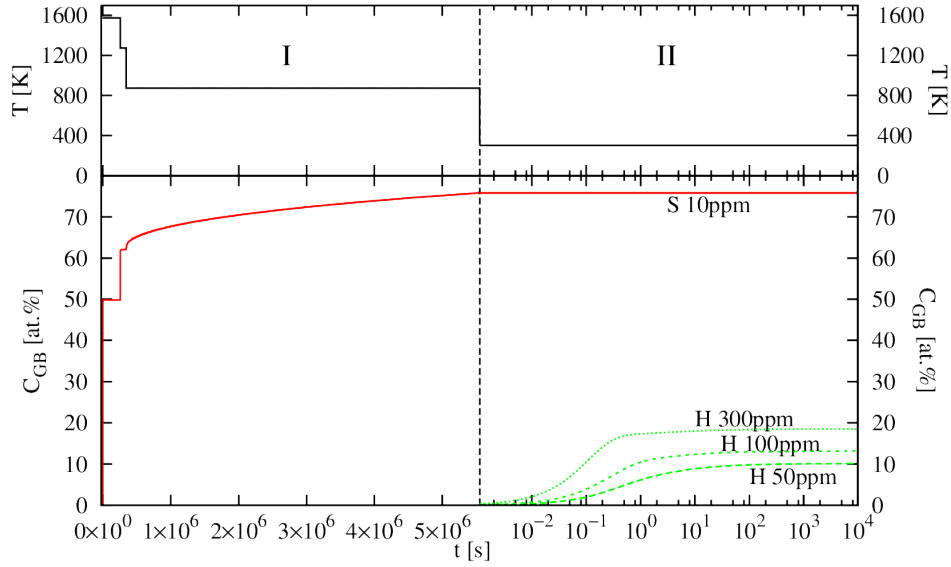


Fig. 7.10 Enrichment of S and H at Ni GB as a function of temperature and time. The upper panel shows temperature changes during sample preparation and H charging. The dashed vertical line splits two stages of sample treatment: I) 3-step annealing and II) H charging. Assumed in the calculations bulk concentrations of S and H are given next to the corresponding concentration profiles. All concentrations are given in at.% and at.ppm.

The calculated S GB content of 75% (after stage I heat treatment in Figure 7.10) can be compared to the estimated S GB concentration from the experimental WDS measurements of S segregation profiles shown in Table 7.1. To do so, we have converted S GB content values reported in ng/cm^2 into ML using a conversion factor reported in [62]. The theoretical prediction of S GB excess after stage I heat treatment should be close to the experimental GB S content at the GB with the highest misorientation angle, i.e. GB1 from Table 7.1. Indeed, our calculated value of 75% corresponding to 0.75 ML/layer on average for the given GB is in reasonably good agreement with the experimental value of 0.84 ML from the WDS experimental measurements. Here, it should be noted that GB excess of impurity atoms strongly depends on the GB structure and the current comparison is valid under the assumption that both theoretical and experimental GB structures are close to each other.

7.3.2.4 GB decohesion by H and S

The effect of H and S on the W_{sep} of the $\Sigma 5(210)$ GB in Ni is shown in Fig. 7.11. Here, we show W_{sep} as a function of GB coverage x by $x\text{-H}$, $x\text{-S}$, $0.25\text{S}+x\text{H}$ and $0.25\text{H}+x\text{S}$ segregating atoms. Both elements decrease W_{sep} and reduce GB resistance to decohesion. In absolute values, the effect of S on the GB decohesion is much more pronounced than that of H. Variations of S GB excess (coverage) have a more pronounced than H influence on W_{sep} as well. However, it is

the simultaneous segregation of both H and S atoms to the GB in Ni results that has the most pronounced GB decohesion among all considered cases reducing it by as much as about 30% (see Table 7.3).

As it has already been mentioned in Sec. 7.2.3, reduction of W_{sep} by itself is not sufficient to describe GB embrittlement of a material. The upper estimate of G_{disl} of about 3 J/m² and the results presented in Figure 7.11 suggest that a brittle fracture can be expected at already low GB coverage by S atoms while a significantly higher fraction of H atoms at GB can be required to promote brittle fracture in Ni. An alternative estimate based on the calculations of the R ratio by using Eq.7.1 shown in Table 7.3, also demonstrates that the increase of S GB excess decreases R (reduces ductility of the GB) in a much more pronounced manner than increasing H GB excess. However, the combined effect of both H and S atoms segregating to the GB in Ni result in the most detrimental of all effects on the reduction of R at 1ML of S and 0.25 ML GB excess of H, suggesting that S-rich GBs should be especially prone to HE even at low H GB concentration levels. The calculated amounts of S (0.75 ML) and H (0.1-0.2 ML) at the GB after stages I and II of the heat treatment described in the previous section result in $R = 0.66$ which is the second lowest R value (the lowest belongs to 1 ML of S and 0.25 ML of H) with about 28 % reduction of the work of separation (compared to pure Ni) suggesting a very strong propensity towards the brittle fracture of the GB.

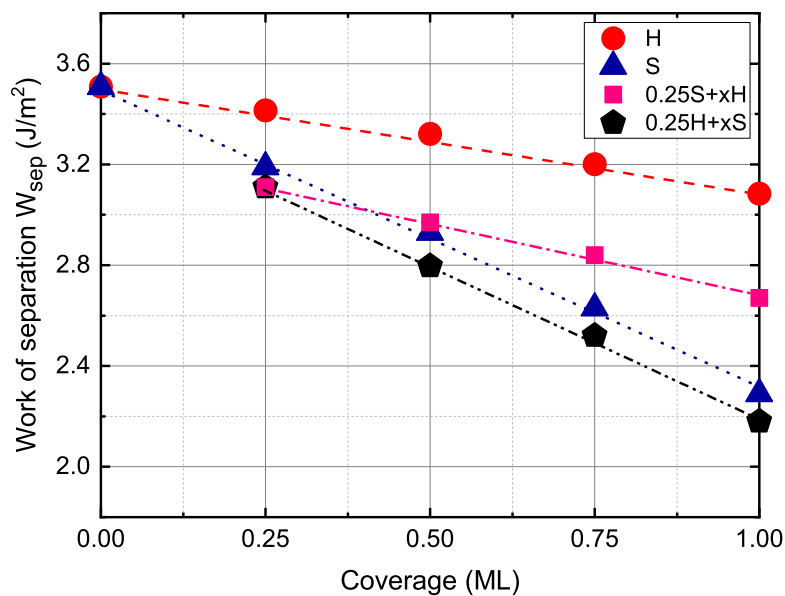


Fig. 7.11 Coverage change effect on the GB work of separation. The work of separation values for the coverage range of 0.25–1 ML H and S as well as the H-S co-segregated GB are calculated.

7.4 Discussion

7.4.1 GB effect on the micro mechanical behavior of the pure Ni bi-crystal

Adding GB to the microcantilever, rather than testing in a single crystal, changes the status of mechanical behaviour of the beam due to dissimilarity of the adjacent GBs. Different grain orientations lead to activation of different slip systems. As shown in a schematic diagram of Fig. 7.5, the high amount of slip traces revealed in the free standing grain forced the GB to deviate from its original straight form to curved or so called bulged shape in the upper part of the beam beneath the notch. It seems that the GB acts as a sink of dislocations and all the activated slip systems end up their pass to the GB. On the other hand, the chain of micro voids formed at the root of the blunted notch represents the commence of typical ductile fracture from the notch root. Accordingly, it seems that in the tested pure Ni bi-crystal system both the GB and notch are stress tolerated areas with a full plastic response.

Introducing H into the system, causes a distinct change in the mechanical response of the tested beams. Two clear differences can be distinguished between H-free and H-charged tested beams. Firstly, the surface slip traces are rarely occurred in the H-charged sample. H is known to confine the plasticity to the stress concentrated area at the crack tip [57, 65, 66, 42]. In the H-free case, dislocations which are formed during the plastic deformation can move easily far from the crack tip and reach to the free surface of the cantilever results in appearing the slip traces. However, accumulation of the H atoms at the crack tip can pin the dislocations shielding the plasticity from the crack tip and hence the plastic affected zone will be confined to a small area around the crack tip. Secondly, in contrast to the H free condition, the crack is initiated when the solute H was present in the material. However, the formed crack does not show a fully brittle characteristics and does not follow a straight line like a brittle crack. The presence of pyramids with triangular base in the fracture surface of the created crack from the top view (Fig. 7.5(b₃)) is the evidence that the crack propagation is accompanied by the plastic deformation. In addition, the L-D curves (Fig. 7.4(a)) also show not a sudden but gradual load drop during the deformation which is also an indication for the accompaniment of the plastic deformation beside the crack propagation. The plastic growth of the crack in the H environment, which is actually a mixture of plastic blunting and cracking. The concentration of H at the very crack tip lets the crack grow in a stable manner to a certain extent by micro cleavage and then the crack growth continues by plastic deformation with the concomitant of dislocations from the crack tip up to reaching a critical H concentration for the next micro cleavage growth.

The rough fracture surface in the H-charged sample, can be an evidence that the presented H amount in the fracture process zone was not enough to induce smooth fracture surface. Researching on the Ni single crystal, Vehoff reports that the fracture surface roughness of the sample increases as the H pressure in the testing chamber decreases at a constant temperature [67].

Interestingly, the presented GB in the bi-crystal system did not act as a crack nucleation area during the H charging test and crack propagation stage. It seems that in this case the GB does not act as a strong hydrogen trap. Generally, unlike many BCC metals, FCC metals have a relatively high solubility of H. In addition, knowing that the diffusivity of H is significantly lower than that of BCC metals, one can expect that H enrichment is rather low in FCC metals. The study of Pu and Ooi [68] on austenitic stainless steel by silver micro print technique proved this hypothesis that the GB in FCC alloys is not an important trap of H. In the review study of McMahon on steels [69], it is suggested that H can not induce IG cracking, unless other embrittling elements are presented in the alloy. However, some conflicting results have been published. Lassila and Birnbaum [70] reported a brittle fracture in presence of H. However, they also mentioned that as long as the H concentration is not more than the containing H in solid solution, no brittle fracture was observed. The reason behind this discrepancy in literature can also be related to the fact that the nature and also the misorientation of the GBs can be another factors that must be taken into account. It is reported that different types of GBs and also different misorientations tend to result in different amount of H solubility as well as diffusivity [71]. Oudriss et al [71] suggested that the diffusible H along random GBs may be the major cause of HE. However, in our case of the random grain boundary, the effect of hydrogen was not enough to induce complete brittle fracture. The same results were obtained by Tehrani and Curtin [72, 73]. Investigating pure Ni GB, they concluded that Ni GBs show no noticeable propensity for H to induce significant embrittlement and the presence of H creates no ductile-to-brittle transition. Another parameter should be considered for the analysis of the results is the amount of H which is charged into the sample. Obviously, the more H is present in the structure, the more brittleness is expected. Some of the contrasts between published literature about the effect of H on GB cracking are related to this factor. Vehoff and Rothe [67] stated that the room temperature equilibrium concentration of the H in the fracture process is the controlling factor for HE. The H concentration is controlled by the stress field of the plastic zone and also by the type and number of traps presented in this zone. According to their results, the intergranular cracking may be initiated and replaced by the transgranular one if the hydrogen activity is further enhanced by the cathodically charging during the test. The effect of H concentration will be discussed later in this paper in more detail.

7.4.2 GB S segregation effect on the micro mechanical behavior of the Ni bi-crystal

Sulfur is known as a harmful impurity that if segregates into the GB, would have a destructive impact on the mechanical properties of the GB and consequently the whole material. The observed intergranular crack initiation and propagation in NiS1 and NiS2 GBs (Fig. 7.6) comparing to the pure Ni beam which shows a ductile behaviour and notch blunting, is a clear indication for the detrimental effect of the segregated sulfur to the GB.

Several reasons have been proposed to show how the sulfur segregation changes the ductile behaviour of a GB to a brittle intergranular fracture. Changes in the electronic structure that weakens the Ni-Ni bonds in the GB reported by Messmer et al.[74]. Yamaguchi et al. [75] suggested the large GB expansion due to the dense S segregation can decrease the cohesive strength of the Ni GB up to one order of magnitude. It is stated that the S-S bonding formed in the GB which is calculated to have about 24% larger distance comparing to the Ni-Ni or Ni-S pairs leads to expansion in the surrounding Ni-Ni and Ni-S bonding. Consequently, this expansion in Ni-Ni or Ni-S bonds which are responsible for holding the GB can result in GB weakening and decohesion.

The DFT results provided in Fig. 7.11 and Table 7.3 indicate that S segregation has a great impact on the W_{sep} loss and also on the decrease in the GB energy. It also increases the propensity for intergranular fracture if one considers the R ratio calculated in 7.3. Here, we have performed an attempt to correlate the value of R with experimental observations of the fractured surfaces with and without H and S and concluded that the brittle fracture may occur in the materials under our investigation at $R < 0.8$ (see Sec. 7.2.3 for details). So the segregation of 0.5 ML of S or greater can lead to the brittle fracture. Although both NiS1 and NiS2 show a brittle crack at the GB, the strength of the GBs against crack propagation and therefore their response to the mechanical loading, presented in L-D curves, were different. Three reasons can be put forward to explain this difference:

a. Geometry effect The location of the GB beneath the notch and also the angle of the GB to the cantilever surface can affect the stress intensity and hence mechanical behaviour of the system. From the experimental point of view, it is important to have a perpendicular GB plane to the specimen surface and also to the load axis. This way, it can be assured that the activation of the slip bands, which are oriented nearly parallel to the GB plane, will be suppressed. Moreover, the tensile stress concentration will be the maximum within the GB plane assuming that the pure tensile stress dominates on the beam surface at the beginning of the test. Furthermore, the actual GB position relative to the notch should be taken into

account. In order to keep the consistency of stress distribution around the GB, the notch should be milled similar in all testing beams. Small deviations of the notch position relative to the GB plane can lead to redistribution of the stresses in the plastic deformation zone. In this work (see Sec. 7.2.1, we tried to reduce the effect of the aforementioned geometrical factors to a minimum. Comparing the notch and GB system in Fig. 7.6 it can be inferred that for both NiS1 and NiS2, the GB is positioned at a distance of several tens of nanometers aside from the notch root. Therefore, we assume that the the geometry has a minor effect on the presented results in comparison to other parameters.

b. Structural effect The type and also the misorientation of the GB has been reported to have an influence on the crack initiation and propagation. High energy random GBs are supposed to have weak resistance to the fracture whereas, low energy and low angle GBs are more resistant [76]. In a work on Molybdenum bi-crystals, values of fracture stress were observed to vary by a factor of six by changing the misorientation angle for the [110] misorientation axis [77]. So the different misorientation angle of the NiS1 GB compared to NiS2 can play a key role to show a nearly complete rupture of the GB to the surface. The incompatibility factor of the GB is also can play a role for the observed difference. Vehoff et al.[67] showed in their experimental work on S-doped GBs that the intergranular cracking susceptibility increases by adding an elastic-plastic incompatibility to the bi-crystal system. Having the constant amount of S in the GBs, they investigated the effect of incompatibility by switching from a symmetrical tilt GB to an asymmetrical boundary between hard and soft grains. The results confirmed that the high stress concentration associated with the incompatibility can be one of the controlling factors of the intergranular fracture. In our work, the NiS2 GB has a symmetric nature as the $\Sigma 5$ -type GBs, while NiS1 is an asymmetric GB. So again, this factor can be another parameter to enhance embrittling potency of the the NiS1 GB.

c. Chemical effect This factor is mutually related to the structural effect, as a different nature of the GB leads to different amount of S which can segregate. Generally, due to less ordered arrangement of the atoms at the GB plane usually associated with excess volume, high angle and high energy GBs are deemed to be more attractive for impurity segregation [1]. Based on table 7.1, it can be seen that high-angle GB1 with the misorientation angle of 54.2° has the largest S excess of 56.3 ng/cm^2 S, whereas the sulfur segregation at GB2 as a low-angle GB is 20.2 ng/cm^2 . The sigma 5 GB shows also a low amount of S segregation (27.3 ng/cm^2). This result agrees very well with previous studies wherein, it has been shown that the phosphorous segregation in Fe-C alloy was three times higher for high angle GBs rather than low angle ones [78]. So it is reasonable to consider that in bended cantilers the NiS1 Gb with high-angle

misorientation has the higher amount of segregated sulfur compared to the NiS2 as a sigma 5 GB. As a result, the different structure of NiS1 compared to NiS2 can be the reason for a larger S excess for NiS1 and consequently for a more pronounced embrittlement as it is confirmed from the L-D curve and fractographic investigations.

7.4.3 Decohesion enhancement of the GB hosting S and H

Solute H can downturn the ductility and change the fracture mode from transgranular to intergranular. However, H induced intergranular cracking needs a number of the factors such as sufficient level of H segregation and the stress distribution condition. Sulfur, as mentioned before, is also an impurity which is known to have a deleterious effect on the ductility and to induce IG cracking when it segregates to the GB. However, co-segregation of S alongside with H to the GB can consolidate their embrittling effect. Accordingly, based on the experimental results on sulfur doped bicrystals, in Both NiS1 and NiS2 GBs, the crack nucleates from the GB which demonstrates that the S segregation has a weakening effect on the GB strength. Adding H to the system by cathodic charging enhanced the embrittling effect by shifting the sudden load drop to approximately 2.5 and 1 μm displacement for NiS1 and NiS2 GBs, respectively. The incorporation of S and H to the polycrystalline nickel is reported before. By increasing the H pressure with switching from -0.3 V to -0.72 V cathodic potential, the critical sulfur coverage for TG to IG transition dropped from 0.2 ML to 0.05 ML [6]. However, It is not clear whether the co-segregation of H+S can have a synergistic effect on the mechanical response of the material. For iron it has been previously shown that the effect of S and H on the GB strength were independent and additive [79]. The DFT results also confirm this finding. Based on Fig. 7.11 the slope of line related to the work of separation for S (blue triangle line) does not change when 0.25 ML H is presented (black pentagon line). similar trend can be observed for the H work of separation with and without 0.25 ML S (red circle and pink square lines, respectively).

However it could be possible that the presence of S enhances the H ingress into the material due to the poisoning effect of this impurity to the H recombination reaction [80, 81], the fact which is not considered in DFT calculations. Preventing the recombination reaction by S can increase the local adsorption and enrichment of the H at the metal GBs. Likewise this phenomenon is reported For the Sb and Sn segregated GBs in Ni, as another recombination poisons [10]. It is suggested that the hydrogen preferentially ingressed into the nickel specimens in the proximity of grain boundary intersections with the free surface, due to the presence therein of Sb and Sn which act as hydrogen recombination poisons and stimulate the absorption of hydrogen by the metal. co-segregation of the Ni and H has also been investigated by molecular orbital model [82]. Forming a network of S-S bonds within the GB, according

to the this work, leads to an increase of the shear stress and simultaneously diminishes the cohesive strength of the GB. However, they suggested that by forming a network of bonds with incorporation of the third element like H, the shear strength will be raised, while it is not effecting the cohesive strength of the GB. However, it seems that this hypothesis is not fully in line with our results. As seen in Figs. 7.6 and 7.7, the shear bands are activated in all H-free conditions, even with the presence of high amount of S in the GBs. In the case of S doped NiS1 GB which is cracked in a fully decohesion manner, still the slip lines are observable especially on the free standing grain which is more favorable for dislocation movements. So it is hard to see any enhancement in shear stress for s-doped specimens. In contrast, adding H to the system was more effective to hinder the dislocation movements and lower amount of slip lines revealed on the surface even in the pure Ni sample. H is believed that can pin the dislocations and increase the shear stress of the material[42, 57, 66].

The DFT results also show that the solute S is more effective in decreasing the GB decohesion than H. According to the Table. 7.3, for example by adding 0.25 ML of S the Work of Separation decreased 9.19%, whereas 2.69% reduction has been calculated for the same segregation amount of H. the same behaviour of greater impact of S is also calculated for co-segregation of the S and H. In Fig. 7.11, by considering the constant value of 0.25ML S with increasing H and 0.25ML H with increasing S, Two lines have been sketched based on the Work of Seperation calculation. It can be seen that the slope of the S increasing line is more that the H increasing one showing the higher impact of S on GB decoration. To sum up the co-segregation effect of H+S in GB, it can be said that S was more influential on the decohesion reduction, while H was more effective on increasing the shear stress for plastic deformation. subsequently, the co-segregation of S+H can have a double side brittleness effect on both decoshesion and shear stress.

7.4.4 H concentration enhancement

As mentioned before, the H concentration is one of the main parameters controlling the mechanical response of the material. Therefore, to investigate the effect of H concentration enhancement on the GB embrittlement, 0.002 M $Na_2S_2O_4$ as the hydrogen recombination poison, was added to the charging glycerol based solution for testing beams containing NiS2 GB.

Comparing L-D curves in Fig. 7.4 for NiS1 and NiS2 GBs in H-free condition, it can be inferred that NiS2 GB shows more ductility compared to NiS1. However, for 2 h of H charging, the presence of poison for bending the beam containing NiS2 GB causes more ductility loss in comparison with NiS1 one which is tested without any poison. As discussed in 7.4.2 section, NiS2 GB possesses lower misorientation angle and probably the lower amount of S compared

to NiS1 GB. So the NiS2 is less prone to cracking. However, the higher content of H obtained by adding poison into the solution, can overcome the structural and chemical effect in the way that the NiS2 GB fails easier and shows enhanced embrittlement comparing to NiS1 with the same H charging time but no poison. In accordance to our results, it is reported that by increasing the cathodic potential which would enhance the H concentration in the Ni GB, the critical S concentration to cause 50 %IG fracture decreases [83]. By applying -0.72V (SCE) cathodic potential the critical S segregation concentration drops to about ~ 2 at.%, whereas in the potential of in -0.3V (SCE) the critical S segregation concentration was 6.5at.%. Additionally, Lassia and birnbaum [70] reported a change from ductile fracture to a mixed brittle-ductile and complete IG fracture by increasing the H content from 0 appm to 60 and 600 appm, respectively for a specimen with sulfur concentration of 0.1 S/Ni.

Low diffusivity, coupled with high solubility in Ni results in a high hydrogen concentration gradient near to the surface. This gradient may result in some structural effects close to the sample surface and accordingly large change in the mechanical properties of the material. Changes in the flow stress of the H-charged Ni samples is one of these effects. As shown in Fig. 7.12, continuing the in situ testing in the poison containing solution, revealed a hardening effect for the beams tested after 3h of charging. While the sudden load drop for both 3h and 2h charged samples happens in the same displacement, for 3h charging condition the beam shows about 20% increase in the maximum tolerated load. After 3h of charging in poisoned solution, in situ charging was stopped, the samples were taken out from the solution, rinsed with distilled water and later with ethanol which followed keeping them in desiccator. Then, the beams were bent after 2, 4 and 17 h. For 2h of being in air (H charged 3h + air 2h), the same L-D curve as 3h in situ charging is achieved. Giving further hours to the sample in H-free environment turns over the ductility of the tested beam up to 50% after 17 hours of being in air. The observed hardening effect was persistent in all L-D curves obtained after 3h of charging.

The observed increase in the maximum tolerated force can be interpreted as the hardening effect caused by H- dislocation interaction. several researches have reported the hardening effect during H charging in both BCC [84] and FCC materials. As an example, Kimura and birnbaum [85] observed hardening effect when they charged the Ni samples in a solution containing H recombination poison at a current density of 0.8 mA/cm². Their reported current density is in a comparable range to the one used in our experiment. However there is a significant difference in the obtained results. The hardening effect reported in their work was reversible and the flow stress turned back to that recorded in the absence of H, when the cathodic potential was removed. In contrast, the maximum tolerated load enhancement in the L-D curves shown in Fig. 7.12 was persistent and did not show any decrease even after 17 h of keeping the sample

in air. Hence, it seems that the hardening hypothesis is unlikely to be the reason behind our results.

The hydride formation can be another possibility for the observed enhancement in the maximum tolerated force. It is reported that the hardening effect, caused by nickel hydride formation, is irreversible even after aging for several hours[85]. Hydride is a brittle phase and acts as a barrier to dislocation ingress from the surface. Despite of the thermodynamically unstable nature of Ni-H in room temperature, it is well documented that if the high activity of H atom presents, the hydride formation would be possible [86]. The presence of poison with longer time of H charging together with the low diffusivity and high solubility of Ni FCC crystal, lead to accumulation of high amount of H beneath the metal surface. The formation of blisters can be an evidence for the high fugacity of the H presented in the sample's subsurface which produce gaseous H at internal pores. After the the 3 hour of cathodic charging experiment with a solution contained H recombination poison some blister with the well known bumpiness shape was observed in the surface of the sample. Fig. 7.14 illustrates the mentioned blister shaped roughness. It worth to note that, comparing the sample surface condition before and after H charging, it is recognizable that the concentration of these blisters are higher in some grains comparing to others. This is consistent with the results reported for a H-charged Ni polycrystal where the grain with lower surface energy, such a (111), were more prone for blistering comparing to those have higher surface energy like (100) or (110) oriented grains [87]. During the out gassing, although the hydride layer reverts to Ni due to its unstable nature at room temperature [85, 88], the remained high surface dislocation density causes the residual increase in the flow curve[85].

Grain boundary opening By examining the surface condition of the metal after H charging, it was observed that some surface GBs opened while they were just under hydrogen charging in the solution without any external applied force. The cross sectional view of one of these opened GBs in Fig. 7.15(b) reveals 5 μm crack opening depth in the GB. This result ties well with previous studies wherein the GB opening was also observed for Ni-S-H system. Two reasons for this phenomenon can be proposed. Firstly, it is well-known that the presence of H, especially in high concentration on the metal surface can produce a lattice expansion in the material[89, 90]. As a result of the lattice expansion and producing tensile stress, some cracks can be initiated from the weak points of the material. The GB areas with high amount of segregated S which has a low work of separation can be a vulnerable areas to form an internally cracks. So the GBs with high amount of segregated S will be opened on the metal surface due to expansion induced of H charging. The formation of Ni hydride can also be another reason to induce internal stresses in the material. It is reported that the lattice constant of the Ni hydride

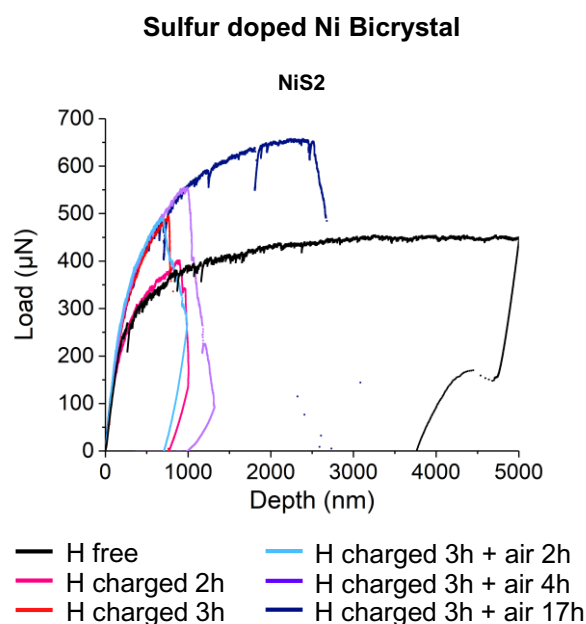


Fig. 7.12 Load-displacement curves of the sulfur doped (grain boundary NiS2 in table 7.2) bi-crystal beams tested with hydrogen free, in situ electrochemical hydrogen charging and post charging in air conditions. The hydrogen charging electrolyte contained 0.002 M $Na_2S_2O_4$ as the hydrogen recombination poison.

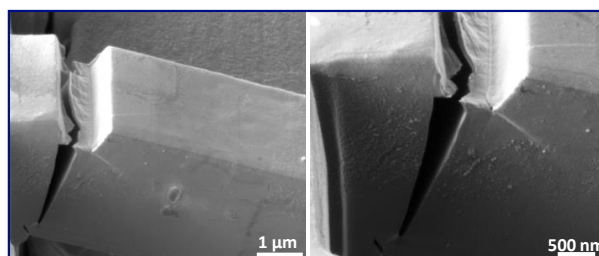


Fig. 7.13 Post deformation secondary electron images from the side view of the bi-crystal grain with grain boundary NiS2 in table 7.2 bent after (a₁ and a₂) 3 h hydrogen charging and (b₁ and b₂) 17 h kept in air after 3 h hydrogen charging.

is about 6% larger than the lattice constant of pure nickel and hence it will cause a significant tensile stress gradient at the surface of the specimen below the hydride[85].

While some of the GBs showed an IG opening, there are cases where the GB is not opened as seen in Fig. 7.15(c). Both the chemical and structural character of the GB can cause the observed difference. The EBSD results of the presented area in Fig. 7.15(d) reveals that the GBs with high angle misorientation and also $\Sigma 27a$ and $\Sigma 9$ Gbs has been opened, while sigma 3 ones remained intact. based on previous discussions about the GB structure and its relation to S segregation it is reasonable to assume that the high misorientation GBs possesses higher

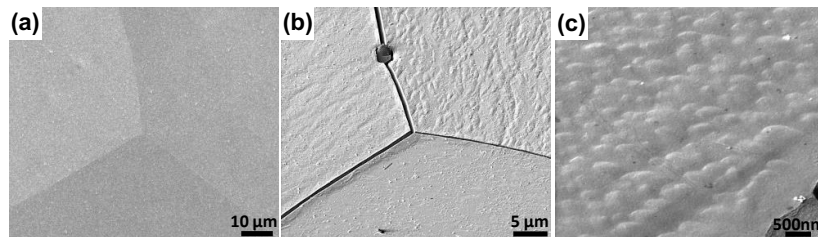


Fig. 7.14 Scanning electron microscopy images from the grain boundary sulfur doped sample (a) before and (b and c) after hydrogen charging with a glycerol based electrolyte containing 0.002 M $Na_2S_2O_4$.

amount of sulfur and then $\Sigma 3$ GBs have the lowest segregated S. Different studies have shown that the $\Sigma 3$ GBs are not susceptible for impurity segregation [91]. It is also reported that H does not affect the decohesion of the sigma 3 GBs very much [92]. As a result, the GBs with higher misorientation and hence higher amount of S can be opened by the surface stress induced by heavy charging of the H, while $\Sigma 3$ and low-angle GBs remain affected.

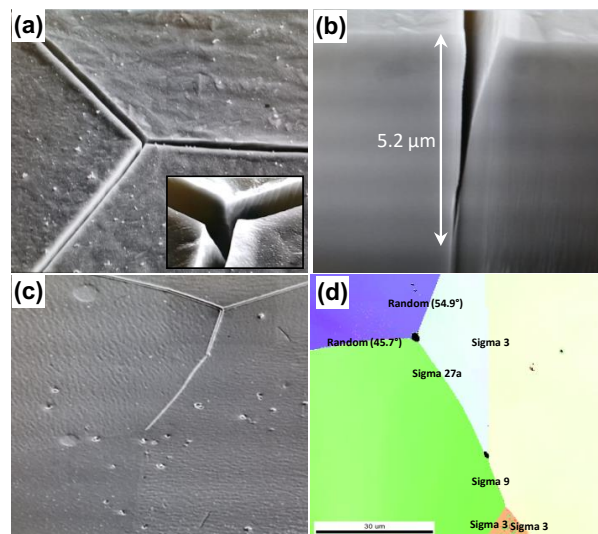


Fig. 7.15 (a) Scanning electron microscopy image of grain boundary opening in the sulfur doped sample after hydrogen charging with a glycerol based electrolyte containing 0.002 M $Na_2S_2O_4$. (b) cross sectional view of an opened GB. (c) Surface area containing both opened and non-opened boundaries. (d) EBSD map of the corresponding area in (c).

7.5 Conclusions

Current work deals with how the segregation of S and H affect the mechanical properties of a single GB. In-situ micro cantilever bending tests were utilized to investigate the mechanical

response of the GB. DFT calculations were also used to study the atomic interaction of the S and H atoms with the GB. Cantilever bending in pure nickel samples without S segregation represented a ductile behaviour accompanied by many activated slip lines on the surface. While testing pure nickel in H charged condition, the crack has initiated from the notch area and less activated slip lines has been observed. However, in this case the crack propagates by plastic behaviour and does not follow the GB, segregation of S in GB makes to form a significant crack after the bending test, and the crack revealed brittle appearance and propagated completely in the GB path. Introducing the H made the condition more detrimental and caused a sooner sudden drop in Load-Displacement curves compared to H-free ones.

Based on the DFT results, it has been shown that solute S can have more detrimental effect on the GB cohesion than H. Furthermore, the co-segregation of the S and H and its effect on intergranular fracture has been studied by DFT calculations and discussed in the paper. The kinetics of S and H atoms at Ni GB have been calculated using the DFT segregation energies and compared to experiments measurements. It has also been shown that depends on the GB structure and the amount of S segregation, the severity of the crack propagation can be different. Moreover, it has been indicated from EBSD maps analysis that random high-angle GBs showed more susceptibility to brittle behaviour while low-angle and Σ 3 GBs less affected by the H charging.

References

- [1] P. Lejček, Grain Boundary Segregation in Metals, Springer Berlin Heidelberg, Berlin, 2010.
- [2] P. Lejček, M. Šob, V. Paidar, Prog. Mater. Sci. 87 (2017) 83–139.
- [3] S. Mahalingam, P. E. J. Flewitt, J. F. Knott, Mater. Sci. Eng.: A 564 (2013) 342–350.
- [4] M. Lozinsky, G. Volkogon, N. Pertsovsky, Russ. Metall. 5 (1967) 65–72.
- [5] A. Larere, M. Guttman, P. Dumoulin, C. Roques-Carmes, Acta Metall. 30 (1982) 685–693.
- [6] S. M. Bruemmer, R. H. Jones, M. T. Thomas, D. R. Baer, Metall. Trans. A 14 (1983) 223–232.
- [7] W. T. Geng, A. J. Freeman, R. Wu, C. B. Geller, J. E. Reynolds, Phys. Rev. B 60 (1999) 7149–7155.
- [8] V. Razumovskiy, A. Lozovoi, I. Razumovskii, Acta Mater. 82 (2015) 369 – 377.
- [9] R. H. Jones, S. M. Bruemmer, M. T. Thomas, D. R. Baer, Metall. Trans. A 14 (1983) 1729–1736.
- [10] R. M. Latanision, H. Opperhauser, Metall. Trans. 5 (1974) 483–492.

- [11] K. M. Bertsch, S. Wang, A. Nagao, I. M. Robertson, *Mater. Sci. Eng. A* 760 (2019) 58–67.
- [12] H. Vehoff, C. Laird, D. Duquette, *Acta Metall.* 35 (1987) 2877 – 2886.
- [13] D. Di Maio, S. Roberts, *J. Mater. Res.* 20 (2005) 299–302.
- [14] J. Ast, M. Ghidelli, K. Durst, M. Göken, M. Sebastiani, A. M. Korsunsky, *Mater. Des.* 173 (2019) 107762.
- [15] H. Dugdale, D. E. J. Armstrong, E. Tarleton, S. G. Roberts, S. Lozano-Perez, *Acta Mater.* 61 (2013) 4707–4713.
- [16] A. Stratulat, D. E. J. Armstrong, S. G. Roberts, *Corros. Sci.* 104 (2016) 9–16.
- [17] M. Yamaguchi, M. Shiga, H. Kaburaki, *J. Phys.: Condens. Matter* 16 (2004) 3933.
- [18] M. Yamaguchi, M. Shiga, H. Kaburaki, *J. Phys. Soc. Jpn.* 73 (2004) 441–449.
- [19] D. D. Stefano, M. Mrovec, C. Elsässer, *Acta Mater.* 98 (2015) 306 – 312.
- [20] S. He, W. Ecker, R. Pippan, V. I. Razumovskiy, *Comput. Mater. Sci.* 167 (2019) 100 – 110.
- [21] B. He, W. Xiao, W. Hao, Z. Tian, *J. Nucl. Mater.* 441 (2013) 301 – 305.
- [22] M. Yuasa, M. Hakamada, Y. Chino, M. Mabuchi, *ISIJ Int.* 55 (2015) 1131–1134.
- [23] D. A. Aksyonov, T. Hickel, J. Neugebauer, A. G. Lipnitskii, *J. Phys.: Condens. Matter.* 28 (2016) 385001.
- [24] D. Scheiber, L. Romaner, R. Pippan, P. Puschnig, *Phys. Rev. Mater.* 2 (2018) 093609.
- [25] M. Yamaguchi, M. Shiga, H. Kaburaki, *Science* 307 (2005) 393–397.
- [26] M. Yamaguchi, M. Shiga, H. Kaburaki, *Science* 309 (2005) 1677–1677.
- [27] W. T. Geng, J.-S. Wang, G. B. Olson, *Science* 309 (2005) 1677–1677.
- [28] G. Schusteritsch, E. Kaxiras, *Modell. Simul. Mater. Sci. Eng.* 20 (2012) 065007.
- [29] D. Raabe, M. Herbig, S. Sandlöbes, Y. Li, D. Tytko, M. Kuzmina, D. Ponge, P. P. Choi, *Curr. Opin. Solid State Mater.* 18 (2014) 253–261.
- [30] S. Bechtle, M. Kumar, B. P. Somerday, M. E. Launey, R. O. Ritchie, *Acta Mater.* 57 (2009) 4148–4157.
- [31] T. Watanabe, S. Tsurekawa, *Acta Mater.* 47 (1999) 4171–4185.
- [32] E. M. Lehigh, G. Palumbo, P. Lin, *Metall. Mater. Trans. A* 29 (1998) 3069–3079.
- [33] J. R. Rice, R. Thomson, *Philos. Mag. A* 29 (1974) 73–97.
- [34] J. R. Rice, J.-S. Wang, *Mater. Sci. Eng. A* 107 (1989) 23 – 40.
- [35] D. McLean, *Grain Boundaries in Metals*, Clarendon Press, Oxford, 1957.
- [36] D. Scheiber, L. Romaner, F. Fischer, J. Svoboda, *Scr. Mater.* 150 (2018) 110–114.
- [37] D. Scheiber, T. Jechtl, J. Svoboda, F. Fischer, L. Romaner, *Acta Mater.* (2019).
- [38] N. Kheradmand, H. Vehoff, A. Barnoush, *Acta Mater.* 61 (2013) 7454–7465.
- [39] F. Christien, P. Risch, *Ultramicroscopy* 170 (2016) 107 – 112.
- [40] A. Barnoush, H. Vehoff, *Acta Mater.* 58 (2010) 5274 – 5285.

- [41] A. Barnoush, H. Vehoff, *Corros. Sci.* 50 (2008) 259 – 267.
- [42] T. Hajilou, Y. Deng, B. R. Rogne, N. Kheradmand, A. Barnoush, *Scr. Mater.* 132 (2017) 17 – 21.
- [43] T. Hajilou, M. S. Hope, A. H. Zavieh, N. Kheradmand, R. Johnsen, A. Barnoush, *Int. J. Hydrog. Energy* 43 (2018) 12516 – 12529.
- [44] P. E. Blöchl, *Phys. Rev. B* 50 (1994) 17953.
- [45] G. Kresse, D. Joubert, *Phys. Rev. B* 59 (1999) 1758.
- [46] G. Kresse, J. Hafner, *Phys. Rev. B* 48 (1993) 13115–13118.
- [47] G. Kresse, J. Furthmüller, *Comput. Mater. Sci.* 6 (1996) 15 – 50.
- [48] J. P. Perdew, K. Burke, M. Ernzerhof, *Phys. Rev. Lett.* 77 (1996) 3865–3868.
- [49] H. J. Monkhorst, J. D. Pack, *Phys. Rev. B* 13 (1976) 5188–5192.
- [50] D. Kandaskalov, D. Monceau, C. Mijoule, D. Connétable, *Surf. Sci.* 617 (2013) 15 – 21.
- [51] D. Connétable, É. Andrieu, D. Monceau, *Comput. Mater. Sci.* 101 (2015) 77–87.
- [52] R. Nazarov, T. Hickel, J. Neugebauer, *Phys. Rev. B* 89 (2014) 144108.
- [53] L. Wang, H. Bei, T. Li, Y. Gao, E. George, T. Nieh, *Scr. Mater.* 65 (2011) 179 – 182.
- [54] A. P. Sutton, R. W. Balluffi, A. Sutton, *Interfaces in crystalline materials*, Clarendon Press Oxford, 1995.
- [55] D. Scheiber, R. Pippan, P. Puschnig, L. Romaner, *Model. Simul. Mater. Sci. Eng.* 24 (2016) 035013.
- [56] A. Pineau, A. Benzerga, T. Pardoen, *Acta Mater.* 107 (2016) 424 – 483.
- [57] D. Wan, Y. Deng, J. I. H. Meling, A. Alvaro, A. Barnoush, *Acta Mater.* 170 (2019) 87 – 99.
- [58] M. Yamaguchi, M. Shiga, H. Kaburaki, *Mater. Trans.* 47 (2006) 2682–2689.
- [59] A. Winkler, K. D. Rendulic, in: M. Grasserbauer, M. K. Zacherl (Eds.), *Zehntes Kolloquium über metallkundliche Analyse*, Springer Vienna, Vienna, 1981, pp. 321–327.
- [60] A. Alvaro, I. T. Jensen, N. Kheradmand, O. Løvvik, V. Olden, *Int. J. Hydrog. Energy* 40 (2015) 16892 – 16900.
- [61] I. J. T. Jensen, V. Olden, O. M. Løvvik, *Metall. Mater. Trans. A* 50 (2019) 451–456.
- [62] M. Allart, F. Christien, R. L. Gall, P. Nowakowski, C. Grovenor, *Scr. Mater.* 68 (2013) 793 – 796.
- [63] H. Mehrer, N. Stolica, *Diffusion in Solid Metals and Alloys*, volume 26 of *Landolt-Börnstein - Group III Condensed Matter*, Springer-Verlag, Berlin/Heidelberg, 1990.
- [64] M. Hill, E. Johnson, *Acta Metall.* 3 (1955) 566–571.
- [65] Y. Deng, A. Barnoush, *Acta Mater.* 142 (2018) 236 – 247.
- [66] B. R. S. Rogne, N. Kheradmand, Y. Deng, A. Barnoush, *Acta Mater.* 144 (2018) 257–268.

- [67] H. Vehoff, W. Rothe, in: *Perspectives in Hydrogen in Metals*, Elsevier, 1986, pp. 647–659.
- [68] S. Pu, S. Ooi, *Mater. Sci. Eng. A* (2019) 138059.
- [69] C. McMahon Jr, *Eng. Fract. Mech.* 68 (2001) 773–788.
- [70] D. Lassila, H. Birnbaum, *Acta Metall.* 34 (1986) 1237–1243.
- [71] A. Oudriss, J. Creus, J. Bouhattate, E. Conforto, C. Berziou, C. Savall, X. Feaugas, *Acta Mater.* 60 (2012) 6814–6828.
- [72] A. Tehranchi, W. Curtin, *J. Mech. Phys. Solids* 101 (2017) 150–165.
- [73] A. Metsue, A. Oudriss, X. Feaugas, *J. Alloys Compd.* 656 (2016) 555–567.
- [74] R. Messmer, C. Briant, *Acta Metall.* 30 (1982) 457–467.
- [75] M. Yamaguchi, M. Shiga, H. Kaburaki, *Science* 307 (2005) 393–397.
- [76] T. Watanabe, *Mater. Sci. Eng. A* 176 (1994) 39–49.
- [77] S. Tsurekawa, T. Tanaka, H. Yoshinaga, *Mater. Sci. Eng. A* 176 (1994) 341–348.
- [78] A. Akhatova, F. Christien, V. Barnier, B. Radiguet, E. Cadel, F. Cuvilly, P. Pareige, *Appl. Surf. Sci.* 463 (2019) 203–210.
- [79] K. Shin, M. Meshii, in: *Perspectives in Hydrogen in Metals*, Elsevier, 1986, pp. 693–700.
- [80] H. Jarmolowicz, M. Smialowski, *J. Catal.* 1 (1962) 165–170.
- [81] M. Abd Elhamid, B. Ateya, K. Weil, H. Pickering, *Corrosion* 57 (2001) 428–432.
- [82] M. Eberhart, K. Johnson, R. Latanision, *Acta Metall.* 32 (1984) 955–959.
- [83] J. K. Heuer, P. R. Okamoto, N. Q. Lam, J. F. Stubbins, *Appl. Phys. Lett.* 76 (2000) 3403–3405.
- [84] S. Asano, R. Otsuka, *Scr. Metall.* 10 (1976) 1015–1020.
- [85] A. Kimura, H. Birnbaum, *Acta Metall.* 35 (1987) 1077–1088.
- [86] E. Wollan, J. Cable, W. Koehler, *J. Phys. Chem. Solids* 24 (1963) 1141–1143.
- [87] M. Zamanzade, C. Müller, J. R. Velayarce, C. Motz, *Int. J. Hydrog. Energy* 44 (2019) 7706–7714.
- [88] E. Lunarska-Borowiecka, N. F. Fiore, *Metall. Trans. A* 12 (1981) 101–107.
- [89] H. Peisl, *Lattice strains due to hydrogen in metals*, Springer Berlin Heidelberg, Berlin, Heidelberg, 1978.
- [90] G. Thomas, W. Drotning, *Metall. Trans. A* 14 (1983) 1545–1548.
- [91] S. Kobayashi, S. Tsurekawa, T. Watanabe, G. Palumbo, *Scr. Mater.* 62 (2010) 294–297.
- [92] M. Rajagopalan, M. Tschopp, K. Solanki, *JOM* 66 (2014) 129–138.

Chapter 8

A theoretical insight into hydrogen clustering at defects in Ni

8.1 Introduction

Hydrogen embrittlement (HE) is a latent problem for many structural materials including Ni and its alloys [1, 2]. The atomic-scale mechanisms of HE are still debated but most of them are often related to H trapping and accumulation in the lattice of the material or more specifically at various defects that are often referred to as traps [3–7]. A possibility of H cluster formation at structural traps in Ni, such as vacancies and grain boundaries (GBs), has been intensively studied in a number of recent density functional theory (DFT) papers [8–18] with a focus on its possible impact on the theories and mechanisms of HE. In this work, we perform an attempt to evaluate the relevance of possible H clustering at vacancies and GBs in Ni to the problem of HE in Ni by assessing the integrity of H clusters reported in literature at temperatures above 0 K. As a method of study, we have chosen a combined DFT calculations and embedded atom method (EAM) approaches that would allow us to account for both chemistry and temperature effects within the framework of molecular dynamics (MD) simulations.

8.2 Computational details

8.2.1 Density functional theory calculations

The spin polarized DFT calculations have been performed using the projector-augmented-wave (PAW) [19] method as implemented in the Vienna *ab initio* simulation package (VASP) [20, 21]. The Perdew-Burke-Ernzerhof (PBE) form of generalized gradient approximation (GGA) has

been employed for the exchange-correlation functional [22]. The plane-wave basis cutoff energy has been set to 400 eV. The convergence criteria of self-consistent calculations have been set to 10^{-5} eV/cell for the total energy, and that to 9×10^{-3} eV/Å for the atomic forces. The integration over the Brillouin zone has been done using the Monkhorst-Pack mesh [23], the k -meshes of $4 \times 4 \times 4$, $6 \times 6 \times 6$, and $4 \times 4 \times 1$ k -points have been used in the cases of the fcc-Ni $[3 \times 3 \times 3]$ supercell, the fcc-Ni $[2 \times 2 \times 2]$ supercell, and the $\Sigma 5$ GB slab calculations respectively. The 0 K equilibrium lattice parameters have been fixed to 3.515 Å and 3.524 Å for the DFT and EAM calculations respectively, which agree with the experimental zero Kelvin value for Ni of 3.515 Å [24].

8.2.2 Semiempirical calculations

The EAM simulations have been performed by using the Large-Scale Atomic/Molecular Massively Parallel Simulator (LAMMPS) molecular dynamics simulator [25]. The EAM potential for Ni-H system has been taken from Refs. [26–29]. The energy minimization of the structure has been carried out using the conjugate gradient algorithm with energy tolerance of 10^{-15} eV and force tolerance of 10^{-15} eV/Å respectively. The optimal Ni supercell configurations with different amounts of H are determined after minimizing and relaxing the Ni-H system at 0 K. Moreover, the MD simulations of the energetically most favorable hydrogen clusters bound to the structural defects have been performed in the isothermal-isobaric (NPT) ensemble within temperature interval of 150-375 K sampled every 25 K and assuming zero-pressure. For each temperature, a $0.5 \mu\text{s}$ trajectory has been generated with a time-step of 1 fs. To monitor the hydrogen cluster integrity, the mean-square displacement (MSD) of hydrogen atoms has been computed.

8.2.3 Computational models

The vacancy in the bulk and GBs has been modeled using supercells shown in Fig. 8.1 (a), (b), and (c) respectively. The bulk of Ni has been represented by a 31-atom fcc-Ni $[2 \times 2 \times 2]$ supercell with a vacancy located at the center of the cube (see Fig. 8.1(a)). The results of supercell size test show that already a $[2 \times 2 \times 2]$ supercell is sufficient to achieve a precision of 0.05 eV for the vacancy formation energy. The $\Sigma 5(012)$ [30] and $\Sigma 3(111)$ [17] coincidence site lattice (CSL) symmetric tilt GBs have been modeled using 76-atom [30] and 96-atom [17] shown in Fig. 8.1 (b)-(c) in all DFT and EAM calculations at 0 K. For the EAM simulations of MSD at finite temperature, the bulk of Ni has been modeled by a 863-atom fcc-Ni $[6 \times 6 \times 6]$ supercell with one vacancy and 6 H atoms, the $\Sigma 5(012)$ and $\Sigma 3(111)$ have been constructed by

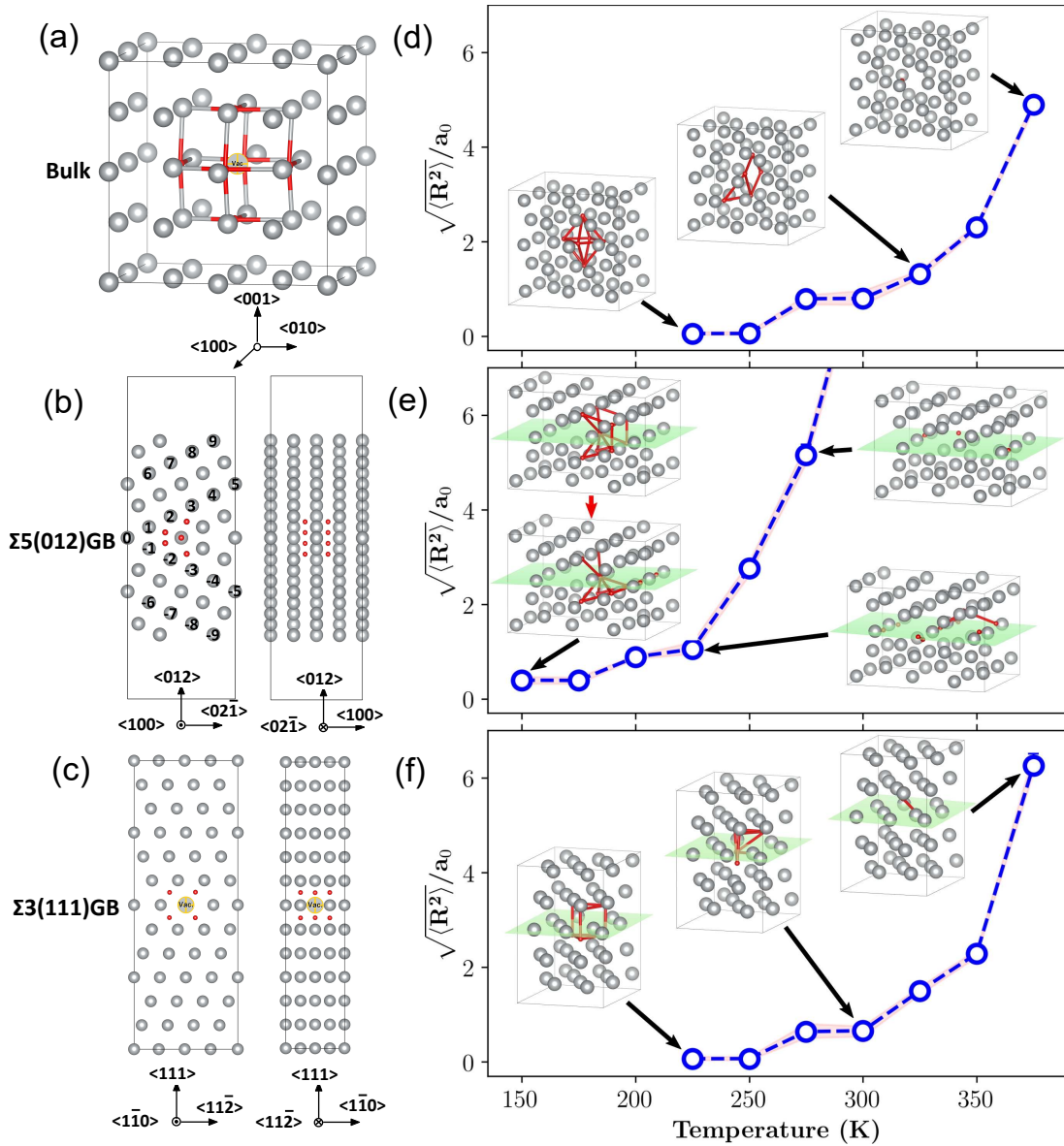


Fig. 8.1 Schematics of the lowest binding energy H clusters and MSD of H atoms from the initial positions at 0 K. (a) A 6-atom hydrogen (red spheres) cluster surrounding a vacancy in Ni ; (b) A 9-atom hydrogen cluster at the void of $\Sigma 5(012)$ GB in Ni; (c) A 6-atom hydrogen cluster at the vacancy of $\Sigma 3(111)$ GB in Ni [17]. (d)-(f) show the MSD of H atoms at traps illustrated in (a)-(c), respectively. The structures depicted in the insets correspond to the geometries within the control volume around the cluster after the MD run.

replicating the 160-atom $\Sigma 5(012)$ and 96-atom $\Sigma 3(111)$ CSL models, resulting in [1440 Ni + 9 H] atoms and [1439 Ni+ 6 H] atoms with one vacancy, respectively.

In this work, the binding energy is defined to study the stability of a H cluster as following:

$$E_b^{\delta,\alpha} = E_{\text{tot}}^{\delta,\alpha} - E_{\text{tot}}^{\alpha} + n(E_{\text{bulk}}^{\text{Ni}} - E_{\text{bulk}}^{\delta}), \quad (8.1)$$

here $E_{\text{tot}}^{\delta,\alpha}$ is the total energy of the supercell containing a structural defect α (a vacancy or GB) and the binding defects δ (H atom or vacancy), while E_{tot}^{α} is the total energy of the supercell with a structural defect α . E_{bulk}^{δ} and $E_{\text{bulk}}^{\text{Ni}}$ are the total energies of the fcc-Ni $[3 \times 3 \times 3]$ supercell with and without a point defect δ , respectively, n is the number of trapped H atoms. When $n=1$, the binding energy is equivalent to the segregation energy [31]: $E_{\text{seg}}^{\delta,\alpha} = E_{\text{tot}}^{\delta,\alpha} - E_{\text{tot}}^{\alpha} + E_{\text{bulk}}^{\text{Ni}} - E_{\text{bulk}}^{\delta}$, which is used to investigate the H atom and the vacancy segregation energy profiles at the GB in Ni. In this study, we adopt the following sign convention: binding (or segregation) energy is negative if the impurities tend to be attracted to the GB/vacancy.

8.3 Results and discussions

8.3.1 Segregation of H to the defects of Ni

As a first step in our investigation, we focus on the segregation of a H atom and a vacancy to the $\Sigma 5(012)$ GB as well as the segregation of a H atom to the vacancy of the bulk of Ni by DFT and EAM calculations. In Fig. 8.2 (a) and (b), we show that a H atom prefers to segregate to the first 3 layers (0, +/-1, and +/-2 in Fig. 8.1(b)) of the GB, meaning that the GB region is a strong trap for H atoms. At the same time, DFT and EAM calculations predict the segregation energy of -0.90 eV and -1.37 eV respectively for a vacancy located at the neighboring layer of the GB layer, *i.e.*, the 1 or -1 layers in Fig. 8.1 (b), which indicates a possibility of H trapping by a vacancy at the GB of Ni [17].

In addition to the GB segregation energy profiles, we have calculated the binding energies between a vacancy and the H atoms located at neighboring TSs and OSs in the bulk of Ni. The results and corresponding neighboring TS and OS positions are shown in Fig. 8.2 (c) and (d) respectively. Fig. 8.2 (c) shows that the lowest binding energy of H to the vacancy is achieved for the 1NN OS configuration, amounting to -0.25 eV and -0.20 eV in the DFT and EAM calculations, respectively. The 1NN TS configuration is somewhat less favorable, yielding the binding energy of -0.22 eV and -0.09 eV in DFT and EAM, respectively, which confirms a stronger trapping for H to the OSs around the vacancy and a tendency to form a H-vacancy complex in Ni. The binding energy of a H atom to the vacancy is in good agreement with DFT literature data of $-0.22 \sim -0.25$ eV/atom [10–13, 15], however, the DFT calculated binding energy of H-vacancy is much higher than experimental values of $-0.24 \sim -0.57$ eV for H-vacancy [34–38] possibly due to the fact that the binding energy of multiple-vacancy

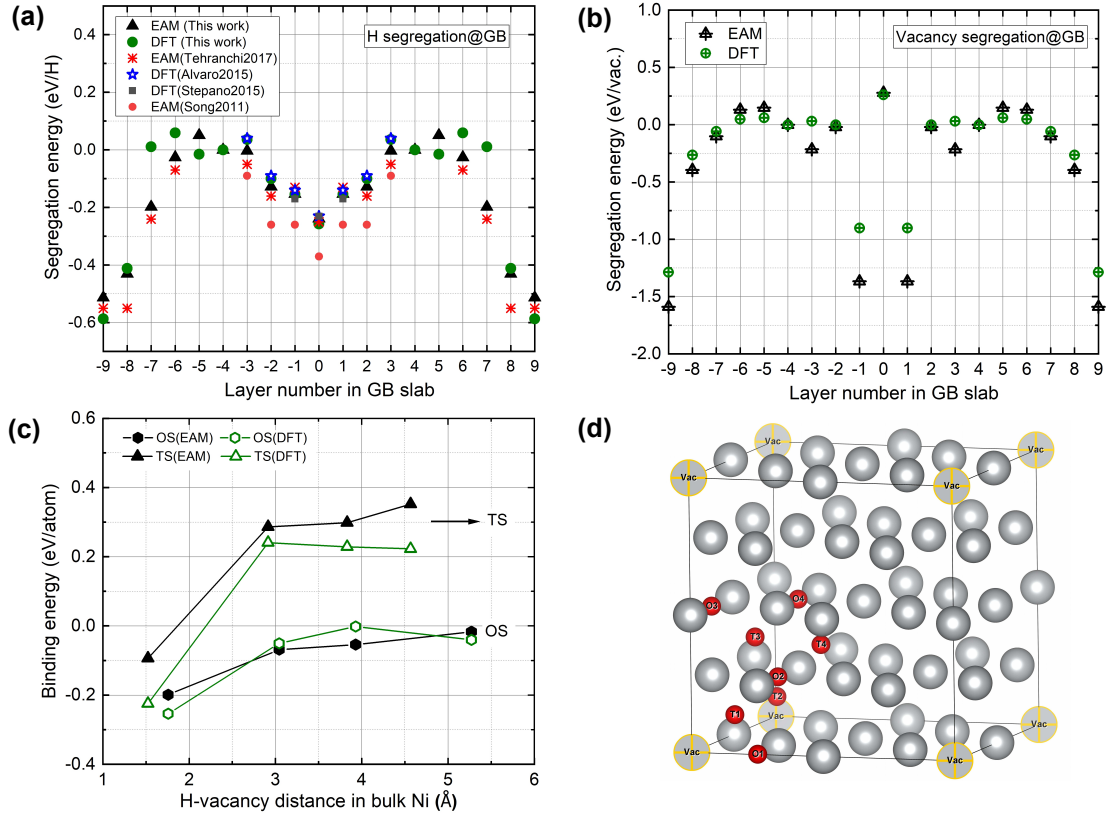


Fig. 8.2 The segregation energies of H and vacancy to the Ni $\Sigma 5$ (012) GB as well as the H-vacancy binding energy as a function of H-vacancy distance in the bulk Ni from DFT and EAM calculations. The layer number indexes in (a) and (b) correspond to the schematics in Fig. 8.1 (b). (a) Calculated H segregation energy in the Ni $\Sigma 5$ (012) GB with comparison from literature [29, 32, 33, 28]; (b) Vacancy segregation energy in the Ni $\Sigma 5$ (012) GB; (c) H binding energy profile to a vacancy of Ni; (d) The schematics of a Ni supercell with a vacancy and its four nearest neighbouring octahedral sites (OS, labelled by O1–O4) and four nearest neighbouring tetrahedral sites (TS, labelled by T1–T4).

defect was measured in the experiment [35]. We also show a comparison to the literature for the segregation energy profiles of H atom and the vacancy at the $\Sigma 5$ (012) GB and at the (012) free surface (FS) which are in perfect agreement with the literature data [28, 29, 32, 33]. These results make us confident that the selected EAM potential captures well the structural and the chemical aspects of the Ni-H system with a GB.

8.3.2 H-vacancy cluster in bulk Ni

Let us now take a look at hydrogen clustering at a vacancy in the bulk of Ni. Following conclusion from above as well as the methodology from Ref. [11], the H atoms have been

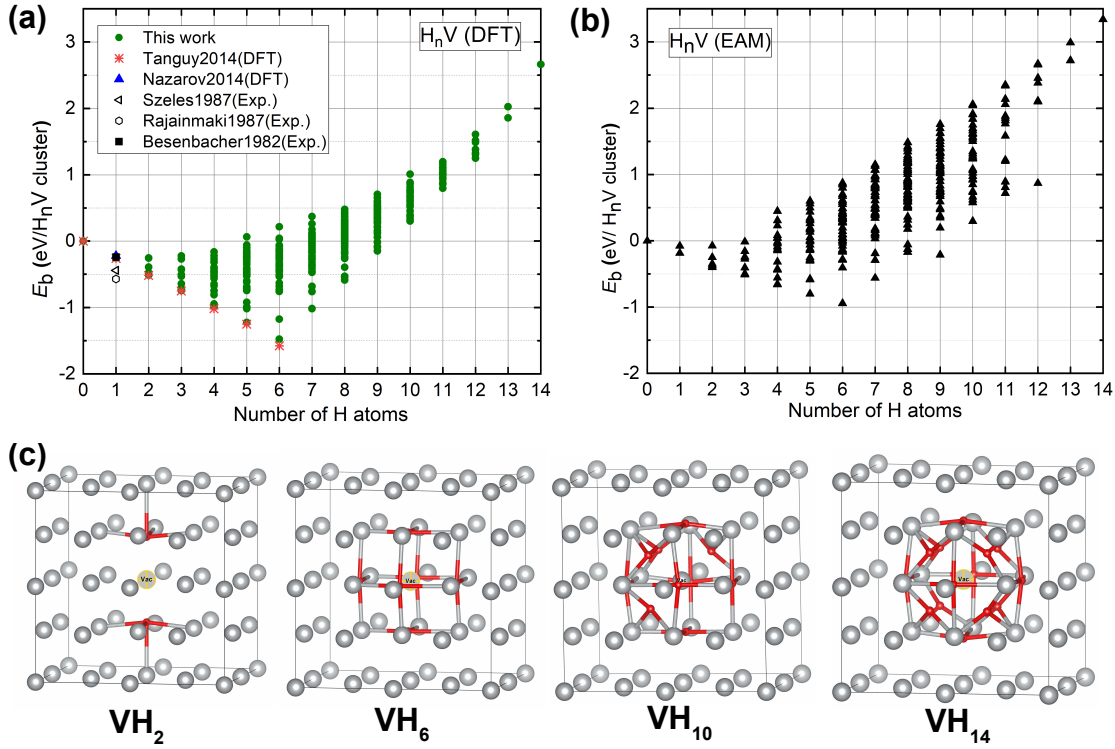


Fig. 8.3 Binding energies of VH_n clusters and the structures of selected clusters. (a) DFT results compared to the literature data [13, 11, 34, 35, 38, 37, 36]; (b) EAM results; (c) Structures of selected VH_n clusters with lowest binding energies for the given n .

placed at high-symmetry OS and TS positions next to the vacancy in all possible configurations at the nearest neighbor coordination shell of the vacancy (14 sites in total, shown by VH_{14} in Fig. 8.3(c)). The energies of the Ni- VH_n configurations have been evaluated from EAM total energy calculations and only those configurations with nonidentical energies have been selected for the further investigations using DFT calculations. The results shown in Fig. 8.3 suggest that the VH_6 cluster with H atoms occupying all 6 available OS positions surrounding the vacancy is the most preferred cluster configuration in the bulk of Ni at 0 K. Our DFT and EAM calculations predict the binding energies of -1.48 eV (DFT) and -0.94 eV (EAM) for the VH_6 cluster respectively. The results are in good qualitative and in reasonable quantitative agreement with available DFT literature data predicting the binding energies of -1.58 eV [12, 13] for the VH_6 cluster. Furthermore, it is found that the DFT and EAM calculations predict the same minimal-energy configuration for each VH_n cluster population. Some of the selected lowest energy VH_n structures ($n=2, 6, 10, \text{ and } 14$) are displayed in Fig. 8.3(c).

Having both 0 K DFT and EAM results on defect segregation energies as well as the VH_n cluster binding energies in Ni, we have proceeded with MD-EAM simulations of the VH_6

cluster stability in bulk Ni at finite temperatures by calculating MSD of H atoms. The MSD of H atoms from their original positions in the cluster at 0 K has been selected as a measure of the cluster integrity (zero means the cluster configuration has not changed and the larger the MSD the farther from the cluster origin have the H atoms moved). The results shown in Fig. 8.1 (d) indicate that the VH_6 cluster in bulk Ni stays intact when the temperature is below 250 K and falls apart as the temperature increases. According to the results of our calculations, the VH_6 clusters should not exist in a bound state at $T > 325$ K which includes the most relevant for the HE temperature interval (near the room temperature (RT)), it is also suggested by DFT-based study in Ref. [10] that the VH_n cluster of Ni is difficult to form at or above RT. Our calculations suggest that VH_6 decomposes into VH_5 at RT, which is also confirmed by the Monte Carlo simulations of Refs. [13, 39] that the repulsive H-H interactions could lead to lower activation energies for H detrapping from the VH_n clusters. Moreover, our results also indicate that the VH_6 clusters will completely dissociate at $T > 375$ K. This is consistent with the dissociation of the hydrogen-vacancy pairs at temperatures around 305 K [37] or within the range of 318–513 K [38] observed in the positron lifetime experiments.

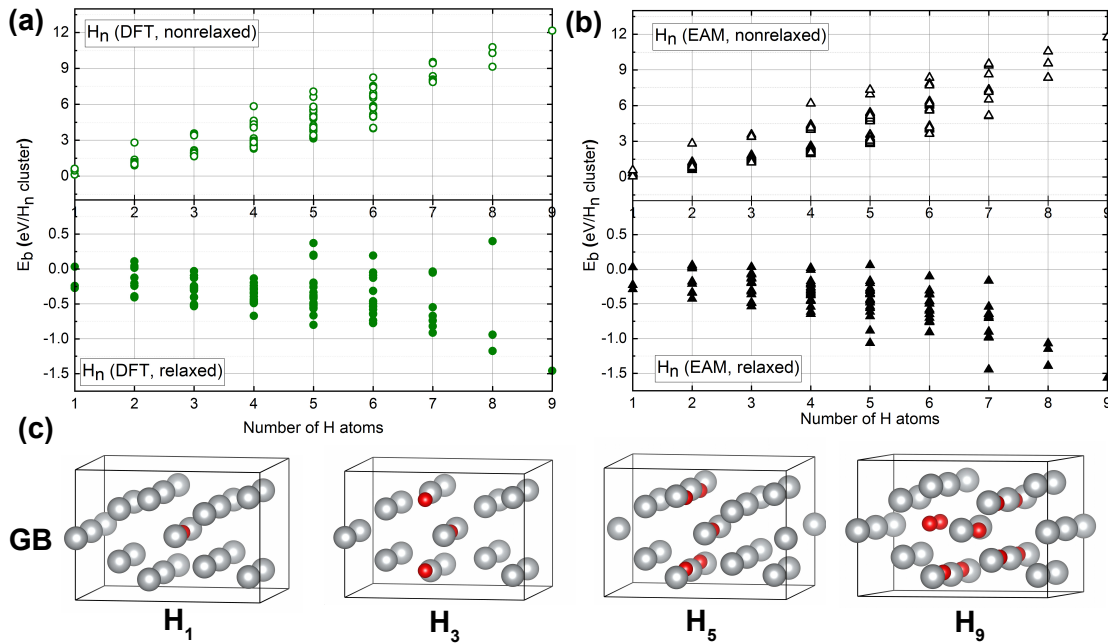


Fig. 8.4 Binding energy of H atoms at $\Sigma 5(012)$ GB and selected H cluster configurations. (a) DFT results; (b) EAM results; (c) H_1 , H_3 , H_5 , and H_9 cluster configurations, only 5 layers (-2 , -1 , 0 , 1 , 2 in Fig. 8.1) are shown for clarity.

8.3.3 H cluster at Ni grain boundary

In the final part of our study, we focus on the hydrogen cluster formation and stability at GBs in Ni. To this end, we have selected the $\Sigma 5$ (012) GB as the representative case. We have restricted our calculations to the first two coordination shells around the H atom occupying a site at the core of the GB, which has included 1 OS and 8 TS positions as shown in Fig. 8.1(b). Since the number of possible cluster configurations in the chosen cluster geometries is large for the explicit DFT calculations, we resorted to a pre-screening using EAM total energy calculations which is same as the selection for VH_n in bulk Ni shown in Fig. 8.3. Moreover, we show the binding energies of H_n from both relaxed and norelaxed calculations for the GB- H_n structures. The comparison between EAM and DFT calculations presented in Fig. 8.4 reveals a reasonable agreement in both relaxed and nonrelaxed cases. One notices that the nonrelaxed GB is not the preferential trap for H atoms due to the neglect of GB configuration optimization, while the relaxed both EAM and DFT calculations provide a consistent picture of slightly attractive binding energies of the considered H clusters, with the strongest binding energy corresponding to the H_9 cluster. Due to relatively small absolute values of the binding energies, we refer to the discrepancies between DFT and EAM results presented in Fig. 8.4 as minor.

In what follows, we are going to use the most stable GB H cluster found from our DFT calculations to check its stability against temperature in MD-EAM calculations. As shown in Fig. 8.1(e), the H_9 cluster of $\Sigma 5$ GB reconstructs already at 150 K. In addition, we have also investigated the stability of VH_6 complex at Ni $\Sigma 3$ (111) GB (see Fig. 8.1 (c)) reported in Ref. [17], it is found that the VH_6 cluster in Ni $\Sigma 3$ GB tends to dissociate when $T > 250$ K. Furthermore, both, the H_9 of $\Sigma 5$ GB and VH_6 of $\Sigma 3$ GB, can easily fall apart as the temperature increases up to 250 K and 350 K respectively. It is worth noting that the 0 K DFT binding energies of VH_6 cluster in bulk Ni, H_9 of $\Sigma 5$ GB, and VH_6 of $\Sigma 3$ GB are -0.247 eV/H (see Fig. 8.3(a)), -0.162 eV/H (see Fig. 8.4(a)), and -0.235 eV/H (estimated by formation energy from Ref[17]), respectively, which indicates that the vacancy of Ni exhibits as a strong trap for H atoms at 0 K. This similar behavior of H cluster binding to the vacancies of bulk and $\Sigma 3$ GB is mainly due to the fact of nearly identical atom arrangement between bulk Ni lattice and $\Sigma 3$ GB. Moreover, at finite temperature, as shown Fig. 8.1 (d)-(f), the VH_6 in bulk Ni still shows the similar stability to VH_6 cluster of $\Sigma 3$ GBs .

8.4 Conclusion

In summary, we would like to conclude that VH_6 clusters in bulk Ni and $\Sigma 3$ GB as well as H_9 cluster in Ni $\Sigma 5$ GB seem to be stable at low temperatures as predicted by theoretical

investigations in this work and in some earlier studies. However, the H clusters completely dissociate in all simulations at temperatures above 375 K. The VH_6 clusters in the bulk and $\Sigma 3$ GB turned out to be more stable than H_9 in $\Sigma 5$ GB due to the strong H atoms trapping to the vacancy. However, VH_6 clusters in the bulk and $\Sigma 3$ GB can be stable up to 300 K whereas H_9 cluster at $\Sigma 5$ GB loses their integrity already at $T > 225$ K. These results indicate that such H clusters may not be relevant for investigations of the mechanisms of HE associated with the hydrogen enhanced de-cohesion (HEDE) of Ni-base alloys at around RT and it is rather atomic H than H clusters that plays a major role in the phenomena of HEDE starting from 375 K. Both bulk and GB H clusters seem to play no or little role in the HE processes of Ni-base alloys at temperatures above the room temperature relevant for practical applications.

References

- [1] S. M. Myers, M. I. Baskes, H. K. Birnbaum, J. W. Corbett, G. G. DeLeo, S. K. Estreicher, E. E. Haller, P. Jena, N. M. Johnson, R. Kirchheim, S. J. Pearton, M. J. Stavola, *Rev. Mod. Phys.* 64 (1992) 559–617.
- [2] Y. Fukai, *The metal-hydrogen system: basic bulk properties*, second ed., Springer Science & Business Media, New York, 2006.
- [3] W. T. Geng, A. J. Freeman, R. Wu, C. B. Geller, J. E. Raynolds, *Phys. Rev. B* 60 (1999) 7149–7155.
- [4] M. Yamaguchi, M. Shiga, H. Kaburaki, *J. Phys. Soc. Jpn.* 73 (2004) 441–449.
- [5] A. Pundt, R. Kirchheim, *Ann. Rev. Mater. Res.* 36 (2006) 555–608.
- [6] I. M. Robertson, P. Sofronis, A. Nagao, M. L. Martin, S. Wang, D. W. Gross, K. E. Nygren, *Metall. Mater. Trans. A* 46 (2015) 2323–2341.
- [7] M. Nagumo, *Fundamentals of hydrogen embrittlement*, Springer Science & Business Media, Singapore, 2016.
- [8] N. Z. Carr, R. B. McLellan, *Acta Mater.* 52 (2004) 3273–3293.
- [9] E. H. Megchiche, C. Mijoule, M. Amarouche, *J. Phys.: Condens. Matter* 22 (2010) 485502.
- [10] Y.-W. You, X.-S. Kong, X.-B. Wu, Y.-C. Xu, Q. F. Fang, J. L. Chen, G.-N. Luo, C. S. Liu, B. C. Pan, Z. Wang, *AIP Advances* 3 (2013) 012118.
- [11] R. Nazarov, T. Hickel, J. Neugebauer, *Phys. Rev. B* 89 (2014) 144108.
- [12] D. Connétable, Y. Wang, D. Tanguy, *J. Alloys Compd.* 614 (2014) 211–220.
- [13] D. Tanguy, Y. Wang, D. Connétable, *Acta Mater.* 78 (2014) 135–143.
- [14] X. Zhou, D. Marchand, D. L. McDowell, T. Zhu, J. Song, *Phys. Rev. Lett.* 116 (2016) 075502.
- [15] A. Metsue, A. Oudriss, X. Feugas, *J. Alloys Compd.* 656 (2016) 555–567.

- [16] A. V. Subashiev, H. H. Nee, *J Nucl. Mater.* 487 (2017) 135–142.
- [17] X. Zhou, J. Song, *Acta Mater.* 148 (2018) 9–17.
- [18] A. Metsue, A. Oudriss, X. Feaugas, *Comput. Mater. Sci.* 151 (2018) 144–152.
- [19] P. E. Blöchl, *Phys. Rev. B* 50 (1994) 17953.
- [20] G. Kresse, J. Hafner, *Phys. Rev. B* 48 (1993) 13115–13118.
- [21] G. Kresse, J. Furthmüller, *Comput. Mater. Sci.* 6 (1996) 15–50.
- [22] J. P. Perdew, K. Burke, M. Ernzerhof, *Phys. Rev. Lett.* 77 (1996) 3865–3868.
- [23] H. J. Monkhorst, J. D. Pack, *Phys. Rev. B* 13 (1976) 5188–5192.
- [24] J. Bandyopadhyay, K. Gupta, *Cryogenics.* 17 (1977) 345–347.
- [25] S. Plimpton, *J. Comput. Phys.* 117 (1995) 1–19.
- [26] J. E. Angelo, N. R. Moody, M. I. Baskes, *Model. Simul. Mater. Sci. Eng.* 3 (1995) 289.
- [27] M. I. Baskes, X. Sha, J. E. Angelo, N. R. Moody, *Model. Simul. Mater. Sci. Eng.* 5 (1997) 651.
- [28] J. Song, W. Curtin, *Acta Mater.* 59 (2011) 1557–1569.
- [29] A. Tehranchi, W. Curtin, *J. Mech. Phys. Solids* 101 (2017) 150 – 165.
- [30] S. He, W. Ecker, R. Pippin, V. I. Razumovskiy, *Comput. Mater. Sci.* 167 (2019) 100–110.
- [31] V. Razumovskiy, A. Lozovoi, I. Razumovskii, *Acta Mater.* 82 (2015) 369–377.
- [32] D. D. Stefano, M. Mrovec, C. Elsässer, *Acta Mater.* 98 (2015) 306 – 312.
- [33] A. Alvaro, I. T. Jensen, N. Kheradmand, O. Løvvik, V. Olden, *Int. J. Hydrog. Energy* 40 (2015) 16892–16900.
- [34] J. K. Nørskov, F. Besenbacher, J. Bøttiger, B. B. Nielsen, A. A. Pisarev, *Phys. Rev. Lett.* 49 (1982) 1420–1423.
- [35] F. Besenbacher, J. Bøttiger, S. M. Myers, *J. Appl. Phys.* 53 (1982) 3536–3546.
- [36] S. M. Myers, P. Nordlander, F. Besenbacher, J. K. Nørskov, *Phys. Rev. B* 33 (1986) 854–863.
- [37] H. Rajainmaki, S. Linderöth, H. E. Hansen, R. M. Nieminen, *J. Phys. F: Met. Phys.* 18 (1988) 1109–1118.
- [38] C. Szeles, A. Vertes, *J. Phys. F: Met. Phys.* 17 (1987) 2031–2039.
- [39] Y. Wang, D. Connétable, D. Tanguy, *Acta Mater.* 103 (2016) 334–340.

Chapter 9

Thermodynamic and mechanical stability of Ni₃X-type compounds

9.1 Introduction

Ni₃X-type intermetallic compounds can be found in a form of so-called γ' , γ'' , and η precipitates in Ni-base alloys (NBA) [1–5]. These intermetallic compounds play an important role in stability and micro-structure property relationships in NBA [6–17]. The strength of some Ni-base alloys is confirmed due to the hardening precipitates of γ' -Ni₃(Al,Ti) (L1₂ crystal structure) and γ'' -Ni₃(Nb, Al, Ti) (D0₂₂ crystal structure) phases. Both the γ' and γ'' have good solubility of Cr, Fe, Nb, Mo and other elements that may be distributed on different crystal sublattices of both phases [18–21]. In Ni-base alloys containing sufficient amount of Ti and Nb, γ' and γ'' may transform to Ni₃X-type η phase which typically has mostly Ti on the X-sublattices (Ni₃X) and has an ordered hexagonal D0₂₄ crystal structure [6, 22].

One of the most frequently investigated intermetallic phase in NBA is L1₂-Ni₃Al [23–32]. Sluiter *et al.* [23] and Ruban *et al.* [24, 25, 32] proposed computational methods for evaluation of the site preference in multicomponent ordered intermetallic compounds with a focus on the L1₂-Ni₃Al system. Sluiter *et al.* [23] showed that early transition metals including Si and Ge preferred to go to the Al sublattice, whereas Fe, Co, and Pd had a strong preference for the Ni sublattice which was partly confirmed in an experimental study of Shindo *et al.*, who showed experimentally that Fe occupied primarily the Ni-sublattice in Ni₃Al [31]. Sluiter *et al.* [23] also found elements in the 3A, 5A, and 6A group had a noticeable only weak Al sublattice preference, while Cu and Ag had a weak Ni sublattice preference, but Cr and Cd had virtually no site preference. Ruban *et al.* [24, 25, 32] predicted similar trends in Ni₃Al system: Sc, Ti, V, Cr, Y, Zr, Nb, Mo, Tc, Lu, Hf, Ta, W, Re, and Os tended to occupy the Al-sublattice,

while Cu, Va, Pt, and Pd preferred the Ni-sublattice. Another set of first-principles total energy calculations was performed to investigate the site preference of Pt, Hf, Cr and Ir in L1₂-Ni₃Al by Jiang *et al.* [26]. They concluded that Pt has a predominant preference for the Ni sublattice, while Hf and Cr had a predominant preference for the Al sublattice in L1₂-Ni₃Al. Using first-principles calculations, Wu *et al.*[27] also found that Ti, Nb, Cr, Mo elements occupied Al sublattice, among them, Ti, Nb, Cr, and Mo increased shear and Young's moduli of single crystal Ni₃Al in all orientations. Liu *et al.* [30] studied the site preference of 3*d*, 4*d*, and 5*d* solutes in L1₂-Ni₃Al and they found that the preference of Al sublattice increased as the atomic number increased down the column in the periodic table, and decreased as the *d*-occupation number increased along the element period. This behavior has been also confirmed by the investigations from Ruban *et al.* [24, 25] and Jiang *et al.* [26].

The thermodynamic stability of other Ni₃Al structural modifications and other Ni₃X compounds are less known. Ni₃Al as well as Ni₃Nb, Ni₃Ti, Ni₃Cr, and Ni₃Fe in D0₂₂ structure have been studied in Refs. [33–39] by using *ab initio* calculations, Ni₃Ti in D0₂₄ structure has also been studied theoretically [39–42] and experimentally [43]. D0₂₂-Ni₃Nb and D0₂₄-Ni₃Ti phases have been found thermodynamically stable, though no systematic investigation of Ni₃X (X=Al, Ti, Nb, Mo, Fe, and Cr) has been provided for evaluation of the relative phase stability of Ni₃X intermetallic compounds.

The elastic properties of Ni₃X (X=Al, Ti, Nb, Mo, Fe, and Cr) intermetallic compounds play an important role in the description of mechanical properties of alloys where they are present in the form of precipitates [44]. A number of investigations have focused on the elastic properties of Ni₃X type intermetallic compounds [34–37, 39, 44–51]. For instance, Connétable *et al.* studied the binary phase D0₂₂-Ni₃Nb by first-principles calculations and concluded that the elastic behavior of D0₂₂-Ni₃Nb was close to Ni [34]. Using first-principles method, Dai *et al.* [35] also calculated elastic properties of D0₂₂-Ni₃Nb and obtained the values of C₁₁-C₁₂ =99.7 GPa and B/G=2.56 suggesting that D0₂₂-Ni₃Nb might have good ductility. Kim *et al.* have studied effects of alloying elements on elastic properties of Ni and L1₂-Ni₃Al by first-principles calculations, they found that the shear modulus decreased with alloying element additions caused by the expansion of equilibrium volume [46], they also observed that the bulk modulus of Ni₃Al alloys was strongly related to the total molar volume as well as the electron density and that the solute atom with high bulk modulus of its parent phase tended to contribute to the high bulk modulus of Ni₃Al [47].

The fundamental understanding of thermodynamic and mechanical stability of Ni₃X type intermetallic compounds is of major importance for the design of new alloys and for an accurate thermodynamic description of the materials containing these phases using methods of thermodynamic modeling like Calphad [52]. However, the literature data presented above, do not cover

some key alloying elements for the design of modern Ni-base alloys. These alloys are often composed of multiple alloying elements, which makes the investigation of the phase stability in compositionally complex alloys even more complicated as the phase formation is governed by the phase competition between multiple phases, some of which might be metastable and therefore virtually inaccessible for experimental investigations. So far, no systematic study on the thermodynamic and mechanical stability of the Ni₃X-type intermetallic compounds in the most common precipitates in Ni-base alloys L1₂, D0₂₂ and D0₂₄ structures has yet been reported.

In this study, we have selected typical alloying elements of Ni-based alloys, such as Al, Ti, Nb, Cr, Mo, and Fe, for the investigation of the phase stability of Ni₃X-type intermetallic compounds in the L1₂, D0₂₂, and D0₂₄ crystal structures by means of density functional theory (DFT) calculations. We have focused our study on thermodynamic and mechanical properties of these compounds, identified the most stable phases, and investigated the site occupancy as well as the solubility of the alloying elements in L1₂-Ni₃X intermetallic compounds.

9.2 Methodology

9.2.1 Structure models

The crystal structures used to model γ , γ' , γ'' , and η phases in DFT calculations are shown in Figure 9.1. γ phase has the face-centered cubic (fcc) A1 structure, the γ' phase has the L1₂-type ordered fcc-based crystal structure, the γ'' phase has the tetragonal D0₂₂ crystal structure, and the η phase has the D0₂₄ ordered hexagonal crystal structure. The L1₂, D0₂₂, and D0₂₄ have the same chemical composition of Ni₃X. In Table 9.1, the crystallographic data for the A1, L1₂, D0₂₂, and D0₂₄ structures are shown in detail [53].

Table 9.1 The crystallographic data for the A1, L1₂, D0₂₂, and D0₂₄ structures used in the calculations. N_{eq} represents the number of equivalent positions, and (x, y, z) represent the coordinates of the equivalent positions.

| Structure | Prototype | Space Group | Equivalent sites | N_{eq} | Wyckoff notation | (x, y, z) |
|------------------|--------------------|-------------------------------|------------------|----------|------------------|--|
| A1 | Cu | Fm3m, No. 225 | Cu | 4 | <i>a</i> | (0,0,0) |
| L1 ₂ | Ti ₃ Al | Pm3m, No. 221 | Al | 1 | <i>a</i> | (0,0,0) |
| | | | Ti | 3 | <i>c</i> | (0, $\frac{1}{2}$, $\frac{1}{2}$), ($\frac{1}{2}$, 0, $\frac{1}{2}$), ($\frac{1}{2}$, $\frac{1}{2}$, 0) |
| D0 ₂₂ | TiAl ₃ | I4/mmm, No. 139 | Ti | 2 | <i>a</i> | (0,0,0) |
| | | | Al _I | 2 | <i>b</i> | (0, 0, $\frac{1}{2}$) |
| | | | Al _{II} | 4 | <i>d</i> | (0, $\frac{1}{2}$, $\frac{1}{4}$), ($\frac{1}{2}$, 0, $\frac{1}{4}$), |
| D0 ₂₄ | Ni ₃ Ti | P6 ₃ /mmc, No. 194 | Ti _I | 2 | <i>a</i> | (0,0,0), (0,0, $\frac{1}{2}$) |
| | | | Ti _{II} | 2 | <i>c</i> | ($\frac{1}{3}$, $\frac{2}{3}$, $\frac{1}{4}$), ($\frac{2}{3}$, $\frac{1}{3}$, $\frac{3}{4}$) |
| | | | Ni _I | 6 | <i>g</i> | ($\frac{1}{2}$, 0, 0), (0, $\frac{1}{2}$, 0), ($\frac{1}{2}$, $\frac{1}{2}$, 0) |
| | | | | | | ($\frac{1}{2}$, 0, $\frac{1}{2}$), (0, $\frac{1}{2}$, $\frac{1}{2}$), ($\frac{1}{2}$, $\frac{1}{2}$, $\frac{1}{2}$) |
| | | | Ni _{II} | 6 | <i>h</i> | (x, 2x, $\frac{1}{4}$), (2 \bar{x} , \bar{x} , $\frac{1}{4}$), (x, \bar{x} , $\frac{1}{4}$) |
| | | | | | | (x, 2 \bar{x} , $\frac{3}{4}$), (2x, x, $\frac{3}{4}$), (\bar{x} , x, $\frac{3}{4}$) |

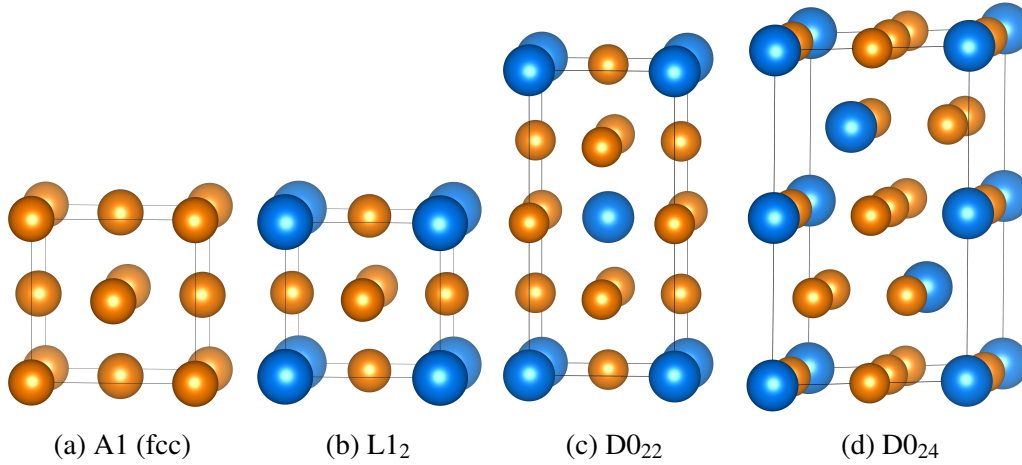


Fig. 9.1 The crystal structures of (a) A1 fcc-Ni, (b) L₁₂-Ni₃X, (c) D0₂₂-Ni₃X, and (d) D0₂₄-Ni₃X phases. The small (orange) spheres represent Ni atoms, the large (blue) spheres represent X atoms, *i.e.* Al, Ti, Nb, Cr, Mo, and Fe.

9.2.2 Computational details

We have used the Vienna *ab initio* simulation package (VASP) with the projector augmented wave (PAW) construction for the pseudopotential [54–56]. The spin-polarized generalized gradient approximation (GGA) in the form of Perdew-Burke-Ernzerhof (PBE) [57] has been employed for the exchange-correlation energy. The initial magnetic structure of all configurations has been set as ferromagnetic. The cut-off energy for plane waves has been set to 400 eV for all calculations. The convergence criteria of self-consistent calculations have been set to 10^{-5} eV/cell for the total energy and to 9×10^{-3} eV/Å for the atomic forces. The integration over the Brillouin zone has been done using the Monkhorst-Pack k -mesh method [58] and a dense mesh grid of around 7000 k -points/atom/cell (an equivalent density of $12 \times 12 \times 12$ k -mesh for the 4-atom conventional Ni or the L₁₂ cubic unit cell) has been employed in all calculations. The transfer energies and solution energies of solutes in L₁₂ phases was obtained by using a 108-atom supercell [$3 \times 3 \times 3(\times 4)$]. The cutoff energy, k -point mesh density, and the supercell size used in this work have been converged within 1 meV/atom, 0.2 meV/atom, and 6 meV/atom respectively.

9.2.3 Equation of state

We have employed the third-order Birch-Murnaghan isothermal equation of state given by [59]:

$$E(V) = E_0 + \frac{9V_0B_0}{16} \left(\left[\left(\frac{V_0}{V} \right)^{\frac{2}{3}} - 1 \right]^3 B'_0 + \left[\left(\frac{V_0}{V} \right)^{\frac{2}{3}} - 1 \right]^2 \left[6 - 4 \left(\frac{V_0}{V} \right)^{\frac{2}{3}} \right] \right), \quad (9.1)$$

where $E(V)$ is the total energy, V is the deformed volume, E_0 is the total energy which corresponds to the equilibrium volume V_0 , B_0 is the bulk modulus, and B'_0 is the pressure derivative of the bulk modulus.

9.2.4 Formation Enthalpy

The formation enthalpy (ΔH) of the γ' , γ'' and η precipitates was calculated using [60]:

$$\Delta H(\text{Ni}_n\text{X}_m) = \frac{E_0(\text{Ni}_n\text{X}_m) - nE_0(\text{Ni}) - mE_0(\text{X})}{m+n}, \quad (9.2)$$

where $E_0(\text{X})$ and $E_0(\text{Ni})$ are the 0 K total energies of the pure elements at their reference states (as shown in Table 9.2) and $E_0(\text{Ni}_n\text{X}_m)$ is the 0 K total energy of the compound Ni_nX_m .

9.2.5 Elastic properties

The number of elastic constants sufficient to describe the complete elastic tensor depends on the crystal symmetry. In particular, for the cubic crystals (A1 and L1₂): $C_{11}=C_{22}=C_{33}$, $C_{12}=C_{23}=C_{13}$, $C_{44}=C_{55}=C_{66}$, namely, cubic crystals only have three independent elastic constants: C_{11} , C_{12} and C_{44} . In the case of tetragonal crystal (D0₂₂): $C_{11}=C_{12}$, C_{12} , $C_{13}=C_{23}$, C_{33} , $C_{44}=C_{55}$, C_{66} , namely, tetragonal crystal has six independent elastic constants: C_{11} , C_{12} , C_{13} , C_{33} , C_{44} , C_{66} . In the case of hexagonal crystal (D0₂₄): $C_{11}=C_{12}$, C_{12} , $C_{13}=C_{23}$, C_{33} , $C_{44}=C_{55}$, $C_{66}=\frac{1}{2}(C_{11}-C_{12})$, namely, hexagonal crystal has five independent elastic constants: C_{11} , C_{12} , C_{13} , C_{33} , C_{44} . The elastic constants of single crystals in this work are shown as follows [61]:

$$C = \begin{pmatrix} C_{11} & C_{12} & C_{13} & 0 & 0 & 0 \\ C_{12} & C_{22} & C_{23} & 0 & 0 & 0 \\ C_{13} & C_{23} & C_{33} & 0 & 0 & 0 \\ 0 & 0 & 0 & C_{44} & 0 & 0 \\ 0 & 0 & 0 & 0 & C_{55} & 0 \\ 0 & 0 & 0 & 0 & 0 & C_{66} \end{pmatrix}. \quad (9.3)$$

The second order elastic constants calculations are calculated with the help of the ElaStic code [62, 63]. The mechanical stability of the proposed compounds is analyzed by means of

Cauchy-Born criteria [64, 65] as follows:

$$C_{11} - C_{12} > 0, \quad (9.4)$$

$$C_{11} + 2C_{12} > 0, \quad (9.5)$$

$$C_{44} > 0 \quad (9.6)$$

for the cubic crystal structures (A1 and L1₂) and

$$C_{11} > |C_{12}|, \quad (9.7)$$

$$2C_{13}^2 < C_{33}(C_{11} + C_{12}), \quad (9.8)$$

$$C_{44} > 0, \quad (9.9)$$

$$C_{66} > 0 \quad (9.10)$$

for the tetragonal and hexagonal crystal structures (D0₂₂ and D0₂₄).

The bulk modulus can be evaluated using the obtained single crystal elastic constants. Voigt [66] proposed to assume uniform strain within the heterogeneous material, thus B_V can be calculated by

$$9B_V = (C_{11} + C_{22} + C_{33}) + 2(C_{12} + C_{13} + C_{23}) \quad (9.11)$$

and the shear modulus G_V follows as

$$15G_V = (C_{11} + C_{22} + C_{33}) - (C_{12} + C_{13} + C_{23}) + 3(C_{44} + C_{55} + C_{66}). \quad (9.12)$$

Reuss [67] approximated the stress field in a polycrystalline material as uniform, thus the bulk modulus B_R can be calculated by

$$1/B_R = (S_{11} + S_{22} + S_{33}) + 2(S_{12} + S_{13} + S_{23}) \quad (9.13)$$

and the shear modulus G_R follows as

$$15/G_R = 4(S_{11} + S_{22} + S_{33}) - 4(S_{12} + S_{13} + S_{23}) + 3(S_{44} + S_{55} + S_{66}), \quad (9.14)$$

where S_{ij} is the inverse of the elasticity matrix C_{ij} [61].

Hill [68] proved that the Voigt and Reuss equations were upper and lower limits of the true polycrystalline bulk or shear modulus, which led to a practical estimate of the bulk and shear modulus by the arithmetic means of the extremes. Hence, the elastic modulus of the

polycrystalline material can be approximated by

$$B_H = \frac{B_V + B_R}{2} \quad (9.15)$$

for the bulk moduli and

$$G_H = \frac{G_V + G_R}{2} \quad (9.16)$$

for the shear moduli, the corresponding estimate of Young's moduli is obtained by

$$E_H = \frac{9B_H G_H}{3B_H + G_H}. \quad (9.17)$$

Additionally, we apply a universal anisotropy index A^U [69, 70] to provide a unique measure of anisotropy for cubic, tetragonal, and hexagonal crystal symmetries. A^U is then defined as

$$A^U = 5 \frac{G_V}{G_R} + \frac{B_V}{B_R} - 6, \quad (9.18)$$

which is valid for any crystallite symmetry and A^U is zero for a locally isotropic single crystals.

9.2.6 Solute sublattice preference in $L1_2$ - Ni_3X

As it has been shown in Table 9.1, the ordered $L1_2$ structure of γ' - Ni_3X consists of two sublattices, *i.e.*, the a -sublattice (the face centers) and the b -sublattice (cube corner), with the a -sublattice having three times the number of lattice sites than the b -sublattice. In perfectly ordered stoichiometric Ni_3Al , the a -sublattice is fully occupied by Ni and the b -sublattice by X atoms. Ruban *et al.* [25, 24] introduced a method to predict the site preference of ternary alloying elements in $L1_2$ - Ni_3Al at 0 K by calculating the transfer energy in a binary compound Ni_3X which only contained two inequivalent sites. In this case, the site preference can be determined from the transfer energy, which is the energy of a transfer of an impurity Y from a Ni site to a X site, while an X from that site goes to the Ni site, where the Y atom has been before:

$$E_{Ni \rightarrow X}^Y = E^Y(X) + E^X(Ni) - E^Y(Ni) - E_{Ni_3X}, \quad (9.19)$$

here $E_{Ni \rightarrow X}^Y$ is the transfer energy, while $E^Y(X)$ and $E^Y(Ni)$ are the energies of the Ni_3X supercell with an Y atom on X and Ni site, respectively; $E^X(Ni)$ is the energy of the Ni_3X supercell with one X antisite; E_{Ni_3X} is the total energy of Ni_3X supercell. A negative transfer energy means a site preference to X site in Ni_3X .

9.2.7 Solution energy in in L1₂-Ni₃X

The solution energy of a Y impurity on the preferred sublattice in Ni₃X can be calculated using [71]:

$$E_{\text{sol}}^Y = E_{\text{Ni}_3\text{X}}^Y(\text{Ni}/\text{X}) - E_{\text{Ni}_3\text{X}} - E_{\text{ref}}(\text{Y}) + E_{\text{ref}}(\text{Ni}/\text{X}), \quad (9.20)$$

where E_{sol}^Y represents the solution energy and $E_{\text{Ni}_3\text{X}}^Y(\text{Ni}/\text{X})$ the 0 K total energy of Ni₃X with one solute at its preferred sublattice; $E_{\text{ref}}(\text{Y})$ and $E_{\text{ref}}(\text{Ni}/\text{X})$ are the reference state energies (per atom) of the Y and Ni or X atom, respectively.

9.3 Results and discussion

9.3.1 Reference state properties of elements

We have calculated the ground state structures of Ni, Al, Nb, Cr, Mo, Fe, and Ti, which have been later used to obtain the enthalpies of formation as the reference states. Among those components, the crystal structures of Ni and Al are the face-centered cubic (fcc), while Nb, Cr, Mo and Fe have a body-centered cubic (bcc) structure, and Ti a hexagonal close packed (hcp) structure. The calculated equilibrium lattice constants of pure Ni, Al, Nb, Cr, Mo, Fe, and Ti are compared to the available literature data in Table 9.2. Our results show good agreement to previous experimental and theoretical studies [34, 39, 45, 47, 72–88].

Table 9.2 The calculated 0 K equilibrium lattice constants and bulk moduli of reference state pure elements Ni, Al, Nb, Cr, Mo, Fe, Ti. 0 K DTF and available low temperature experimental literature data are also shown in the table for comparison.

| Ele. | Lattice constants (Å) | | | Bulk modulus (GPa) | | |
|------|---------------------------|--------------------------------|--------------------------------|--------------------|--------------------|--------------------|
| | This work | Ref. Exp. | Ref. DFT | This work | Ref. Exp. | Ref. DFT |
| Ni | 3.519 | 3.520 [72] | 3.521 [47], 3.515 [74] | 195 | 188 [75] | 192 [76] |
| Al | 4.043 | 4.047 [73] | 4.047 [47] | 77 | 76 [45] | 82 [89] |
| Nb | 3.325 | 3.300 [72], 3.280 [77] | 3.313 [34] | 169 | 172 [78], 168 [77] | 174 [79], 182 [80] |
| Cr | 2.847 | 2.884 [73] | 2.848 [47], 2.849 [81] | 256 | 166 [82], 198 [83] | 255 [81] |
| Mo | 3.160 | 3.147 [84], 3.120 [77] | 3.140 [80] | 257 | 263 [85], 265 [84] | 254 [79], 285 [80] |
| Fe | 2.837 | 2.867 [86] | 2.838 [87] | 174 | 173 [86] | 194 [87] |
| Ti | $a=b=4.578,$ $c=2.829$ | $a=b=4.680,$ $c=2.940$ [73] | $a=b=4.577,$ $c=2.829$ [39] | 113 | 110 [90] | 123 [88] |

9.3.2 Thermodynamic stability of Ni₃X-type intermetallic compounds

In Table 9.3, we present the enthalpy of formation ΔH of Ni₃X-type γ' , γ'' , and η phases obtained using Equation 9.2. The calculated results are in good agreement with available theoretical and experimental literature data [28, 29, 33–36, 38–43, 47, 49, 50, 91]. The

enthalpies of formation of L1₂ structure Ni₃Mo, D0₂₂-Ni₃Mo, D0₂₄-Ni₃Mo, D0₂₄-Ni₃Nb, D0₂₄-Ni₃Cr and D0₂₄-Ni₃Fe intermetallic compounds have been calculated for the first time to the best of our knowledge. ΔH of all phases except for L1₂-Ni₃Mo and D0₂₄-Ni₃Mo is negative indicating thermodynamic stability of the calculated phases at 0 K. L1₂-Ni₃Mo and D0₂₄-Ni₃Mo have slightly positive formation enthalpies, meaning that they could be, in principle, stabilized by temperature and chemical disorder effects at elevated temperatures.

Table 9.3 Equilibrium lattice constants and formation enthalpies (per atom) at 0 K compared to 0 K DFT and low temperature experimental literature data.

| Compunds | Lattice parameter (Å) | | ΔH (eV/atom) | Reference | |
|--------------------|-----------------------|-------|----------------------|------------|------------|
| | $a=b$ | c | | | |
| L1 ₂ | Ni ₃ Al | 3.567 | 3.567 | -0.429 | This work |
| | | 3.561 | 3.561 | -0.430 | DFT: [39] |
| | | 3.571 | 3.571 | -0.430 | DFT: [28] |
| | | 3.571 | 3.571 | - | DFT: [29] |
| | | - | - | -0.440 | DFT: [47] |
| | Ni ₃ Ti | 3.569 | 3.569 | -0.421 | DFT: [50] |
| | | 3.611 | 3.611 | -0.475 | This work |
| | | 3.618 | 3.618 | -0.493 | DFT: [49] |
| | | 3.640 | 3.640 | - | Exp.: [40] |
| | Ni ₃ Nb | 3.610 | 3.610 | -0.420 | DFT: [50] |
| | | 3.693 | 3.693 | -0.138 | This work |
| | | 3.695 | 3.695 | -0.128 | DFT: [39] |
| | | 3.689 | 3.689 | -0.154 | DFT: [34] |
| | Ni ₃ Cr | 3.685 | 3.685 | -0.150 | DFT: [50] |
| | | 3.551 | 3.551 | -0.009 | This work |
| 3.545 | | 3.545 | -0.005 | DFT: [39] | |
| Ni ₃ Mo | 3.551 | 3.551 | -0.002 | DFT: [50] | |
| | 3.643 | 3.643 | 0.085 | This work | |
| Ni ₃ Fe | 3.651 | 3.651 | -0.082 | DFT: [50] | |
| | 3.543 | 3.543 | -0.083 | This work | |
| | 3.538 | 3.538 | -0.094 | DFT: [39] | |
| | | 3.544 | 3.544 | -0.082 | DFT: [50] |
| D0 ₂₂ | Ni ₃ Al | 3.644 | 6.866 | -0.399 | This work |
| | | 3.540 | 7.200 | -0.223 | DFT: [33] |
| | Ni ₃ Ti | 3.602 | 7.298 | -0.432 | This work |
| | | - | - | -0.446 | Exp.: [91] |
| | Ni ₃ Nb | 3.619 | 7.600 | -0.314 | This work |
| | | 3.637 | 7.517 | -0.261 | DFT: [39] |
| | | 3.649 | 7.508 | -0.345 | DFT: [36] |
| | | 3.653 | 7.503 | - | DFT: [35] |
| | | - | - | -0.308 | DFT: [34] |
| | Ni ₃ Cr | 3.640 | 7.500 | - | DFT: [38] |
| | | 3.463 | 7.272 | -0.018 | This work |
| | | 3.505 | 7.153 | -0.014 | DFT: [39] |
| | Ni ₃ Mo | 3.567 | 7.491 | -0.079 | This work |
| | Ni ₃ Fe | 3.486 | 7.320 | -0.062 | This work |
| | | 3.534 | 7.080 | -0.072 | DFT: [39] |
| D0 ₂₄ | Ni ₃ Al | 4.814 | 7.847 | -0.412 | This work |
| | Ni ₃ Ti | 5.102 | 8.332 | -0.493 | This work |
| | | 5.096 | 8.312 | -0.481 | DFT: [39] |
| | | 5.109 | 8.299 | -0.488 | DFT: [41] |
| | | 5.100 | 8.300 | - | DFT: [40] |
| | | 5.088 | 8.299 | -0.480 | DFT: [42] |
| | - | - | -0.446 | Exp.: [43] | |
| | Ni ₃ Nb | 4.959 | 7.083 | -0.266 | This work |
| | Ni ₃ Cr | 4.785 | 4.785 | -0.028 | This work |
| | Ni ₃ Mo | 4.904 | 7.993 | 0.029 | This work |
| | Ni ₃ Fe | 4.778 | 7.789 | -0.079 | This work |

Among all considered chemical variations, one can select the Ni_3Al , Ni_3Ti and Ni_3Nb intermetallic compounds as most stable in the $L1_2$, $D0_{22}$ and $D0_{24}$ structures, respectively. This result is in good agreement with experimental observations suggesting that Al, Ti and Nb alloying elements are strong inhibitors of the intermetallic phase precipitates in Ni-base alloys [7]. Cr, Mo and Fe form much less thermodynamically stable $L1_2$, $D0_{22}$ and $D0_{24}$ phases, namely, their formation enthalpies are close to zero.

The Ni_3Al compound has the most thermodynamically stable structure of $L1_2$ in terms of the absolute structural stability of each of the considered Ni_3X -type intermetallic compounds. This result is confirmed by experimental observations of this phase in Ni-Al [92, 93] and Ni-Al-based alloys [7–9, 16]. The Ni_3Ti compound has $D0_{24}$ as the most stable structure, which is also known as η phase and plays an important role in the strengthening of some NBA [7, 94]. In the case of Ni_3Nb , the most stable structure is $D0_{22}$, which is known as the γ'' phase [95, 96] and contributes to strengthening of Ni-based superalloys via coherency strains created between the γ'' precipitates and the matrix [97]. Furthermore, the most thermodynamically stable crystal structures for the other three considered intermetallic compounds have been found as follows: i) $L1_2$ for Ni_3Fe ; ii) $D0_{22}$ for Ni_3Mo ; and iii) $D0_{24}$ for Ni_3Cr . The latter three phases have not been observed experimentally as they have significantly higher formation enthalpies compared to the Ni_3Al , Ni_3Ti and Ni_3Nb phases that are much more stable in all considered structural modifications.

The formation enthalpy and lattice constants of $L1_2\text{-Ni}_3\text{X}$ (X =transition metals) have been investigated in literature Ref. [50], the authors have shown an ideal parabolic variation of lattice parameters with minimum occurring around the column of Fe/Ru/Os and the column of Ni/Pd/Pt 3d-5d metals. In the case of formation enthalpy, they also found that the elements taking the position of X in $L1_2\text{-Ni}_3\text{X}$ situated to the left from Cr, Mo and W yielded in the negative enthalpies, while the elements situated to the right resulted in the positive enthalpies. Mn, Fe, Pt, and Zn stood out as an exception. In this work, we have only investigated some selected elements of our interest which might be insufficient for studying trends of lattice constants and formation enthalpy across the periodic table, however, as shown in Table 9.3, our calculated results for $L1_2\text{-Ni}_3\text{X}$ are in good agreement with the results of Ref. [50]. We also observe similar to $L1_2\text{-Ni}_3\text{X}$ trends of the lattice parameter and formation enthalpy changes with changing X in $D0_{22}$ and $D0_{24}$ Ni_3X compounds.

9.3.3 Mechanical stability of precipitate phase

Table 9.4 shows the results of our DFT calculations of the elastic properties of Ni_3X intermetallic compounds. The results show good agreement with literature data [34, 35, 39, 44–49, 51].

The elastic properties of Ni₃Al and Ni₃Ti in D0₂₂ structure, Ni₃Al and Ni₃Nb in D0₂₄ structure have not been calculated so far to the best of our knowledge.

There are just three independent elastic constants C_{11} , C_{12} and C_{44} in the case of cubic structures A1 and L1₂. According to the Cauchy-Born criteria (Equations 9.4, 9.5, and 9.6), one can see all of three elastic constants for each composition in L1₂ structure are positive and C_{11} is always larger than C_{12} , which means the Ni₃Al, Ni₃Ti, and Ni₃Nb in L1₂ structures are mechanically stable. All results for the elastic properties of L1₂ compounds are rather close to each other and to pure Ni with an exception of Ni₃Nb which has an abnormally low C_{44} value that might be an indication of a soft mode in the phonon spectrum and that the element is on the verge of mechanical stability for this class of compounds as it should be easily deformed by a shear strain corresponding to the monoclinic deformation of the crystal[89].

The number of independent elastic constants increases to six in the case of a D0₂₂ tetragonal structure and to five in the case of a D0₂₄ hexagonal structure, respectively. The calculated elastic constants are in good agreement with previous studies for Ni₃Al and Ni₃Ti intermetallic compounds [34, 35, 39, 44]. All phases are found to be mechanically stable according to the Cauchy-Born criteria. In the D0₂₂ phase, Ni₃Ti and Ni₃Nb have larger elastic constants than the Ni₃Al in general indicating that they may be elastically stiffer than the latter phase. In the case of D0₂₄ phase, Ni₃Al and Ni₃Ti phases have very similar elastic properties, whereas the Ni₃Nb phase shows somewhat higher C_{11} , C_{12} and C_{13} and lower C_{33} , C_{44} and C_{66} components of the elastic tensor suggesting that the Ni₃Nb should be prone to easier shear deformation than Ni₃Ti and Ni₃Al.

The bulk and polycrystalline averaged Young's and shear moduli of Ni₃X compounds are given in Table 9.4. The bulk modulus calculated by means of the Birch-Murnaghan equation of state calculations (Equation 9.1, B_0)[59] and from the elastic constants using the Hill's averaging (Equation 9.15, B_H) are shown in the right part of Table 9.4. Both independently obtained values of bulk modulus are in good agreement with each other as well as with the results of earlier investigations [34, 35, 39, 44, 45, 47–49, 51]. The bulk modulus of Ni₃X-type intermetallic compounds (177-209 GPa) is rather close to that of Ni (198 GPa). The Young's moduli and shear moduli of Ni₃X are on the other hand generally lower in comparison to pure Ni, which agrees well with the previous studies as well [34, 35, 39, 44, 45, 47–49, 51].

We have used the calculated elastic constants of L1₂, D0₂₂ and D0₂₄ Ni₃X compounds to evaluate their elastic anisotropy. For this purpose, we have employed the universal anisotropy index as proposed in Ref. [69]. According to the definition, the ideally isotropic crystal would have $A^U=0$. The stronger the deviation from 0 is the larger the degree of elastic anisotropy. The results presented in Table 9.4 show that Ni₃Al is the most elastically anisotropic compound in all considered structures, whereas Ni₃Nb and Ni₃Ti are more isotropic with A^U close to or

Table 9.4 The elastic constants, bulk moduli and universal anisotropy index of A1, L1₂, D0₂₂, and D0₂₄ structures compared to available 0 K DFT and low temperature experimental literature data.

| Structure | | Elastic constants (GPa) | | | | | | Elastic moduli (GPa) | | | | A ^U | Reference |
|------------------|--------------------|-------------------------|-----------------|-----------------|-----------------|-----------------|-----------------|----------------------|----------------|----------------|----------------|----------------|------------|
| | | C ₁₁ | C ₁₂ | C ₁₃ | C ₃₃ | C ₄₄ | C ₆₆ | B ₀ | B _H | E _H | G _H | | |
| A1 | Ni | 274 | 160 | – | – | 131 | – | 195 | 198 | 243 | 94 | 0.88 | This work |
| | | 276 | 159 | – | – | 132 | – | – | 198 | – | 95 | 0.84 | DFT: [39] |
| | | 281 | 157 | – | – | 132 | – | – | 198 | 265 | 104 | – | DFT: [46] |
| | | 261 | 151 | – | – | 132 | – | – | – | – | – | – | Exp.: [45] |
| | | 255 | 152 | – | – | 125 | – | – | 184 | 224 | 87 | – | Exp.: [51] |
| L1 ₂ | Ni ₃ Al | 242 | 148 | – | – | 128 | – | 178 | 179 | 222 | 86 | 1.31 | This work |
| | | 238 | 147 | – | – | 129 | – | – | 177 | – | 85 | 1.45 | DFT: [39] |
| | | 242 | 152 | – | – | 125 | – | – | 182 | 217 | 83 | – | DFT: [47] |
| | | 240 | 160 | – | – | 124 | – | – | 187 | 207 | 79 | – | DFT: [48] |
| | | 223 | 145 | – | – | 125 | – | – | 171 | 200 | 77 | – | Exp.: [51] |
| | Ni ₃ Ti | 281 | 142 | – | – | 118 | – | 189 | 188 | 245 | 95 | 0.34 | This work |
| | | 288 | 148 | – | – | 120 | – | – | 194 | 250 | 97 | – | DFT: [49] |
| | Ni ₃ Nb | 240 | 175 | – | – | 20 | – | 200 | 197 | 70 | 24 | 0.29 | This work |
| | | 268 | 179 | – | – | 16 | – | – | 208 | – | 24 | 1.40 | DFT: [39] |
| | | | | | | | | | | | | | |
| D0 ₂₂ | Ni ₃ Al | 249 | 127 | 167 | 198 | 121 | 97 | 178 | 179 | 179 | 67 | 3.27 | This work |
| | Ni ₃ Ti | 250 | 156 | 155 | 261 | 112 | 128 | 185 | 188 | 216 | 83 | 0.98 | This work |
| | Ni ₃ Nb | 295 | 192 | 146 | 305 | 108 | 122 | 210 | 207 | 237 | 91 | 0.50 | This work |
| | | 286 | 181 | 160 | 308 | 112 | 116 | – | 209 | – | 89 | 0.51 | DFT: [39] |
| | | 288 | 188 | 162 | 299 | 115 | 104 | – | – | – | – | – | DFT: [35] |
| | | 283 | 180 | 165 | 292 | 112 | 102 | – | 200 | – | – | – | DFT: [44] |
| | | 285 | 180 | 159 | 306 | 113 | 119 | – | 208 | 235 | 90 | – | DFT: [34] |
| D0 ₂₄ | Ni ₃ Al | 313 | 122 | 105 | 337 | 63 | 96 | 177 | 181 | 218 | 84 | 0.30 | This work |
| | Ni ₃ Ti | 339 | 124 | 107 | 358 | 85 | 108 | 189 | 190 | 257 | 101 | 0.11 | This work |
| | | 334 | 133 | 111 | 356 | 83 | 101 | – | 192 | – | 97 | 0.10 | DFT: [39] |
| | Ni ₃ Nb | 309 | 174 | 146 | 318 | 55 | 68 | 200 | 207 | 179 | 66 | 0.16 | This work |

smaller than that of pure Ni. The D0₂₂-Ni₃Al compound has been identified as the one with the most pronounced elastic anisotropy of all studied structures.

9.3.4 Solute site preference and solubility in L1₂-Ni₃X intermetallic compounds

The solubility of Al, Ti, Nb, Cr, Mo, and Fe atoms in the most stable Ni₃Al, Ni₃Ti and Ni₃Nb phases (see Section 3.2) has been investigated for the case of the L1₂ crystal structure. This Ni₃X (X=Al, Ti, Nb)-type phase has 2 nonequivalent sublattices that can be occupied by the alloying elements mentioned above. Here, we use the concept of the so-called transfer energies (see Section 2.6) to calculate the sublattice preference of each element [32]. The results presented in Figure 9.2 indicate a site preference of solute Y on Ni-sublattice (red blocks, $E_{Ni \rightarrow X}^Y > 0$) or on X-sublattice (green blocks, $E_{Ni \rightarrow X}^Y < 0$) in the L1₂-Ni₃X intermetallic compounds. One can also notice that when an X atom site preference is taken into account in the Ni₃X compound, according to Equation 9.2.6, the transfer energy $E_{Ni \rightarrow X}^Y$ should be zero, as it is shown in the Figure 9.2 by white blocks.



Fig. 9.2 The transfer energy (in eV) heat map for $L1_2$ - Ni_3X ($X=Al, Ti, Nb$) intermetallic compounds compared to literature results ([Ref] Ni_3Al) from Ruban *et al.* [25, 32]. Green blocks represent the X site preference, red blocks show the Ni site preferences.

The calculated results suggest that Al, Ti, Nb, Cr, and Mo have the Al-sublattice site preferences while Fe has Ni-sublattice site preference in Ni_3Al . Our results are in good quantitative agreement with the results from Ruban *et al.* [32]. Sluiter *et al.* [23] have not provided the transfer energies we could compare our results to, but their site preference studies have indicated that Ti, Nb, Mo occupied Al site and Fe had strong site preference on Ni-sublattice, which are in agreement with the results from Ruban *et al.* [32] and Wu *et al.* [27]. Ruban *et al.* have also proposed that the site occupation reversal of Fe could be observed in Ni_3Al due to the asymmetrical form of the entropy, increasing temperature, or the compositions of the alloys. The composition effect on site preference has been also confirmed from the experiment by Shindo *et al.* [31]. They found that the site occupation of Fe depended strongly on the composition of the host elements. Our results confirm these findings. In the case of Ni_3Ti and Ni_3Nb , only Al has a strong preference to the Ti-sublattice and Al, Ti, and Fe have a preference to the Nb-sublattice respectively. We relate this strong qualitative difference in the sublattice preference of Nb, Cr, Mo and Fe in Ni_3Al , Ni_3Ti and Ni_3Nb to the fact that all of them have different ground state structures: $L1_2$ in the case of Ni_3Al , $D0_{24}$ in the case of Ni_3Ti and $D0_{22}$ in the case of Ni_3Nb .

In Ref [30] it has been discussed that the solute site preference in $L1_2$ - Ni_3Al may depend on the ratio of the atomic radii of the sublattice-forming element and of the solute atom. It has been suggested that solutes that deviate from the atomic radius of Ni by $> 15\%$ are prone to

occupy the Al sub-lattice and otherwise if the deviation is $< 15\%$. Indeed, this simple rule seems to work (at least qualitatively) for all solute elements we have studied in $L1_2$ - Ni_3Al as shown in Figure 9.3 with a threshold of about 3% for the atomic radius difference [98]. However, this simple rule does not seem to hold true for the cases of $L1_2$ - Ni_3Ti and $L1_2$ - Ni_3Nb as there is no systematic behavior of solutes as a function of the atomic radius any more. As it has been discussed in Ref. [30], the atomic size alone cannot be used to explain the behavior and a direct DFT calculation is required to get the site preference right.

Once the site preference has been known, we have calculated the solution energies of Al, Ti, Nb, Cr, Mo and Fe atoms on the preferred sublattice. Negative solution energies indicate that an element is soluble on the energetically favorable sublattice (after the results presented in Figure 9.2). As one can see from Figure 9.3, only Ti and Nb atoms that occupy the Al-sublattice have negative solution energies in Ni_3Al . In the case of Ni_3Ti , Al on Ti-sublattice and Fe on Ni-sublattice have negative solution energies indicating possibly high solubility on the corresponding sublattices. Al, Ti and Fe should have a sizeable solubility on the Nb sublattice and Cr and Mo on the Ni-sublattice in the case of Ni_3Nb compound according to the results of our calculations.

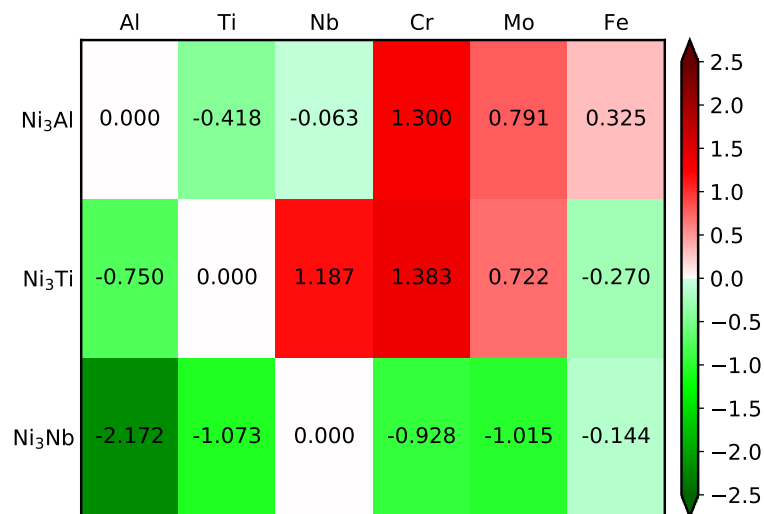


Fig. 9.3 The solution energy (in eV) heat map for $L1_2$ - Ni_3X ($X=Al, Ti, Nb$) intermetallic compounds. Green blocks represent solutes with negative solution energies and red blocks represent solutes with positive solution energies on the preferred sublattice chosen according to the results on the transfer energies shown in Figure 9.2.

We have also plotted the element transfer energy in $L1_2$ - Ni_3X intermetallic compounds as a function of atomic radius in Figure 9.4, which shows that the lowest transfer energy always

appears for the solute which has the similar or close atomic radius to the replaced atom. For example, Nb has the lowest transfer energy on the Al sub-lattice in the $L1_2$ - Ni_3Al , meaning possible Nb occupation on the corresponding sublattices. The same behavior can be seen for Al on the Ti sub-lattice in the $L1_2$ - Ni_3Ti and on the Nb sub-lattice in the $L1_2$ - Ni_3Nb .

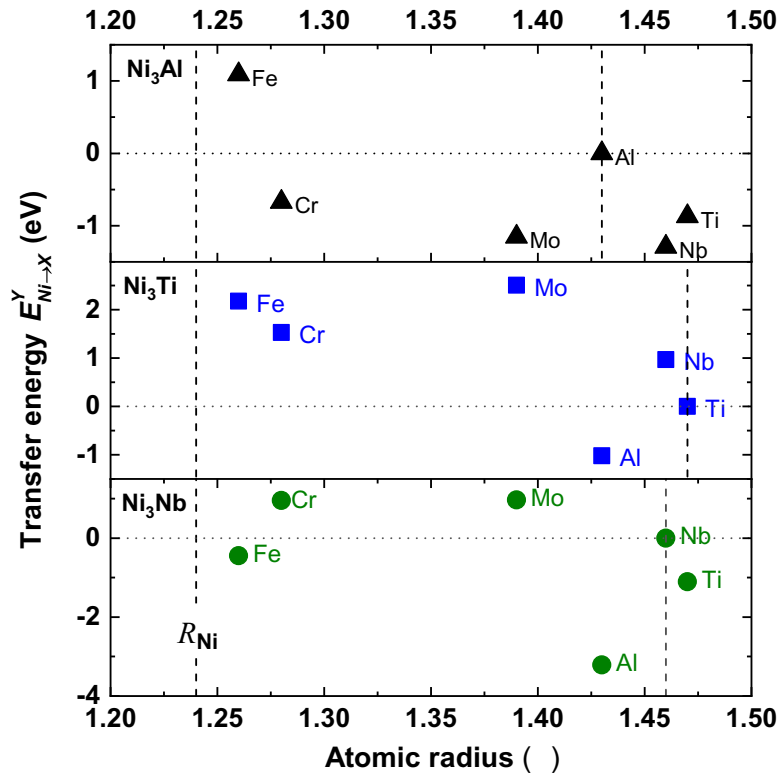


Fig. 9.4 The transfer energy of solutes in $L1_2$ - Ni_3X ($X=Al, Ti, Nb$) intermetallic compounds as a function of the solute atomic radius. The metallic radii of the elements are taken from Ref.[98]. The vertical dash lines are the atomic radii of the elements forming sublattices and the horizontal dot lines correspond to $E_{Ni \rightarrow X}^Y=0$ eV.

A similar analysis could be done for $D0_{22}$ and $D0_{24}$ phases as well. However, it would require to consider 3 and 4 instead of 2 for $L1_2$ sublattices respectively (see Table 9.1). The transfer energy formalism defined for the case of $L1_2$ structure is presently unavailable for these two cases and requires a separate study. Moreover, the associated DFT calculations would require substantial computational resources and, therefore, such an investigation goes beyond the scope of the present paper.

9.4 Conclusion

The equilibrium lattice constants, thermodynamic and mechanical properties of Ni_3X ($\text{X} = \text{Al}, \text{Ti}, \text{Nb}, \text{Cr}, \text{Mo},$ and Fe) intermetallic compounds in L1_2 , D0_{22} , and D0_{24} structures often found as γ' , γ'' and η precipitates in Ni-base alloys have been studied by means of density functional theory calculations. The site preferences of Al, Ti, Nb, Mo, Fe, and Cr alloying elements in L1_2 - Ni_3X ($\text{X} = \text{Al}, \text{Ti}, \text{Nb}$) phases as well as their solubility in the aforementioned phases have been studied. The formation enthalpies of Ni_3Mo in L1_2 , D0_{22} , and D0_{24} structures and all of the D0_{24} structures except for the most stable Ni_3Ti have been calculated for the first time by this work. The elastic properties investigations of D0_{22} - Ni_3Al and Ni_3Ti , D0_{24} - Ni_3Al structures as well as solute solubility in L1_2 - Ni_3Ti and Ni_3Nb have not yet been investigated previously. The main results can be summarized as follows:

- The theoretical lattice constants and the formation enthalpies of γ , γ' , γ'' and η phases are in reasonable agreement with available literature data. According to the lowest formation enthalpies, Ni_3Ti is the most stable compound for all of the precipitates. Furthermore, the thermodynamically stable compounds are Ni_3Al , Ni_3Fe , Ni_3Cr , and Ni_3Nb .
- The elastic constants and the elastic modulus have been calculated. The mechanical stability which determined by the Cauchy-Born criteria has shown that the Ni_3Al , Ni_3Ti and Ni_3Nb compounds are mechanically stable. The Young's and shear moduli of Ni_3X intermetallic compounds are generally lower than those of Ni. The Ni_3Al compound has been identified as the most elastically anisotropic of all considered structures whereas Ni_3Ti and Ni_3Nb compounds exhibit an anisotropy of the elastic properties which is lower or similar to pure Ni.

Additionally, sublattice occupancy as well as the corresponding solubility of Al, Ti, Nb, Cr, Mo, and Fe impurities in L1_2 -structure Ni_3Al , Ni_3Ti , and Ni_3Nb intermetallic compounds have been investigated. The following results have been obtained:

- Ni_3Al : Ti, Nb, Mo, and Cr occupy the Al-sublattice while Fe occupies the Ni-sublattice. Ti and Nb atoms have negative solution energies (soluble) on Al sublattice.
- Ni_3Ti : Al occupies the Ti-sublattice while Nb, Mo, Fe, and Cr occupy the Ni-sublattice. Al atoms have negative solution energies (soluble) on the Ti sublattice, Fe atoms have negative solution energies (soluble) on the Ni sublattice.
- Ni_3Nb : Al, Ti, and Fe occupy the Nb-sublattice while Mo and Cr occupy the Ni-sublattice. Al, Ti and Fe atoms have negative solution energies (soluble) on the Nb sublattice, Fe and Mo atoms have negative solution energies (soluble) on the Ni sublattice.

References

- [1] G. P. Sabol, R. Stickler, *Phys. Status Solidi B* 35 (1969) 11–52.
- [2] A. K. Jena, M. C. Chaturvedi, *J. Mater. Sci.* 19 (1984) 3121–3139.
- [3] M. Stockinger, *Mikrostrukturelle Simulation des Gesenkschmiedens von Nickelbasis-Legierungen*, Ph.D. thesis, Technical University of Graz, 2003.
- [4] B. Oberwinkler, A. Fischersworing-Bunk, M. Hüller, M. Stockinger, in: *Superalloys 2016*, John Wiley & Sons, Ltd, 2016, pp. 513–521.
- [5] A. Drexler, B. Oberwinkler, S. Primig, C. Turk, E. Povoden-Karadeniz, A. Heinemann, W. Ecker, M. Stockinger, *Mater. Sci. Eng. A* 723 (2018) 314 – 323.
- [6] C. T. Sims, N. S. Stoloff, W. C. Hagel, *superalloys II*, Wiley New York, 1987.
- [7] R. C. Reed, *The superalloys: fundamentals and applications*, Cambridge university press, 2006.
- [8] S. Mannan, F. Veltry, in *Proceedings of the International Symposium: Superalloys 718, 625, 706 and Various Derivatives*. (The Minerals, Metals and Materials Society (TMS)) (2001) 345–356.
- [9] L. E. Shoemaker, in: E. Loria (Ed.), *Superalloys 718, 625, 706 and Derivatives 2005*, The Minerals, Metals & Materials Society Warrendale, PA, 2005.
- [10] M. Kassner, P. Kumar, W. Blum, *Inter. J. Plast.* 23 (2007) 980 – 1000.
- [11] P. Morra, S. Radelaar, M. Yandouzi, J. Chen, A. Böttger, *Inter. J. Plast.* 25 (2009) 2331 – 2348.
- [12] M. Basirat, T. Shrestha, G. Potirniche, I. Charit, K. Rink, *Inter. J. Plast.* 37 (2012) 95 – 107.
- [13] J.-B. Le Graverend, J. Cormier, F. Gallerneau, P. Villechaise, S. Kruch, J. Mendez, *Inter. J. Plast.* 59 (2014) 55 – 83.
- [14] M. Fisk, J. Ion, L.-E. Lindgren, *Comput. Mater. Sci.* 82 (2014) 531 – 539.
- [15] S. He, P. Peng, L. Peng, Y. Chen, H. Wei, Z. Hu, *J. Alloys Compd.* 597 (2014) 243 – 248.
- [16] M. Detrois, K. A. Rozman, P. D. Jablonski, J. A. Hawk, in: E. Ott (Ed.), *Proceedings of the 9th International Symposium on Superalloy 718 & Derivatives: Energy, Aerospace, and Industrial Applications*, Springer, 2018, pp. 421–437.
- [17] A. Drexler, A. Fischersworing-Bunk, B. Oberwinkler, W. Ecker, H.-P. Gänser, *Inter. J. Plast.* 105 (2018) 62 – 73.
- [18] M. Burke, M. Miller, in: E. Loria (Ed.), *Superalloys 718, 625, 706 and Derivatives 1991*, The Minerals, Metals & Materials Society Warrendale, PA, 1991, pp. 337–350.
- [19] S. Kobayashi, K. Sato, E. Hayashi, T. Osaka, T. J. Konno, Y. Kaneno, T. Takasugi, *Intermetallics* 23 (2012) 68 – 75.

- [20] Y. Chen, S. He, Z. Yi, P. Peng, *Comput. Mater. Sci.* 152 (2018) 408 – 416.
- [21] Y. Chen, S. He, Z. Yi, P. Peng, *J. Phys. Chem. Solids* 131 (2019) 34 – 43.
- [22] K. Ohira, Y. Kaneno, T. Takasugi, *Mater. Sci. Eng. A* 399 (2005) 332 – 343, measurement and Interpretation of Internal/Residual Stresses.
- [23] M. H. F. Sluiter, Y. Kawazoe, *Phys. Rev. B* 51 (1995) 4062–4073.
- [24] A. Ruban, H. Skriver, *Solid State Commun.* 99 (1996) 813 – 817.
- [25] A. V. Ruban, H. L. Skriver, *Phys. Rev. B* 55 (1997) 856–874.
- [26] C. Jiang, B. Gleeson, *Scr. Mater.* 55 (2006) 433 – 436.
- [27] Q. Wu, S. Li, *Comput. Mater. Sci.* 53 (2012) 436 – 443.
- [28] X. L. Liu, G. Lindwall, T. Gheno, Z.-K. Liu, *Calphad* 52 (2016) 125–142.
- [29] S. Rao, D. Dimiduk, T. Parthasarathy, M. Uchic, C. Woodward, *Scr. Mater.* 66 (2012) 410–413.
- [30] S. Liu, M. Wen, Z. Li, W. Liu, P. Yan, C. Wang, *Mater. Des.* 130 (2017) 157 – 165.
- [31] D. Shindo, M. Kikuchi, M. Hirabayashi, S. Hanada, O. Izumi, *Trans. Japan Ins. Metals* 29 (1988) 956–961.
- [32] A. V. Ruban, V. Popov, V. Portnoi, V. Bogdanov, *Philos. Mag.* 94 (2014) 20–34.
- [33] J.-h. Xu, B. I. Min, A. J. Freeman, T. Oguchi, *Phys. Rev. B* 41 (1990) 5010–5016.
- [34] D. Connétable, M. Mathon, J. Lacaze, *Calphad* 35 (2011) 588–593.
- [35] S. Dai, W. Liu, *Comput. Mater. Sci.* 49 (2010) 414 – 418.
- [36] Y. Lin, S.-C. Luo, M.-S. Chen, D.-G. He, C.-Y. Zhao, *J. Alloys Compd.* 688 (2016) 285–293.
- [37] Y. Lin, X.-Y. Jiang, S.-C. Luo, D.-G. He, *Mater. Des.* 139 (2018) 16 – 24.
- [38] W. T. Geng, D. H. Ping, Y. F. Gu, C. Y. Cui, H. Harada, *Phys. Rev. B* 76 (2007) 224102.
- [39] A. Jain, S. P. Ong, G. Hautier, W. Chen, W. D. Richards, S. Dacek, S. Cholia, D. Gunter, D. Skinner, G. Ceder, et al., *APL Mater.* 1 (2013) 011002.
- [40] D. Farkas, D. Roqueta, A. Vilette, K. Ternes, *Model. Simul. Mater. Sci. Eng.* 4 (1996) 359.
- [41] A. Pasturel, C. Colinet, D. N. Manh, A. T. Paxton, M. van Schilfgaarde, *Phys. Rev. B* 52 (1995) 15176–15190.
- [42] P. Lang, T. Wojcik, E. Povoden-Karadeniz, C. Cirstea, E. Kozeschnik, *Comput. Mater. Sci.* 93 (2014) 46 – 49.
- [43] J. Gachon, M. Notin, J. Hertz, *Thermochim. Acta* 48 (1981) 155 – 164.
- [44] D. Lv, D. McAllister, M. Mills, Y. Wang, *Acta Mater.* 118 (2016) 350 – 361.
- [45] G. Simmons, H. Wang, *Single crystal elastic constants and calculated aggregate properties: A handbook*, Cambridge, Mass., M.I.T. Press, 1971.
- [46] D. Kim, S.-L. Shang, Z.-K. Liu, *Comput. Mater. Sci.* 47 (2009) 254 – 260.

- [47] D. Kim, S. Shang, Z. Liu, *Intermetallics* 18 (2010) 1163–1171.
- [48] X. Luan, H. Qin, F. Liu, Z. Dai, Y. Yi, Q. Li, *Crystals* 8 (2018).
- [49] Y. Cao, J. Zhu, Y. Liu, Z. Lai, Z. Nong, *Physica B: Condens. Matter* 412 (2013) 45–49.
- [50] A. Breidi, J. Allen, A. Mottura, *Phys. Status solidi B* 254 (2017).
- [51] H. Yasuda, T. Takasugi, M. Koiwa, *Acta Metall. Mater.* 40 (1992) 381 – 387.
- [52] Z.-K. Liu, *J. Phase Equilibria Diffus.* 30 (2009) 517.
- [53] W. Pearson, *A Handbook of Lattice Spacings and Structures of Metals and Alloys*, volume 4 of *International Series of Monographs on Metal Physics and Physical Metallurgy*, Pergamon Press, 1958.
- [54] P. E. Blöchl, *Phys. Rev. B* 50 (1994) 17953–17979.
- [55] G. Kresse, J. Furthmüller, *Phys. Rev. B* 54 (1996) 11169–11186.
- [56] G. Kresse, D. Joubert, *Phys. Rev. B* 59 (1999) 1758–1775.
- [57] J. P. Perdew, K. Burke, M. Ernzerhof, *Phys. Rev. Lett.* 77 (1996) 3865–3868.
- [58] H. J. Monkhorst, J. D. Pack, *Phys. Rev. B* 13 (1976) 5188–5192.
- [59] F. Birch, *Phys. Rev.* 71 (1947) 809–824.
- [60] A. McNaught, A. Wilkinson, *IUPAC Compendium of Chemical Terminology: The Gold Book*, International Union of Pure and Applied Chemistry: Zürich, Switzerland, 1997.
- [61] J. F. Nye, *Physical properties of crystals: their representation by tensors and matrices*, Oxford university press, 1985.
- [62] R. Golezorkhtabar, P. Pavone, J. Spitaler, P. Puschnig, C. Draxl, *Comput. Phys. Commun.* 184 (2013) 1861 – 1873.
- [63] T. Dengg, *Computation of temperature dependent elastic constants within the framework of density-functional theory*, Ph.D. thesis, Karl-Franzens-Universität Graz, 2017.
- [64] J. Ericksen, *Math. Mech. Solids* 13 (2008) 199–220.
- [65] D. C. Wallace, *Thermodynamics of crystals*, Courier Corporation, 1998.
- [66] W. Voigt, *Ann. Phys.* 274 (1889) 573–587.
- [67] A. Reuss, *Z. angew. Math. Mech.* 9 (1929) 49–58.
- [68] R. Hill, *Proc. Phys. Soc. A* 65 (1952) 349–354.
- [69] S. I. Ranganathan, M. Ostoja-Starzewski, *Phys. Rev. Lett.* 101 (2008) 055504.
- [70] C. M. Kube, *AIP Adv.* 6 (2016) 095209.
- [71] O. I. Gorbatov, I. K. Razumov, Y. N. Gornostyrev, V. I. Razumovskiy, P. A. Korzhavyi, A. V. Ruban, *Phys. Rev. B* 88 (2013) 174113.
- [72] C. Kittel, P. McEuen, P. McEuen, *Introduction to solid state physics*, volume 8, Wiley New York, 1996.
- [73] C. Francois, A. Doyle, O. Jackson, et al., *Materials Handbook, A Concise Desktop Reference*, Springer, Berlin, 2000.

- [74] S. He, P. Peng, O. I. Gorbatov, A. V. Ruban, *Phys. Rev. B* 94 (2016) 024111.
- [75] H. M. Ledbetter, R. P. Reed, *J. Phys. Chem. Ref. Data* 2 (1973) 531–618.
- [76] Y. Wang, Z.-K. Liu, L.-Q. Chen, *Acta Mater.* 52 (2004) 2665 – 2671.
- [77] V. L. Moruzzi, J. F. Janak, A. R. Williams, *Calculated Electronic Properties of Metals*, Pergamon Press Inc., New York, 1978.
- [78] E. Fisher, D. Westlake, S. Ockers, *Physica status solidi (a)* 28 (1975) 591–602.
- [79] L. Koči, Y. Ma, A. R. Oganov, P. Souvatzis, R. Ahuja, *Phys. Rev. B* 77 (2008) 214101.
- [80] C. L. Fu, K. M. Ho, *Phys. Rev. B* 28 (1983) 5480–5486.
- [81] V. I. Razumovskiy, A. V. Ruban, P. A. Korzhavyi, *Phys. Rev. B* 84 (2011) 024106.
- [82] J. T. Lenkkeri, *J. Phys. F: Met. Phys.* 10 (1980) 611–618.
- [83] K. W. Katahara, M. Nimalendran, M. H. Manghnani, E. S. Fisher, *J. Phys. F: Met. Phys.* 9 (1979) 2167–2176.
- [84] F. H. Featherston, J. R. Neighbours, *Phys. Rev.* 130 (1963) 1324–1333.
- [85] K. W. Katahara, M. H. Manghnani, E. S. Fisher, *J. Phys. F: Met. Phys.* 9 (1979) 773–790.
- [86] J. A. Rayne, B. S. Chandrasekhar, *Phys. Rev.* 122 (1961) 1714–1716.
- [87] H. Zhang, B. Johansson, L. Vitos, *Phys. Rev. B* 84 (2011) 140411.
- [88] Y. Nie, Y. Xie, *Phys. Rev. B* 75 (2007) 174117.
- [89] M. J. Mehl, *Phys. Rev. B* 47 (1993) 2493–2500.
- [90] E. S. Fisher, C. J. Renken, *Phys. Rev.* 135 (1964) A482–A494.
- [91] O. Kubaschewski, *Trans. Faraday Soc.* 54 (1958) 814–820.
- [92] F. J. Bremer, M. Beyss, H. Wenzl, *Phys. Status Solidi A* 110 (1988) 77–82.
- [93] R. Cahn, P. Siemers, J. Geiger, P. Bardhan, *Acta Metall.* 35 (1987) 2737 – 2751.
- [94] K. Hagihara, T. Nakano, Y. Umakoshi, *Acta Mater.* 51 (2003) 2623 – 2637.
- [95] M. Chaturvedi, Y. Han, *Mater. Sci. Eng.* 89 (1987) L7 – L10.
- [96] A. Devaux, L. Nazé, R. Molins, A. Pineau, A. Organista, J. Guédou, J. Uginet, P. Héritier, *Mater. Sci. Eng.: A* 486 (2008) 117 – 122.
- [97] J. M. Oblak, D. F. Paulonis, D. S. Duvall, *Metall. Trans.* 5 (1974) 143.
- [98] A. Earnshaw, N. N. Greenwood, *Chemistry of the Elements*, volume 60, Butterworth-Heinemann Oxford, 1997.

Chapter 10

Conclusions and outlook

10.1 Conclusions

In this thesis, the systematic DFT-based investigations have been performed to explore some of the fundamental aspects of how hydrogen interacts with Ni and Ni-base alloys and to aid the development of Ni-base alloys with improved resistance against hydrogen induced damage intended for use in hydrogen-containing environments. The following main conclusions can be drawn from this work:

- I. The comprehensive DFT calculations have been used to study on the alloying effect of solutes in bulk Ni and Ni GB cohesion. The elements which can enhance the Ni bulk and GB cohesion have been identified. It is found that there is a linear correlation between the bulk cohesion and GB strengthening by solute alloying. Furthermore, a list of elements that contribute to HE reduction have also been selected for the design of hydrogen resistant Ni-base alloys .
- II. By investigating the HEDE mechanism of HE for the case of the special $\Sigma 5(012)$ grain boundary (GB) in Ni containing C and Mo impurity atoms within the framework of the Rice-Thomson-Wang theory. The results show that H, C, and Mo segregate to the GB in Ni, H demonstrates the GB embrittling effect while C and Mo solutes strengthen the GB in Ni. The results on co-segregation of H-C and H-Mo solute atoms show a significant distribution of the GB segregation energy and strengthening energy at the GB within the first three GB layers, while H-Mo and H-C interactions in the bulk and at the GB are very similar and can be neglected in most of cases of co-segregation.
- III. The co-segregation of S and H and their effect on fracture mode have been studied by In-situ electrochemical micro cantilever bending and DFT simulations . The DFT results show that both S and H embrittle the Ni GB, while S has more stronger effect

on Ni GB embrittling. The segregation amount of S to the GB has been identified by experimental measurement and DFT-based kinetic simulation, results show a good agreement. Combining experiment and simulation, it is found that there is a concentration-dependent effect on fracture mode of Ni GB.

- IV. By using a combination of density functional theory calculations and embedded atom method simulations for investigating the configurations of H clusters at defects in Ni at 0 K as well as finite temperatures. Results show that the H cluster stability at structural defects (vacancies and GB) of Ni is limited to temperatures below 300 K and that their appearance at the ambient temperature and therefore an impact on possible HE mechanisms is unlikely.
- V. By studying the thermodynamic and mechanical stability of Ni_3X intermetallic compounds, it is found that the most stable structures of Ni_3Al , Ni_3Ti , Ni_3Nb , Ni_3Cr , Ni_3Mo , and Ni_3Fe at 0 K are $L1_2$, $D0_{24}$, $D0_{22}$, $D0_{24}$, $D0_{22}$, and $L1_2$ structures respectively. Moreover, the site preference behavior of Al, Ti, Nb, Mo, Fe, and Cr solutes in the $L1_2$ -structure Ni_3Al , Ni_3Ti , and Ni_3Nb intermetallic compounds and the solubility of the aforementioned alloying elements have been investigated.

10.2 Outlook

As it has been discussed in Section 2.2, there are various strengthening mechanisms that can be effectively utilised to make Ni-base alloys meet the service requirement, meaning these strengthening mechanisms are also susceptible when the alloys served in the environment with the presence of hydrogen. Therefore, the future work can focus on following aspects:

- I. H-solute interaction in bulk Ni. It is known that solutes play an important role on the Ni matrix cohesion, in order to know how hydrogen interacts with solute as well as solute alloying effect on the hydrogen solubility in bulk Ni, therefore, it is needed to have a further investigation on H-solute interaction in Ni. Furthermore, as it has been concluded in Chapters 6 and 7, the H-solute interactions in the Ni bulk and GB are similar, so this investigation is also significant to understand the interactions of multiple solutes at GB.
- II. H trapping by precipitates on Ni as well as Ni/precipitate interfaces. In Chapter 9, the most stable structure of each Ni_3X type intermetallic compound has been identified and they can be used to study the H trapping by the precipitates and corresponding Ni/precipitate interfaces. From this point, a comprehensive study of H trapping by Ni_3X precipitates in different structures and chemical compositions as well as Ni/ Ni_3X interfaces is needed.

- III. Hydrogen accumulation at cracks. In Chapter 8, it has been known that hydrogen accumulates at the vacancies, GBs, and FSs of Ni in equilibrium condition. However, the hydrogen trapping under stress is not studied well. In the future, hydrogen segregation in strained Ni will be investigated to understand the distribution of hydrogen at cracks.
- IV. Solute segregation in the alloyed Ni GB. This thesis has conducted a set of investigations which considers solute segregation in the pure Ni GB, meaning concentration change effects have not been discussed here. In the future work, the alloyed Ni GB will be adopted to study the solute segregation to the GB of Ni-based alloys.

This thesis offers an in-depth theoretical study of hydrogen embrittlement in Ni-based alloys. The results can directly be used for HE-resistance performance improvement and new Ni-based alloys design. In particular, the beneficial elements found in this work can be the guidance for the strengthening design of poly-crystalline Ni-based alloys.

Appendix A

List of Papers

1. List of papers included in this thesis (with contribution statement and link to each chapter in this thesis)

- [1] S. He, W. Ecker, R. Pippan, and V. I. Razumovskiy. The effects of solute solid solution and grain boundary segregation on the strengthening in Ni. (In manuscript, to be submitted Scripta Materialia) [Chapter 5].

I performed all of calculations and composition of the paper.

- [2] S. He, W. Ecker, R. Pippan, and V. I. Razumovskiy. Hydrogen-enhanced decohesion mechanism of the special $\Sigma 5(012)[100]$ grain boundary in Ni with Mo and C solutes. Computational Materials Science 167 (2019)100-110. [Chapter 6]

I performed all of calculations and composition of the paper.

- [3] T. Hajilou, I. Taji, F. Christien, S. He, D. Scheiber, W. Ecker, R. Pippan, V. I. Razumovskiy, A. Barnoush. Hydrogen enhanced intergranular failure of sulfur doped nickel grain boundary: In-situ electrochemical micro cantilever bending test vs. DFT (In manuscript, to be submitted to a peer-reviewed journal) [Chapter 7].

I performed all of DFT calculations and composition for the DFT sections of the paper, D. Scheiber did kinetic calculations and composition for corresponding sections. T. Hajilou, I. Taji, F. Christien, and A. Barnoush carried out the experiment parts .

- [4] S. He, M. N. Popov, W. Ecker, R. Pippan, V. I. Razumovskiy. A theoretical insight into hydrogen clustering at defects in Ni. (Done, to be submitted to a peer-reviewed journal) [Chapter 8]

I did DFT and EAM calculations for 0 K and Maxim N. Popov did the EAM calculations of MSD at finite temperatures.

- [5] N. Kulo, S. He, W. Ecker, R. Pippan, T. Antretter, V. I. Razumovskiy. Thermodynamic and mechanical stability of Ni_3X -type intermetallic compounds, *Intermetallics*, 114(2019)106604 [Chapter 9].

N. Kulo helped me to do the DFT calculations and data analysis, I conceived the idea of this study and wrote the paper from the input of N. Kulo, T. Antretter participated with helpful discussions on the paper.

For all the papers above, my supervisor R. Pippan, project managers W. Ecker and V. I. Razumovskiy contributed to supervise the project, discuss the results as well as polish the papers.

2. Publications not included in this thesis

- [6] Y. Chen, S. He, Y. Zhou, P. Peng. A synergistic reinforcement of Re and W for ideal shear strengths of γ' - Ni_3Al phases. *Journal of Physics and Chemistry of Solids*, 131(2019)34-43.
- [7] Y. Chen, S. He, Y. Zhou, P. Peng. Impact of correlative defects induced by double Re-addition on the ideal shear strength of γ' - Ni_3Al phases. *Computational Materials Science*, 152(2018)408-416.
- [8] W. Zheng, S. He, J. Wang, and H. Mao. Thermodynamic Evaluation of the Co-Al-C System by Coupling Ab Initio Calculations and CALPHAD Approach. *Journal of Phase Equilibria and Diffusion*, 39(2018)538-548.
- [9] W. Zheng, S. He, M. Selleby, Y. He, L. Li, X. G. Lu, J. Ågren. Thermodynamic assessment of the Al-C-Fe system. *Calphad* 58 (2017)34-49.
- [10] S. He, P. Peng, O.I. Gorbатов, A. Ruban. Effective interactions and atomic ordering in Ni-rich Ni-Re alloys. *Physical Review B*, 94(2016)024111.
- [11] S. He, P. Peng, L. Peng, Y. Chen, H. Wei, Z. Q. Hu. An interplay of sulfur and phosphorus at the γ -Ni/ γ' - Ni_3Al interface. *Journal of Alloys Compounds*, 597(2014)243-248.
- [12] L. Peng, P. Peng, Y. G. Liu, S. He, H. Wei, T. Jin, Z. Q. Hu. The correlation between Re and P and their synergetic effect on the rupture strength of the γ/γ' interface, *Computational Materials Science* 63(2012)292-302.

Appendix B

Contributions to Conferences

- [1] S. He, W. Ecker, R. Pippan, V. I. Razumovskiy. Hydrogen-enhanced decohesion in Ni from DFT calculations. 3rd Austrian-German Workshop on Computational Materials Science, 15-19.01.2018, Kirchdorf, Tirol. (Oral presentation)
- [2] S. He, W. Ecker, R. Pippan, V. I. Razumovskiy. Hydrogen-enhanced decohesion in Ni from DFT calculations. Steely Hydrogen 2018: 3rd International Conference on Metals & Hydrogen, 29-31.05.2018, Gent, Belgium. (Poster)
- [3] S. He, W. Ecker, R. Pippan, V. I. Razumovskiy. Hydrogen-enhanced decohesion in Ni from DFT calculations. THERMEC'2018, 08-13.07.2018, Gent, Belgium. (Poster)
- [4] S. He, W. Ecker, R. Pippan, V. I. Razumovskiy. First-principles study of H co-segregation with C and Mo to the $\Sigma 5$ (012)[100] symmetrical tilt GB in Ni. EUROMAT2019, 01-05.09.2019, Stockholm, Sweden. (Oral presentation)

Appendix C

Acronyms and Abbreviations

| | |
|---------|--|
| AIDE | Adsorption-induced dislocation emission |
| bcc | Body-centered cubic |
| CSL | Coincidence site lattice |
| DFT | Density functional theory |
| XC | Exchange correlation |
| EAM | Embedded atom method |
| EBSD | Electron back-scatter diffraction |
| FS | Free surface |
| FIB-SEM | Focused ion beam - scanning electron microscopy |
| FLAPW | Full potential linearized augmented plane wave |
| fcc | Face-centered cubic |
| GB | Grain boundary |
| GGA | Generalized gradient approximation |
| hcp | Hexagonal close packed |
| HE | Hydrogen embrittlement |
| HEDE | Hydrogen-enhanced decohesion |
| HELP | Hydrogen enhanced localized plasticity |
| HESIV | Hydrogen-enhanced strain-induced vacancy formation mechanism |
| Int. | Interstitial |
| IG | Intergranular |
| LAMMPS | Large-scale atomic/molecular massively parallel simulator |
| LD | Load-displacement |
| LDA | Local density approximation |
| MD | Molecular dynamics |

| | |
|--------|--|
| ML | Monolayer |
| MSD | Mean-square displacement |
| NBA | Ni-based alloy |
| NPT | Isothermal–isobaric ensemble |
| OS | Octahedral site |
| PAW | Projector-augmented-wave |
| PBE | Perdew-Burke-Ernzerhof |
| PBEsol | Perdew-Burke-Ernzerhof revised for solids |
| PW91 | Perdew-Wang91 |
| RT | Room temperature |
| SC | Supercell |
| Sub. | Substitutional |
| TS | Tetrahedral site |
| VASP | Vienna <i>ab initio</i> simulation package |
| Vac. | Vacancy |